IOCCG Report

# Remote Sensing of Inherent Optical Properties: Fundamentals, Tests of Algorithms, and Applications

## Table of Contents

## Preface

Historically, remote sensing of ocean color was focused on the retrieval of chlorophyll concentration in the global oceans. Recent studies, as synoptically outlined in the Report 3 of the International Ocean-Colour Coordinating Group (IOCCG), have emphasized the importance of understanding and retrieving inherent optical property (IOP) in ocean color remote sensing. As a follow up, this report promotes the research and applications of IOPs.

IOPs are at the center of satellite measured water-leaving radiance and water constituents. At the same time, variations of IOPs are clear indications of changes of water mass or water constituents. Following these basic concepts, significant progress has been achieved in the past decade regarding remote sensing algorithms for IOPs and applications of IOPs in oceanographic studies. In an endeavour to emphasize IOPs in ocean optics and in ocean color remote sensing, this report summarizes the progress to date. It lays out the fundamental relationships between water-leaving radiance and IOPs (Chapter 1), establishes a data base for algorithm testing and evaluation (Chapter 2), and provides a discussion of sources of uncertainty (Chapter 3).

This report also presents a series of commonly encountered algorithms in remote sensing practices and their performances when applied to compiled synthetic and *in situ* data sets (Chapter 4 – Chapter 12). These are presented in such a fashion that sufficient details are included for easy inter-comparison among the algorithms and easy utilization by interested researchers. The ocean-color community has accomplished a lot by developing algorithms for ocean color remote sensing. What is lacking, however, are broad-range tests, validations, and inter-comparisons. This report provides initial results in this regard. It should be pointed out that algorithm development is a continuous process, and this report by no means attempts to include all the algorithms developed, or under development, in the community.

The report ends with examples of IOP applications in oceanographic studies (Chapter 13) and a summary and conclusions (Chapter 14). This report may never have become a reality without the support from the IOCCG Committee, and the diligent work of the "Algorithm Working Group". In particular, Z.P.L. wishes to extend his great appreciations to the series editor, Dr. Venetia Stuart, for her enormous assistance during the whole process.

## Chapter 1. Why are Inherent Optical Properties Needed in Ocean Color Remote Sensing?

J. Ronald V. Zaneveld, Andrew Barnard, and ZhongPing Lee

### 1.1 Introduction

In this volume we are interested in the determination of useful oceanographic parameters from the radiance measured by a satellite based sensor. The measured radiance originates from sunlight that passes through the atmosphere, is reflected, absorbed, and scattered by constituents in the ocean, and is transmitted back through the atmosphere to the satellite based sensor. Solar photons that reach the sea surface are redistributed from those that reached the top of the atmosphere. Absorption of the aerosols and gases changes the intensity, and scattering changes the intensity as well as the directionality, resulting in diffuse light that is a function of wavelength. The directional slope spectrum of the waves at the sea surface together with the radiance distribution determine the reflected radiance. In addition to the waves, white caps, bubbles, and surface slicks also affect the redistribution of light entering the ocean.

The processes of scattering and absorption by dissolved and suspended materials in the ocean affect the spectrum and radiance distribution (light field) of the light emerging from the ocean – the so called water-leaving radiance. The scattering and absorption characteristics of ocean water and its constituents are described by the inherent optical property (IOP, Preisendorfer [1976]). Note that the IOP does not depend on the radiance distribution. If we can successfully remove the atmosphere and surface effects, the best we can hope for from inversions of the water-leaving radiance are the scattering and absorption characteristics of the dissolved and suspended materials.

While the spectral quality and quantity of the water-leaving radiance is largely determined by the IOP, conventionally the modification of the radiance has been used to directly determine oceanic constituents. Typically the desired parameter has been the chlorophyll concentration, Chl. Usually algorithm development searches for a combination of radiance signals at several wavelengths to find some ratio or other combination that relates empirically to the desired parameter. The coefficients contained in these algorithms are generally derived by pooling data collected at various spatial and temporal scales. This globally and seasonally inclusive approach, which removes "noise" associated with the data sets, diminishes important spatial and temporal features of the global oceans. This approach assumes that the ocean is a black box, and that little is to be gained by examining how the black box works, presumably because the black box is too difficult to be understood. With such a perception, most algorithm development (even today) uses the black box approach (see Fig. 1.1). However, a great deal is known about the IOP and its influence on the water-leaving radiance, as is detailed below.

In the past (CZCS), present (e.g., SeaWiFS, MODIS), and in the future (VIIRS-NPOESS) the emphasis of ocean color remote sensing has been on the derivation of the chlorophyll concentration [*Hooker et al.*, 1992; *Yoder et al.*, 2001]. This is partly because values of chlorophyll play a central role in conventional algorithms for primary production or light attenuation coefficients. But, fundamentally, water color is determined by IOP, and Chl is just one of the active components that determine the IOP, therefore Chl can be determined only with a relatively large uncertainty from ocean color remote sensing.

Since no amount of study will modify nature, and the link between IOP and Chl has remained weak, no substantial progress has been made in the accuracy of the determination of Chl from space in the last two decades. On the other hand, it is now assumed as in VIIRS that ocean color can be operational. This should not be interpreted to mean that no further progress can be made in deriving useful information from remotely sensed radiance. By starting at the product end (the need to determine Chl, production, etc) the real inversion signal, IOP, is ignored. Fundamentally, a better approach would be to ask: "What can water-leaving radiance really give us, and with what accuracy?" Such an approach, based on physics, would examine how water color is related to the IOP and then, secondarily how the IOP are related to the biogeochemical parameters of the suspended and dissolved constituents, and finally what these parameters can tell us about processes. Such an approach, as shown below in more detail, would enhance

our understanding about the remotely sensed signal, optimize its utilization, and eventually provide improved and reliable products related to the biogeochemistry of the oceans.


Figure 1.1. Diagram of inverse radiative transfer elements using the "black box" approach.

### 1.2 The Forward Problem of Ocean Optics

The process of forward radiative transfer can be summarized by Fig. 1.2. In ocean color remote sensing, the forward radiative transfer problem is to predict the spectral distribution of water-leaving radiance based on a quantitative description of all the absorption and scattering characteristics of the optical components in the ocean. A recent review of radiative transfer can be found in Zaneveld et al. [2005b]. The inverse problem is the determination of useful oceanic particulate and dissolved parameters when the spectral characteristics of the water-leaving radiance are known.

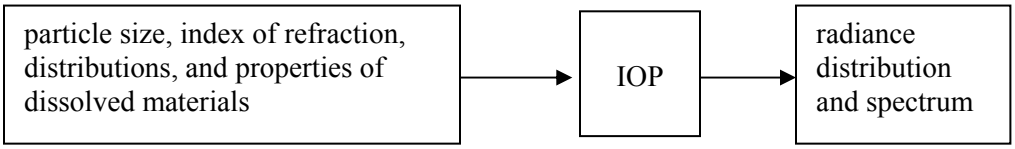


Figure 1.2. Diagram of forward radiative transfer elements.

The forward problem is governed by the Equation of Radiative Transfer (ERT). Without internal sources such as fluorescence or Raman scattering, the ERT is given by:

$$\nabla . L(\vec{\mathbf{x}},\lambda,\theta,\phi) = -c(\vec{\mathbf{x}},\lambda)\, L(\vec{\mathbf{x}},\lambda,\theta,\phi) + \int_0^{4\pi} \beta(\vec{\mathbf{x}},\lambda,\theta,\phi,\theta',\phi')\, L(\vec{\mathbf{x}},\lambda,\theta',\phi')\mathrm{d}\omega'. \quad (1.1)$$

The radiance is $L$, units are $\mathrm{W(m^2sr)^{-1}}$, $\vec{\mathbf{x}}$ is the position vector $(x,y,z)$, $\theta$ is the zenith angle, $\phi$ is the azimuth angle, $c$ is the beam attenuation coefficient (in units of $\mathrm{m^{-1}}$). $\beta(\vec{\mathbf{x}},\theta,\phi,\theta',\phi')$ is the volume scattering function (VSF), with units of $\mathrm{m^{-1}sr^{-1}}$. Many books have been written regarding solutions to the ERT (e.g., Chandrasekhar [1960] and Preisendorfer [1976]).

The most common approach in oceanography is to assume that horizontal gradients in radiance and IOP are much smaller than vertical ones, so that horizontal structure is ignored. This leads to:

$$\cos(\theta)\, \mathrm{d}L(z,\lambda,\theta,\phi)/\mathrm{d}z = -c(z)\, L(z,\lambda,\theta,\phi) + \int_0^{4\pi} \beta(z,\lambda,\theta,\phi,\theta',\phi')\, L(z,\lambda,\theta',\phi')\mathrm{d}\omega'. \quad (1.2)$$

This is the ERT for the so-called plane parallel assumption without internal sources and is widely applied. Numerical solutions to this equation can be found in Mobley [1995] (Hydrolight) and Thomas and Stamnes [1999].

There is a large literature on radiative transfer in the ocean and atmosphere. This body of work is based on deriving radiance distributions when the IOPs are known. Typically, for oceanographic applications, the IOPs used are based on knowledge or speculation of the relationship between particulate

and dissolved materials and the IOPs. Again there is a large and developing literature relating particulate properties such as particle concentration, size distributions, index of refraction distributions, and shape to IOP (for a recent review see Twardowski et al. [2005]). The forward problem is thus logically broken into two parts: The relationship between biogeochemical parameters and IOP, and the relationship between the IOP and the radiance distribution.

### 1.3 Inherent Optical Properties

Much has been written on the IOPs, and their wavelength dependencies; examples of which can be found throughout the books by Shifrin [1988], Kirk [1994], and Mobley [1994]. We will briefly summarize here.

The beam attenuation coefficient ($c$) is a sum of the coefficients of absorption ($a$) and scattering ($b$),

$$c = a + b. \tag{1.3}$$

The total scattering coefficient can be divided into forward, $b_f$, and backward, $b_b$, components:

$$b = b_b + b_f, \tag{1.4}$$

and

$$b_f = 2\pi \int_0^{\pi/2} \beta(\theta)\sin(\theta)\,\mathrm{d}\theta \text{ and } b_b = 2\pi \int_{\pi/2}^{\pi} \beta(\theta)\sin(\theta)\,\mathrm{d}\theta\,. \tag{1.5}$$

The theoretical aspects of light scattering are treated extensively in van de Hulst [1981]. For the various semi-analytical and analytical remote sensing algorithms, we now have defined the two key IOPs relevant to the remote sensing reflectance, $a$ and $b_b$. These IOPs are often separated into operationally defined components such as the dissolved and particulate fractions and water:

$$a = a_w + a_{ph} + a_d + a_g, \tag{1.6}$$

and,

$$b_\mathrm{b} = b_\mathrm{bw} + b_\mathrm{bp}, \tag{1.7}$$

$$b_f = b_{fw} + b_{fp}, \tag{1.8}$$

which applies to Eq. 1.3 as:

$$c = a + b_f + b_b. \tag{1.9}$$

The subscripts g, p, and w represent dissolved (historically called gelbstoff or gilvin), particulate matter, and water, respectively. Subscripts ph and d represent the algal and non-algal components of the particles, respectively. Operationally, the dissolved fraction typically comprises all substances that pass through a 0.2 μm filter. The non-algal component is comprised of non-living particulate organic material, living particles such as bacteria, inorganic minerals, and bubbles. The relative contributions of these different particle groups to particulate backscattering are poorly known, but recent progress has been made [*Stramski et al.*, 2001].

Substituting all of the above into the ERT (Eq. 1.2) gives:

$$\cos(\theta)\,\mathrm{d}L(z,\lambda,\theta,\phi)/\mathrm{d}z = -[a_\mathrm{w} + a_\mathrm{g} + a_\mathrm{ph} + a_\mathrm{d} + b_\mathrm{w} + b_\mathrm{p}](z,\lambda)\,L(z,\lambda,\theta,\phi) + \int_0^{4\pi} [\beta_\mathrm{w}(z,\lambda,\theta,\phi,\theta',\phi') + \beta_\mathrm{p}(z,\lambda,\theta,\phi,\theta',\phi')]\,L(z,\lambda,\theta',\phi')\mathrm{d}\omega'. \tag{1.10}$$

Of the IOP parameters in the ERT, only $a_\mathrm{ph}$ relates more or less directly to Chl (depending on the presence of ancillary pigments and their proportionality to chlorophyll). The other parameters only relate very indirectly and weakly to Chl. In so-called Case 1 waters [*Morel*, 1988], it is assumed that all non-water components closely vary with Chl. This has been shown to be questionable, especially in coastal waters. It is thus clear, that in nature, deriving the radiance based on knowledge of Chl only, will often lead to incorrect results.

When solving a forward radiative transfer problem, one determines the IOP in some manner. This can be done by measurement or modeling. Modeling often involves electromagnetic theory, as this allows one

to derive IOP based on the particle size distribution, index of refraction distribution and shape distribution. Clearly, requiring all of the particulate properties above to be closely related to Chl, is unreasonable, though in practice has quite frequently been done (e.g., Morel [1988] and Haltrin [1999]). This encourages people to believe that all IOPs are in fact a function of Chl only, when this is far from the truth.

### 1.4 The Inverse Problem of Ocean Optics

The inversion problem is to determine the biogeochemical parameters from the upwelling radiance spectrum, i.e. the normalized water-leaving radiance. Zaneveld [1973] has shown that the radiance distribution and its derivative can, in theory, be inverted to obtain the VSF and beam attenuation coefficient, i.e. the IOP. This has not been done in practice. An important point is, however, that the entire radiance distribution and its depth derivative must be known to obtain the IOP. In remote sensing we only know the radiance at the surface in a few directions. We therefore cannot expect to be able to accurately invert for all of the IOPs. A corollary is that we are unable to accurately invert for the complete suite of biogeochemical parameters which determine the IOPs.

Inversion for either IOP or biogeochemical parameters is thus inexact and must, perforce, depend on approximations. Based on the discussion above, it is clear that inversion is also a two-step process, explicitly or implicitly: the derivation of IOP from the radiance, and then biogeochemical parameters from the IOP. Both of these are inexact procedures, especially for the separation of particulate and dissolved materials. Due to the extremely complex nature of these materials, their full details cannot be expected to be inverted from the IOP. Nonetheless, one would logically expect inversion of the water leaving radiance spectrum to follow an inverse approach to that of Fig. 1.2.

Historically, starting with the CZCS, remote sensing inversions have been focused on the direct derivation of the Chl from water-leaving radiance (e.g., Fig. 1.1). This was based on the early recognition that chlorophyll-laden waters are “greener” than chlorophyll poor waters. While this was a reasonable starting point, it is also unfortunate in that this is still the oceanographic parameter chosen for performance criteria of future satellite sensors such as NPOESS–VIIRS. This is unfortunate not because chlorophyll is of no interest to scientists and managers, but because chlorophyll is only indirectly or not at all related to many of the IOPs that determine radiance, as shown in the IOP section and Fig. 1.3 below. Using chlorophyll as the primary product therefore minimizes the information that can be gained from optical remote sensing. Even the chlorophyll concentration itself could be determined with greater accuracy if there was a full understanding of all the optical processes that connect the remotely sensed radiance to the IOP and the IOP to chlorophyll.

It is of course possible to find empirical relationships between e.g. radiance ratios and Chl, but the uncertainties in such relationships cannot be predicted and analyzed. Furthermore such relationships cannot be justified or derived *a priori* using radiative transfer. Because of this most of the information contained in remotely sensed radiance is ignored or overlooked. This approach thus limits the use and applicability of optical remote sensing.

How can one obtain the maximum information from remote sensing? This requires going back to the approach in Fig. 1.3. We must recognize that the radiance spectrum depends physically on the IOP and solar input. Thus if we focus on the derivation of the IOP to the maximum allowed by the geometric restrictions of radiative transfer, we have not diminished the information given to us. Once the IOP are in hand we can ask the second question: “What particulate and dissolved properties can be derived from the remotely determined IOP?” Such an IOP based inversion maximizes the information gained from remote sensing, whereas the black box approach minimizes it. Recently good progress has been made in the inversion of IOP from the upwelled radiance spectrum (for example, Roesler and Perry [1995]; Lee et al. [1996a], Garver and Siegel [1997]; Hoge and Lyon [1996]; Carder et al. [1999]; Maritorena et al. [2002]; Lee et al. [2002]; Roesler and Boss [2003]).

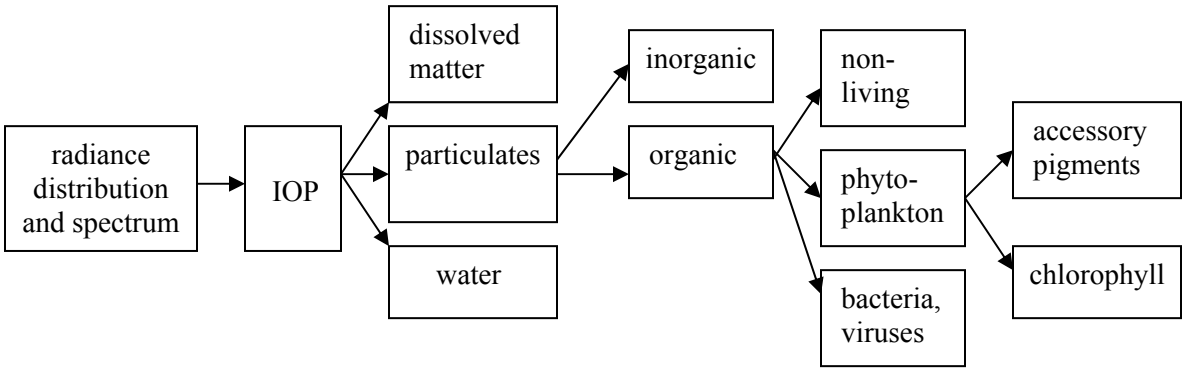


Figure 1.3. Diagram of inverse radiative transfer elements. Many further parameters are derived from theses constituents, such as DOC, POC, productivity, etc.

Semi-analytical approaches to remote sensing inversion [*Gordon et al.*, 1988; *Morel*, 1988] use an IOP approach in that they use the relationship between the oceanic constituents and the IOP upon which to base the inversion. Such semi-analytical approaches are based on simple approximations of the remote sensing reflectance such as Eq. 1.11 below. To complete this discussion we present below the fundamental relationship that links remote-sensing reflectance (or water-leaving radiance) and the IOP.

### 1.5 The Dependence of the Remote Sensing Reflectance on the IOP

Most remote sensing inversions are based on this simple relationship:

$$r_{rs} = L_u(0^-)/E_d(0^-) = g\frac{b_b}{a}, \tag{1.11}$$

where $L_u(0^-)$ and $E_d(0^-)$ are is the upwelling radiance and downwelling irradiance just below the sea surface, respectively. A similar relationship developed for subsurface irradiance reflectance was first derived by Gordon et al. [1975] and Morel and Prieur [1977] based on modeling the results from radiative transfer calculations. They found that the water reflectance is proportional to the backscattering coefficient and inversely proportional to the absorption coefficient. The proportionality factor $g$ (also called $f/Q$ in the literature, in unites of $sr^{-1}$), which generally varies in a range of 0.084 – 0.15 $sr^{-1}$ for nadir-viewed radiance [*Lee et al.*, 2004; *Morel and Gentili*, 1993], depends on how the backscattered light relates to the backscattering coefficient, and therefore to the details of the volume scattering function in the backward direction and the radiance distribution. Most of the directional effects of radiative transfer are thus contained in the factor $g$, and this factor has been studied in detail (for example Gordon et al. [1988]; Morel and Gentili [1993]; Lee et al. [2004]). Eq.1.11 is the starting point for many inversion algorithms, but it ignores the dependence of $g$ on the shape of the volume scattering function and the radiance distribution.

Based on the derivations of Zaneveld [1982; 1995], a theoretical relationship of the dependence of the remote sensing reflectance on the IOP can be obtained from the ERT (in the form of Eq. 1.11) for the nadir radiance, $L_u$, for which $\cos(\theta) = -1$, and for which we can define a vertical attenuation coefficient $k_u$):

$$r_{rs}(z) = L_u(z)/E_d(z) = \frac{1}{\overline{\mu}_d(z)}\frac{\frac{f_b(z)}{2\pi}b_b(z)}{k_u(z) + c(z) - f_L\, b_f(z)}, \tag{1.12}$$

where

$$\bar{\mu}_d(z) = \frac{E_d(z)}{E_{od}(z)}, \tag{1.13}$$

$$f_b(z) = \left( \int_0^{2\pi} \int_0^{\pi/2} \beta(z,\pi,0,\theta',\varphi') L(z,\theta',\varphi') \sin(\theta') d\theta' d\varphi' \right) \Big/ \left( \frac{b_b(z)}{2\pi} E_{od}(z) \right), \tag{1.14a}$$

$$f_L(z) = \left( \int_0^{2\pi} \int_{\pi/2}^{\pi} \beta(z,\pi,0,\theta',\varphi') L(z,\theta',\varphi') \sin(\theta') d\theta' d\varphi' \right) \Big/ \left( b_f(z) L_u(z) \right). \tag{1.14b}$$

Eq. 1.12 is an exact expression as it is only a rewrite of the ERT. All of the details of the radiative transfer process are compressed into the parameters $\bar{\mu}_d(z)$, $f_b(z)$, $f_L(z)$, and $k_u(z)$.

The simple relationship in Eq. 1.11 is thus clearly an approximation. Based on Eq. 1.12, Zaneveld [1995] has derived the following (also approximate) dependence of $g$:

$$g \approx \frac{f_b}{2\pi \bar{\mu}_d(0^-)(1 + 1/\bar{\mu}_\infty)}, \tag{1.15}$$

where $\bar{\mu}_\infty$ is the asymptotic average cosine, which in turn can be described as a function of $b/c$ [*Berwald et al.*, 1995; *Zaneveld*, 1989].

We thus find that the remote sensing reflectance can be expressed directly in terms of IOP. This is logical as that reflectance is a measure of water-leaving radiance while radiance is determined by the ERT. The difficult part is that all of the directional effects of radiative transfer are involved. The entire shape of the volume scattering function thus matters. Therefore anytime we use inversion formulas such as Eqs. 1.11 and 1.15 approximations, uncertainties are introduced.

A further problem in the interpretation of remotely derived properties is the vertical structure of the IOP. Recently Zaneveld et al. [2005a] derived the dependence of the reflectance at the surface on the vertical structure of optical parameters from first principles. It was shown that the depth dependence is a function of the derivative of the round trip attenuation of the downwelling and backscattered light. With some approximation it can be shown that the backscattering to absorption ratio follows the same vertical integration rule. For backscattering and absorption separately, and for chlorophyll it can be shown that there is no general formula that allows one to integrate the vertical structure and arrive at the remotely sensed parameter. Only in the special case of "optical homogeneity" where the ratio of the backscattering and absorption coefficients does not vary with depth, can the vertical structure be ignored.

What we learn from the above discussion is that in remote sensing inversion the directional and vertical details are initially conveniently buried in various model parameters. Later, when higher accuracies of inversion are required, this then necessitates the reinsertion of those information, such as the directional effects as evidenced by Morel et al. [1993; 1996] on the bi-directional reflectance. What has not been done is to start with an expression such as Eq. 1.12, which contains the full ERT and use this as a basis for the derivation of IOP and hence particulate and dissolved properties. This then is an approach to the question: "What information about the oceanic environment can optical remote sensing provide us?" The multiple connections in Fig. 1.3 can then be explored, and such an approach would allow the maximum information content of the remotely sensed data to be obtained.

## Chapter 2. Synthetic and *in situ* Data Sets for Algorithm Testing

Stephane Maritorena, ZhongPing Lee, KePing Du, Hubert Loisel, Roland Doerffer, Collin Roesler, Paul Lyon, Akihiko Tanaka, Marcel Babin, and Oleg V. Kopelevich

In algorithm testing and evaluation, we are frequently limited by the availability of adequate data sets. In many studies, individual groups measured some data from limited areas. Those data sets, which are important for the initial development of algorithms, usually lack the dynamic range, and therefore make it difficult to evaluate an algorithm's performance in broader scales. To fill in this gap and to have a common ground for algorithm testing, two independent data sets were compiled and adopted by the "Algorithm Working Group". One of the data sets is compiled from global field measurements, where uncertainties among measured properties are common (see Chapter 3). Another data set is simulated using the widely accepted numerical code Hydrolight [*Mobley*, 1995], with input IOPs generated based on extensive measurements made in the field. This synthetic data set can be viewed as results from ideally controlled experiments where errors from measurement processes are minimal. This chapter summarizes the characteristics of both synthetic and *in situ* data sets.

### 2.1 *In situ* Data Set

The *in situ* data set is an extraction from NASA's SeaWiFS Bio-optical Archive and Storage System (SeaBASS) (Hooker at al. [1994], http://seabass.gsfc.nasa.gov/) and contains chlorophyll-a concentration (Chl), above-surface remote sensing reflectance ($R_{rs}$, which is the ratio of water-leaving radiance, $L_w$, to downwelling irradiance just above the surface, $E_d(0^+)$) at the first five SeaWiFS bands (412, 443, 490, 510 and 555 nm), along with the detrital ($a_d$), gelbstoff ($a_g$), and phytoplankton ($a_{ph}$) absorption coefficients. Detrital ($a_d$) and gelbstoff ($a_g$) absorption coefficients were summed to form a single term [*Carder et al.*, 1991] as $a_{dg}$ ($a_{cdm}$ in Maritorena et al. [2002]) and total absorption ($a$) was calculated by adding pure water values ($a_w$) [*Pope and Fry*, 1997] to $a_{ph}$ and $a_{dg}$ at each wavelength. The chlorophyll-a, remote sensing reflectance, and absorption data were considered a match (i.e. coming from a unique station) when all measurements were made within a 12-hour window and within 0.05 degrees in both latitude and longitude. Absorption data come from hyperspectral spectrophotometric measurements but only the SeaWiFS bands were used for consistency with the remote sensing reflectance data.

Methods to measure $R_{rs}$, $a_d$, $a_g$ and $a_{ph}$ are summarized in NASA's technical memorandum [*Mueller and Austin*, 1992]. Generally, phytoplankton absorption coefficients were obtained by spectrophotometric measurements after filtration of a water sample through a GF/F filter. Detrital absorption coefficients were obtained after a methanol extraction of the pigments on the GF/F filter. Gelbstoff absorption coefficients were obtained by measuring the absorbance of the filtrate with a spectrophotometric cell (usually ~10 cm in length). Remote sensing reflectance data were obtained by either in-water or above-surface radiometric measurements [*Mueller et al.*, 2002]. Backscattering measurements were too rare to be included here. As always, errors (sometimes quite large) are associated with each of the measured components.

Data were filtered by applying quality control procedures to the remote-sensing reflectance and absorption data. For $R_{rs}$, these procedures consisted of comparisons with the SeaBAM data set [*O'Reilly et al.*, 1998] and the synthetic data set described in Section 2.2. For a given chlorophyll range, data with $R_{rs}(\lambda)$ values either 10% higher or 10% lower than the maximum or minimum value found in the SeaBAM or synthetic data sets for the same Chl range were eliminated. While this procedure removed extra noise in the data set, it may have also removed some extreme cases such as CDOM or sediment dominated waters. Of the 1235 original data points, 177 points were eliminated during this step.

For the absorption components, the following controlling factors were applied:

$$1.0 < a_{dg}(412)/a_{dg}(443) < 2.0,$$
$$1.0 < a_{dg}(443)/a_{dg}(490) < 3.0,$$
$$0.5 < a_{ph}(412)/a_{ph}(443) < 1.1,$$

$$0.1 < a_{ph}(490)/a_{ph}(443) < 1.0,$$

and another 402 points were removed during this step. The final *in situ* data set contains only 656 stations with a complete set of Chl, $R_{rs}$, and component absorption data. Most of the data come from locations that are relatively close to the coast and some of the data are from high latitudes. Fig. 2.1 presents a summary of the origin and location of the *in situ* data set.

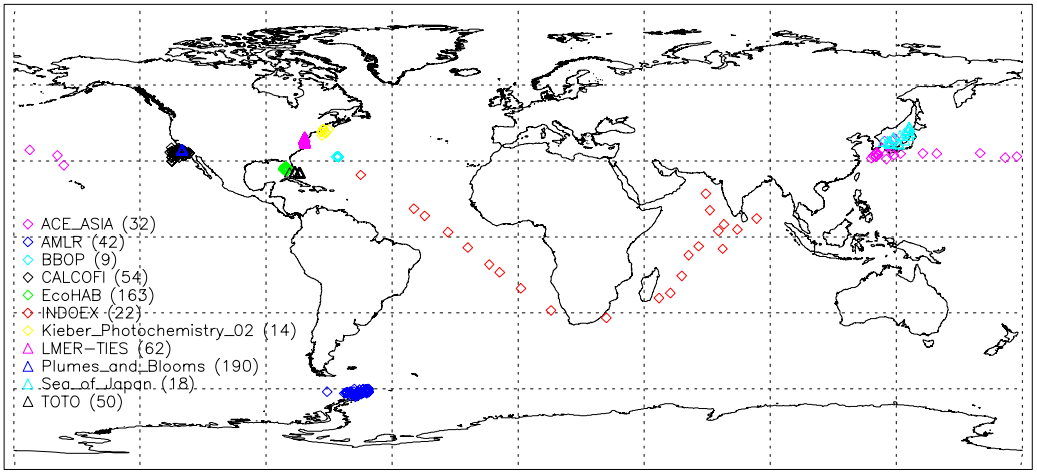


Figure 2.1. Data location of the *in situ* data set. The origin of the data and the number of stations (in parentheses) by experiment are also indicated.

### 2.2 Synthetic Data Set

This data set (a total of 500 points) contains both inherent (IOP) and apparent (AOP) optical properties. IOPs, required as inputs for Hydrolight [*Mobley*, 1995], are simulated with optical/bio-optical parameters/models. Detailed descriptions regarding the simulation of IOPs and AOPs can be found at http://www.ioccg.org/groups/OCAG_data.html.

To summarize briefly, the absorption coefficient of the bulk water was simulated using a four-term model [*Bukata et al.*, 1995; *Carder et al.*, 1991; *Doerffer et al.*, 2002; *Fischer and Fell*, 1999; *Prieur and Sathyendranath*, 1981; *Roesler et al.*, 1989], with contributions from water molecules, phytoplankton, detritus, and gelbstoff. Values of $a_w(\lambda)$ were taken from Pope and Fry [1997]. Values of $a_{ph}(\lambda)$ were modeled as $a_{ph}(440)$ multiplying the spectral shape of phytoplankton absorption coefficient ($a_{ph}^{+}(\lambda) \equiv a_{ph}(\lambda)/a_{ph}(440)$), with $a_{ph}(440)$ expressed as a function of Chl [*Bricaud et al.*, 1995]. $a_{ph}^{+}(\lambda)$ were taken from extensive measurements (600 spectra) of Bricaud et al. [1995; 1998] and Carder et al. [1999]. These spectral shapes have different characteristics between oligotrophic and eutrophic waters [*Hoepffner and Sathyendranath*, 1992; *Stuart et al.*, 1998]. To represent this natural variation, at least to the first order, this $a_{ph}^{+}(\lambda)$ data bank is divided into nine groups separated by the measured $a_{ph}(440)$ values. Fig. 2.2 presents examples of $a_{ph}^{+}(\lambda)$ from the nine groups. In the simulation of $a_{ph}(\lambda)$ spectra, $a_{ph}^{+}(\lambda)$ is selected randomly within the group where $a_{ph}(440)$ value falls in. By such a process, variability of $a_{ph}$ spectral shapes remains among the modeled $a_{ph}(\lambda)$ spectra, and at the same time $a_{ph}^{+}(\lambda)$ of eutrophic waters will not be used to generate $a_{ph}(\lambda)$ of blue oceanic waters, or vice versa.

Absorption spectra of both detritus and gelbstoff were described as exponentially decreasing functions with wavelength [*Bricaud et al.*, 1995; *Roesler et al.*, 1989]. The spectral slopes and absorption values at 440 nm were considered as random variables but constrained by ranges commonly observed in

the field. The absorption coefficients at 440 nm were also varied randomly, but this randomness was constrained such that the ranges were wider for higher Chl values and narrower for lower Chl values.

The total scattering coefficient was simulated by a three-term model [*Bukata et al.*, 1995], with contributions from water molecules, phytoplankton, and inorganic particles. Two different particle phase functions were used to represent the scattering distribution of phytoplankton and inorganic particles. For both particulates, the scattering coefficients at 550 nm and the spectral exponents were varied randomly (but within commonly observed ranges).

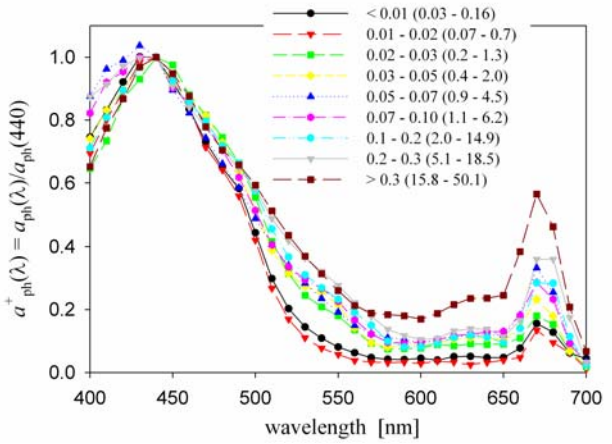

Figure 2.2. Examples of $a_{ph}$ spectral shape for the nine $a_{ph}$ groups (separated by values of $a_{ph}(440)$ [$m^{-1}$]). Numbers in parenthesis are the range of Chl [$mg/m^3$] for those groups.

With the above modeled absorption and scattering (backscattering) coefficients, Hydrolight was used for the calculation of radiance distribution and then the AOPs, which include the nadir-viewed above-surface remote-sensing reflectance ($R_{rs}$), nadir-viewed subsurface remote-sensing reflectance ($r_{rs}$), and subsurface irradiance reflectance ($R$). In the Hydrolight runs, solar input was simulated with the Gregg and Carder [1990] model with marine aerosols, and the sky was assumed cloud free. A wind speed of 5 m/s was applied, and the water body was assumed homogeneous. Spectral bands were set from 400 to 800 nm, with a spacing of 10 nm. Inelastic scatterings (i.e. Raman scattering, chlorophyll fluorescence, etc.) were excluded.

The synthetic data set is compared with the *in situ* data set for consistency. Fig. 2.3a presents the range and variation of $R_{rs}(440)$ versus $a(440)$, whereas Fig. 2.3b presents the range and variation of $R_{rs}(410)/R_{rs}(440)$ versus $R_{rs}(490)/R_{rs}(555)$, for the two data sets. $R_{rs}(412)/R_{rs}(443)$ is used instead of $R_{rs}(410)/R_{rs}(440)$ for the *in situ* data set. We view the effects of these small wavelength differences are negligible. For both data sets, $a(440)$ is in a range of ~0.02 – 3.1 $m^{-1}$, while $R_{rs}(490)/R_{rs}(555)$ is in a range of ~0.3 – 5.2. Clearly, the two data sets generally agree with each other in variation and coverage. Some *in situ* data points, however, have higher $R_{rs}(410)/R_{rs}(440)$ ratios for $R_{rs}(490)/R_{rs}(555)$ around 1.0.

This synthetic data set certainly may not cover the variations of all possible natural waters. Because the models and parameters used in the simulation process are based on extensive field measurements, however, this synthetic IOP-AOP data set represents a wide range of variations that is encountered in the field.

In the following chapters (Chapter 4 – Chapter 12), a series of existing algorithms for the retrieval of IOPs from $R_{rs}(\lambda)$ are applied to both synthetic and *in situ* data sets, with retrieved absorption and/or backscattering coefficients compared with known (synthetic) or measured (*in situ*) values, respectively. To evaluate the performance of each algorithm, regression results (Type II [*Laws*, 1997]) and Root-Mean-Square-Error (RMSE) are calculated and tabulated for each property, in log space. RMSE is defined as

$$\mathrm{RMSE} = \left( \frac{\sum_{i=1}^{n} [\log(\mathrm{IOP}_i^{\mathrm{model}}) - \log(\mathrm{IOP}_i^{\mathrm{true}})]^2}{n-2} \right)^{1/2}, \qquad (2.1)$$

where $\mathrm{IOP}_i^{\mathrm{model}}$ stands for the $i^{\mathrm{th}}$ property derived from $R_{rs}(\lambda)$, $\mathrm{IOP}_i^{\mathrm{true}}$ for the $i^{\mathrm{th}}$ property known either from simulation or from *in situ* measurements, and $n$ is the number of valid retrievals. It is necessary to point out that, due to architecture difference, different algorithms may derive slightly different sets of IOPs from the same $R_{rs}(\lambda)$. Also, for the same IOP product, due to the different settings of the algorithms, not all algorithms may derive valid retrievals for a given $R_{rs}(\lambda)$ spectrum. Such non-valid retrievals are

then excluded in the performance analysis, and result smaller number of data size and likely better statistical results.

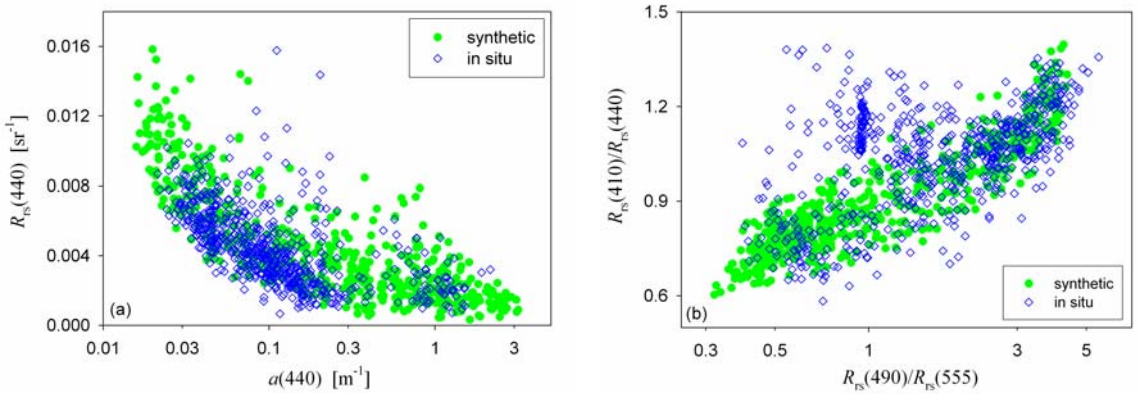


Figure 2.3. Comparison between *in situ* and synthetic data sets. (a) Ranges and variations of $R_{rs}(440)$ and $a(440)$. (b) Ranges and variations of $R_{rs}(410)/R_{rs}(440)$ and $R_{rs}(490)/R_{rs}(555)$.

## Chapter 3. Uncertainties in the Products of Ocean Color Remote Sensing

Emmanuel Boss and Stephane Maritorena

Data products retrieved from the inversion of *in situ* or remotely sensed ocean color data are generally distributed or reported without estimates of their uncertainties. The accuracy of inversion products such as chlorophyll or IOPs is frequently evaluated by comparison with *in situ* measurements but these analyses are not always sufficient to determine the level of uncertainty of an ocean color product. This is particularly true for remote sensing data where match-up analyses [*McClain et al.*, 2000] (http://seabass.gsfc.nasa.gov/matchup_results.html) can only be performed for an infinitesimal fraction of a sensor's records. Although very useful, these analyses cannot provide reliable estimates of how ocean color uncertainties vary with time and/or space. Moreover, because the uncertainties of the input data (for example the normalized water leaving radiance, NWLR) vary in space and time, the uncertainties of the output products cannot be simply reported as a single global value unless it is intended to provide general bounds. Some ocean color products are also used as input to other models (for example, to calculate primary production or to assimilate phytoplankton carbon into ecosystem models) for which uncertainty budget cannot be properly established without knowledge of the uncertainties associated with the input data. It is thus important that the variations of the uncertainty in NWLR and in the products derived from them are documented in time and space. This section discusses the various types of uncertainties present in ocean color data or products and stresses recent approaches that allow uncertainties of satellite ocean color products to be estimated on a pixel-by-pixel basis.

### 3.1 Sources of Uncertainties

a. Uncertainties in *in situ* measurements (NWLR, $R_{rs}$, Chl, IOP)

*In situ* data are used for algorithm development and for validation of algorithms and data products. While *in situ* measurements are frequently considered as "the reference" to which other data (e.g. satellite data) are compared with, they contain significant levels of uncertainties caused by various experimental and environmental factors. Calibration, dark signal, data processing, deployment strategy, sea and sky states all introduce uncertainties in the radiometric measurements [*Hooker and Maritorena*, 2000; *Hooker et al.*, 2001; *Siegel et al.*, 1995]. Close compliancy to establish measurement protocols (e.g. Mueller and Austin, [1995] and follow up) along with regular and rigorous calibrations and good characterization of instruments are key to the minimization of uncertainties in *in situ* measurements. Measurements of biogeochemical variables have their own set of difficulties and resulting uncertainties [*Claustre et al.*, 2004; *Mitchell et al.*, 2000; *Van Heukelem et al.*, 2002]. Most of the data sets that are publicly available (e.g., SeaBASS) do not contain information regarding the estimated uncertainties of the various variables they contain (e.g., the differences between the triplicate chlorophyll measurements and the uncertainties in the radiometer reading, based on its variability through the sampling period and its calibration history). It is frequently assumed that the uncertainties of *in situ* data are small and in any case much smaller than the uncertainties arising from the natural spatial/temporal variability of a given variable.

Another uncertainty arises from the fact that the match-up field data usually characterize an area of the 1-10 m while the satellite spatial scale is often 100-1000 m. This environmental mismatch in scales introduces an uncertainty that is often hard to quantify. Also, satellite measurements represent a water-column weighted average [*Gordon and Clark*, 1980; *Sathyendranath and Platt*, 1989; *Zaneveld et al.*, 2005a], while *in situ* measurements usually come from discrete depths. Therefore, for vertically inhomogeneous waters, uncertainties arise when the two are compared with each other. Some sampling platforms such as on-line sampling from steaming vessels, undulating vehicles, gliders, and AUVs are likely to be fruitful approaches in quantifying these uncertainties.

b. Uncertainties in satellite measurements (NWLR)

Various sources of random and systematic error contribute to disagreements between measured NWLRs and their actual values. Uncertainties in the NWLRs are introduced through a variety of factors such as pre-launch characterization of the sensor, atmospheric and bi-directional corrections, and uncertainties in the monitoring of the changes in the sensor's performance. Errors in geo-location, contamination with light emanating from adjacent pixels or other factors like white caps can also add to this uncertainty. The calibration/validation activities of each ocean color mission are designed to assess and minimize the magnitude of this uncertainty (and remove any bias). Pre-launch and on-orbit characterization of the sensors (e.g., measurements of reflected Sun and/or Moon light) along with vicarious calibrations (e.g., the MOBY buoy) and match-up analyses are the major procedures used to quantify NWLR's uncertainties.

The calibration/validation activities and the reduction of the uncertainties in the derived NWLR should be one of the primary tasks of space agencies providing the ocean color data and much effort must be invested in minimizing it for various missions. In the remainder of this chapter we will therefore assume the uncertainty in the NWLR is known and documented, although at present failure of atmosphere correction still dominates errors in NWLR of coastal waters.

c. Uncertainties and assumptions in the functional relationship that links NWLR and IOP and in the inversion procedure used to derive the products

Uncertainties in the products derived from the inversion of NWLR, however, do not benefit from the same level of effort. In what follows we will address these uncertainties with reference to the type of algorithm designed to produce them, separating between empirical and semi-analytical inversion algorithms. The approaches used in some recent works to provide ocean color product uncertainties are also described.

1) Obtaining uncertainties in products based on empirical algorithms

Empirical algorithms are developed from data sets where *in situ* radiometry and a to-be-derived product (e.g., chlorophyll, POC) have been collected at the same spot of the ocean and within a narrow period of time. A regression is most often performed to obtain the 'best-fit' function between the two variables and define the formulation that relates the two quantities. The type of regression used to relate two variables is relevant to the uncertainty discussion because regression methods work under different assumptions about uncertainties in the data involved. Type-I regressions [*Laws*, 1997] are the most frequently used and they are based on the assumption that only the dependent variable (i.e. y, the product) has an uncertainty, while the independent variable (i.e. x, the input data) is error free. In Type-I regressions, the individual uncertainties in the input data are not taken into account and it is generally assumed that the relative error in the variable is constant. Conversely, Type-II regressions [*Laws*, 1997; *Press et al.*, 1992] assume that both variables have uncertainties and are thus better adapted for ocean color where substantial uncertainties frequently exist in the variables involved (e.g., reflectance ratio, chlorophyll).

An empirical algorithm is as good as the data it is based on and on how representative the data are of the environment or bio-optical provinces where the algorithm is to be applied. *In situ* data sets are often geographically and seasonally biased due to constraints in oceanic cruise's timing and locations [*Claustre and Maritorena*, 2003].

In general, it is crucial that data sets used in the development (or validation) of an ocean color algorithm have complete information about the location and time at which the data were collected and about their quality (i.e. associated uncertainties). The geographical and temporal extent of a data set determines the water types where the algorithm can be applied whereas uncertainties in products require information on uncertainties in the input data.

For empirical algorithms, the dispersion of the y-axis data (i.e. the product) around the "mean" relationship of the resulting algorithm provides, to some degree, information about the uncertainties that can be expected at any given x-axis value (i.e. the input data). However, this only represents the

uncertainties associated with the data set used in the regression and cannot be generalized unless the data set fully encompasses all the natural variability that exists for the water types included. Ideally, to evaluate the uncertainties of an empirical algorithm one needs a different data set than that with which the algorithm was developed; the statistics of the differences between the inverted product and the measured products in this independent data set can then be used to evaluate the uncertainties in the product. Additionally, an uncertainty propagation analysis to evaluate the effect of the uncertainties in the NWLR on the output has to be carried out to establish whether or not this uncertainty is a significant source for uncertainty in the product (e.g., to what extent is a 5% relative uncertainty in NWLR at 440 and 555 nm affects the IOPs retrieved).

In the case of neural network (NN) based algorithms uncertainties should be determined from a rigorous statistical approach. Aires et al. [2004] provided an example for such an approach to products derived from remote sensing (other than ocean color). They use a Bayesian technique to evaluate the uncertainties in the NN parameters which are then used to compute the uncertainties in the outputs.

Another way to determine whether the measured reflectance spectrum is within the domain of the bio-optical models used to simulate reflectance spectrum, which in turn were used to train a neural network, has been developed for the Medium Resolution Imaging Spectrometer (MERIS) [*Doerffer and Schiller*, 2000; *Krasnopolsky and Schiller*, 2003]. For this purpose one network is trained to determine concentrations from the eight MERIS bands together with the solar and viewing zenith angles and the azimuth difference between viewing and sun direction (see Chapter 6, this report). A second, forward, network is trained with the same data set, which takes the derived concentrations as input and produces reflectances. The deviation calculated as the $Chi^2$ [*Sokal and Rohlf*, 1981] over all eight bands between the measured and the computed spectrum is then used as an indicator if the measured spectrum is within the training range and thus within the scope of the algorithm. In the case of the MERIS ground segment, a flag is raised whenever the $Chi^2$ deviation exceeds a certain threshold. However, the $Chi^2$ value can also be used as an uncertainty measure. Furthermore, a technique has been developed [*Schiller and Doerffer*, 2005], which combines the neural networks with an optimization procedure, to estimate the uncertainty of a product on a pixel-by-pixel basis.

2) Obtaining uncertainties in products based on semi-analytical models

Semi-analytical models or algorithms are based on the premise of a known relationship (derived from the radiative-transfer theory) between NWLR (or a function of it) and IOP (generally the absorption, $a$, and the backscattering, $b_b$, coefficients). These models contain some level of empiricism in the way IOPs are parameterized (i.e. how their variations and spectral shapes are formulated) and they also use simplified assumptions for some of their components (see Chapter 1). The inversion of semi-analytical models generally allows the simultaneous retrieval of several variables contained in the IOP terms. Similarly to empirical algorithms, semi-analytical models are affected by uncertainties in the NWLRs but they are also influenced by uncertainties associated with the chosen relationship between NWLR and IOPs and uncertainties resulting from the assumptions used in their formulation.

Sensitivity analyses are frequently used to assess how assumptions used to describe the component terms of a model affect retrievals [*Garver and Siegel*, 1997; *Hoge and Lyon*, 1996; *Roesler and Perry*, 1995]. Although very useful, this approach does not allow the determination of a product's uncertainty on a case-by-case (or pixel-by-pixel) basis but rather provides a general uncertainty estimate. To our knowledge, only two methods have recently been used with ocean color data that can estimate the uncertainties of products retrieved by the inversion of a semi-analytical model on a case-by-case basis. The first one [*Maritorena and Siegel*, 2005] is a nonlinear adaptation of the calculation of confidence intervals in linear regressions. Roughly, this method is based on the projection of the residuals between the observed and reconstructed (from the inverted variables) NWLR in the solution (i.e. retrieved variables) space [*Bates and Watts*, 1988].

A recent study [*Wang et al.*, 2005] suggests another approach to compute uncertainties of the retrieved variables. In this approach, each of the variables to be retrieved has a predefined set of spectral shapes and the model is inverted for each of the possible combinations of these spectral shapes resulting

in an extensive set of possible solutions. These results are then filtered in order to only keep the "realistic" (e.g., positive) solutions that can spectrally reproduce closely the input NWLR spectrum (within a pre-described difference from the NWLR based on the uncertainties in NWLR and the uncertainties in the theoretical relationship between NWLR and IOP). The final value for each inversion product and its associated uncertainty are then obtained from the statistics (median and percentiles) on the acceptable solution subset. The key steps in this approach are the choice of the acceptance criteria for the solutions (e.g., what is the acceptable difference between observed NWLR and that reconstructed from retrieved IOP) and the choice of range in possible shapes for the spectrum of each individual IOP. The two methods described above don't produce the same kind of uncertainties and thus they are not directly comparable. Both approaches have benefits and limitations. For example, the Maritorena and Siegel [2005] approach always returns a value for the confidence interval of the retrieved product because the calculations do not depend on spectral criteria but on the sum of the residuals (weighted by the spectral uncertainties of the input data, if they are known). On the other end, this approach does not take into account the uncertainties caused by the model assumptions. In the Wang et al. [2005] approach, uncertainties in the model and data are included in the spectral agreement criteria but the inversion may fail to find any solution that satisfies this criteria. Although, it uses an efficient linear matrix inversion technique [*Hoge and Lyon*, 1996], the Wang et al. [2005] method is also more computationally demanding (computational demands increase with numbers of possible combinations of different shapes of IOPs).

### 3.2 Summary

While some rough and general uncertainty estimates for ocean color products are available through match-up analyses, uncertainties are generally not provided on a per data point basis. This has caused many users to use ocean color products as a qualitative descriptor of patterns rather than a quantitative variable. Others use these products in biogeochemical models (e.g., computing primary productivity) without being able to propagate uncertainties.

For some ocean colour missions, such as for MERIS, a sophisticated flagging system has been developed. It computes on a pixel-by-pixel basis indicator for the reliability of a product by regarding different possible error sources including sun glint, failure in the atmospheric correction, high turbidity in the water, etc. A flag for each possible problem is raised if the uncertainty value exceeds a certain threshold. By this the user gets a warning and has to decide if he can accept this pixel for further computations, etc.

Here we briefly review some of the uncertainties present in ocean color data and presented different approaches to establish uncertainties in products of ocean color remote sensing for either empirical or semi-analytical algorithms. The procedures described above are not complicated and their full application benefits from the knowledge of uncertainties in the input data. Use of such approaches will help the ocean color community to establish quantitative confidence in the remote sensing products.

## Chapter 4. Simple Algorithms for Absorption Coefficients

ZhongPing Lee, Stephane Maritorena, Andrew H. Barnard

### 4.1 One-Step Spectral Ratio Algorithm

4.1.1. General description

Similar to the empirical approach of deriving chlorophyll concentration from ocean color data, the simplest way to derive absorption coefficients from $R_{rs}(\lambda)$ is by empirical relationships. This kind of approach does not require knowledge of the fundamental relationships between $R_{rs}$ and IOPs, but requires an adequate data set to develop the empirical coefficients. For the derivation of total absorption coefficient at 440 nm, based on limited (63 data points) measurements, Lee et al. [1998b] developed an empirical spectral-ratio algorithm from the spectral ratios of $R_{rs}(\lambda)$. To obtain better fit between measured and algorithm-derived value, the algorithm uses quadratic polynomials with two spectral ratios:

$$\log\big(a(440)\big) = A_0 + A_1\rho_{25} + A_2{\rho_{25}}^2 + B_1\rho_{35} + B_2{\rho_{35}}^2, \tag{4.1}$$

where $\rho_{25}$ and $\rho_{35}$ are

$$\rho_{25} = \log\left(\frac{R_{rs}(440)}{R_{rs}(555)}\right),\ \rho_{35} = \log\left(\frac{R_{rs}(490)}{R_{rs}(555)}\right). \tag{4.2}$$

Values of $A_{0,1,2}$ and $B_{1,2}$ in Eq. 4.1, derived by least-square fitting, are -0.674, -0.531, -0.745, -1.469, and 2.375, respectively [*Lee et al.*, 1998b].

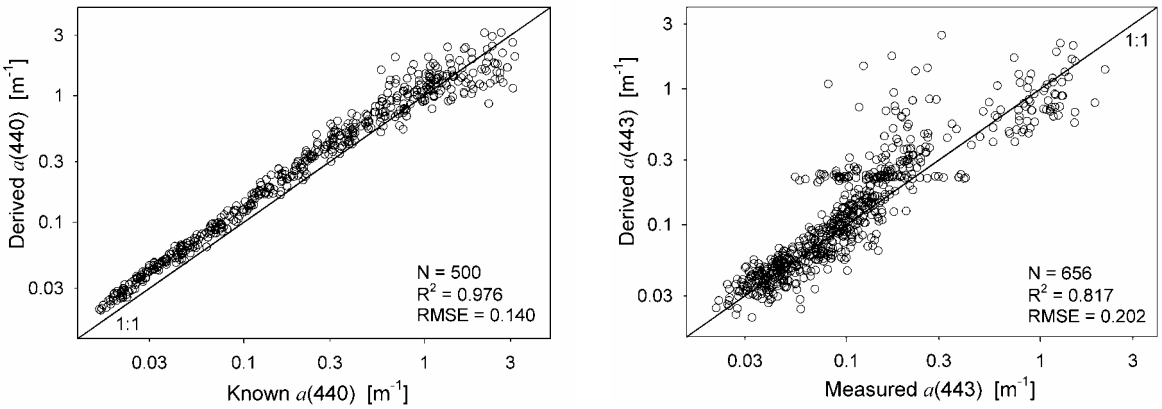


Figure 4.1. Comparison between algorithm-derived and known IOP, with algorithm results from the Lee et al. [1998b] empirical approach. (left) $a(440)$ of the synthetic data set; (right) $a(443)$ of the *in situ* data set.

4.1.2. Results and discussion when applied to the IOCCG data sets

With $R_{rs}$ values at 440, 490 and 555 nm (or nearby wavelengths) as inputs, values of $a(440)$ were calculated from Eqs. 4.1 and 4.2. Figure 4.1 compares the derived and known $a(440)$ values for the synthetic and the *in situ* data sets, respectively. For the synthetic data set, this empirical algorithm systematically overestimated $a(440)$ for most of the data, though good correlation of determination ($R^2$ = 0.976) was achieved between algorithm derived and known $a(440)$ values (see Table 4.1). Such a result suggests that the empirical coefficients, derived by forcing Eq. 4.1 derived $a(440)$ to match a limited number of $a(440)$ from field measurements, were biased by data from those measurements. It is likely that when more high-quality data are available the coefficients in Eq. 4.1 could be fine tuned and the estimation of $a(440)$ from $R_{rs}(\lambda)$ by simple ratios could be improved.

For the *in situ* data set, the $R^2$ value is 0.817 and the RMSE is 0.202 (see Table 4.2), indicating that algorithm-derived $a(440)$ are quite consistent with $a(440)$ values from water samples. The larger differences are likely due to uncertainties associated with both $R_{rs}(\lambda)$ and $a(440)$ in the *in situ* measurements (also see Chapter 3 for discussions regarding uncertainties).

## 4.2 Spectral Curvature Algorithm

4.2.1 General description

A simplistic 3-wavelength ratio method to test *in situ* measurements of remote sensing reflectance and the absorption coefficient for closure was developed by Barnard et al. [1999]. The purpose of the method was to minimize the influence of parameters of the radiative transfer equation that are difficult to determine *in situ*, e.g., backscattering. This method uses two ratios with three different wavelengths ($\lambda_1$ = 440, $\lambda_2$ = 490, and $\lambda_3$ = 555 nm) of $R_{rs}$ to minimize the spectral dependence of the backscattering coefficient as well as the angular dependence of the underwater light field. Based on the semi-analytical relationship between $R_{rs}$ and $b_b/a$ [*Morel and Gentili*, 1993], one can derive the following relationship using ratios of three different wavelengths:

$$R_{rs3}(\lambda_1,\lambda_2,\lambda_3)=\frac{R_{rs}(\lambda_1)}{R_{rs}(\lambda_2)}\Big/\frac{R_{rs}(\lambda_2)}{R_{rs}(\lambda_3)}\cong\frac{g(\lambda_1)g(\lambda_3)}{[g(\lambda_2)]^2}\frac{b_b(\lambda_1)b_b(\lambda_3)}{[b_b(\lambda_2)]^2}\frac{[a(\lambda_2)]^2}{a(\lambda_1)a(\lambda_3)}. \tag{4.3}$$

As the spectral behavior of $g$ parameter is nearly linear over these wavelengths, only a small error is induced by assuming that the triple ratio of $g$ is equal to 1.0. The triple wavelength ratio of the backscattering coefficient in Eq. 4.3, evaluated over typical oceanic conditions where the backscattering ranges from particle dominated to water dominated and where the spectral dependency of particle backscattering ranges from 0 to 2, varies from 0.93 to 1.02. Thus by choosing a constant value equal to 0.975 for the $b_b$ ratio term in Eq. 4.3, a maximum error of 4.5% is made for most oceanic conditions.

Substitution of the assumed constant values of $g$ triple ratio (= 1.0) and the backscattering triple ratio (= 0.975) into Eq. 4.3 results in a model that can be used directly to compare *in situ* (and modeled) measurements of $R_{rs}(\lambda)$ and $a(\lambda)$.

$$R_{rs3}(\lambda_1,\lambda_2,\lambda_3)\cong 0.975\frac{[a(\lambda_2)]^2}{a(\lambda_1)a(\lambda_3)}. \tag{4.4}$$

If functional relationships between the absorption coefficients exist at the selected three wavelengths such that the absorption at $\lambda_1$ and $\lambda_3$ can be defined solely in terms of the absorption at $\lambda_2$, the above formulation can be used to invert the remotely sensed reflectance to determine the spectral absorption at the selected three wavelengths.

While any functional form for the spectral absorption coefficient can be utilized, Barnard et al. [1999] has shown that the absorption at 440 (originally it was 443 nm) and 555 nm is significantly linearly correlated to the absorption at 490 nm, such that;

$$\begin{aligned} a(440) &= f_1[a(490)] = A[a(490)] + B, \\ a(555) &= f_2[a(490)] = C[a(490)] + D, \end{aligned} \tag{4.5}$$

where values of $A$, $B$, $C$, and $D$ are 1.561, -0.012, 0.319, and 0.067, respectively.

Substitution of these functional forms into Eq. 4.4 thus allows for the absorption coefficient at 490 nm (and then at 440 and 555 nm) to be derived solely from $R_{rs}(\lambda)$,

$$a(490)=\frac{-(AD+BC)-\left[(AD+BC)^2-4\left(AC-\dfrac{0.975}{R_{rs3}}\right)(BD)\right]^{0.5}}{2\left(AC-\dfrac{0.975}{R_{rs3}}\right)}. \tag{4.6}$$

4.2.2. Results and discussion when applied to the IOCCG data sets

With $R_{rs}(\lambda)$ values at 440, 490 and 555 nm, $a(490)$ and $a(440)$ are calculated from $R_{rs3}$ based on Eq. 4.5 and Eq. 4.6. Figure 4.2 (also see Tables 4.1 and 4.2) compares model-derived $a(440)$ versus known $a(440)$ values. For the synthetic data, the model-derived values are seems systematically higher in the lower end ($a(440) < 0.05$ m$^{-1}$) and systematically lower in the higher end ($a(440) > 0.3$ m$^{-1}$), indicating a mismatch between data used for algorithm development and data used for test. However, when the algorithm was applied to the *in situ* data set, no such systematically bias was found, though there were 14 points that no valid results were obtained.

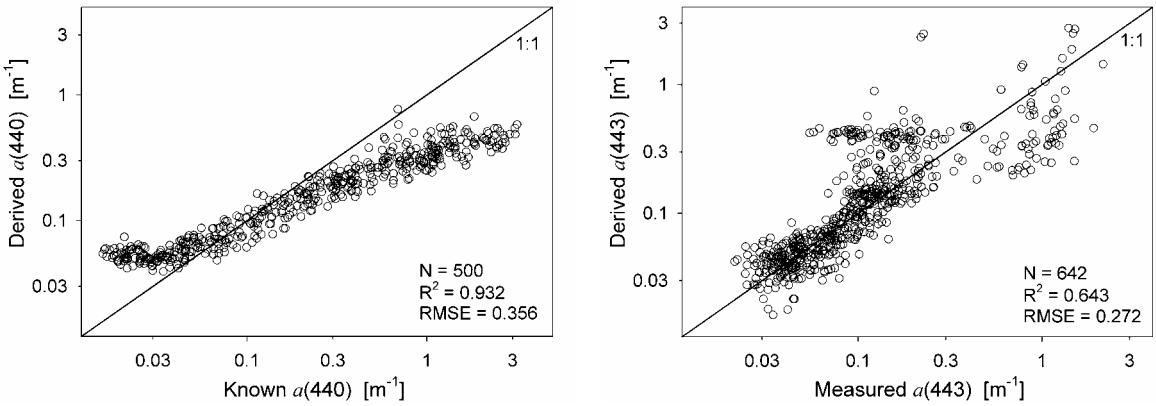


Figure 4.2. As Fig.4.1, with results from the spectral-curvature algorithm [*Barnard et al.*, 1999]. (left) $a(440)$ of the synthetic data set; (right) $a(443)$ of the *in situ* data set.

### 4.3 Spectral-Ratio Algorithm with Chl as A Intermediate Link

4.3.1. General description

Using Chl derived from spectral-ratio of $R_{rs}(\lambda)$, and a relationship between $K_d$ and *Chl*, along with an analytical expression that expresses $a$ as a function of $K_d$ and $R$, value of $a$ can be derived from spectral ratios of $R_{rs}$ [*Morel and Maritorena*, 2001]. Specifically, values of Chl is first derived from the current operational Chl algorithm for SeaWiFS (OC4v4) [*SeaWiFS*, 2000],

$$Chl = 10^{r_0 + r_1 \rho + r_2 \rho^2 + r_3 \rho^3} + r_4 , \tag{4.7}$$

where $\rho = \log[\max(R_{rs}(440,490,510))/R_{rs}(555)]$, and values of $r_{0\text{-}4}$ are 0.366, -3.067, 1.93, 0.649, and -1.532, respectively.

From Eq. 4.7 derived Chl, $K_d(\lambda)$ can be calculated [*Morel*, 1988; *Morel and Maritorena*, 2001]:

$$K_d(\lambda) = K_w(\lambda) + \chi(\lambda) Chl^{e(\lambda)}, \tag{4.8}$$

with the values of $K_w(\lambda)$, $\chi(\lambda)$ and $e(\lambda)$ known from statistical analysis of field measurements (see Table 2 of *Morel and Maritorena* [2001]).

Semi-analytically, there is [*Morel*, 1988; *Morel and Maritorena*, 2001]

$$a(\lambda) = \frac{0.9 K_d(\lambda)[1 - R(\lambda)]}{1 + 2.25 R(\lambda)}, \tag{4.9}$$

and

$$R(\lambda) \approx \frac{n_w^{\,2}}{t^2} Q\, R_{rs}(\lambda). \tag{4.10}$$

Here $t$ is the sea-air transmittance, $n_w$ is the index of refraction of the water, and $Q$ (sr) accounts the conversion of irradiance to radiance. The quantity $Qn_w^2/t^2$ represents the conversion between radiance reflectance to irradiance reflectance and the air-sea interface effect, and approximates 6.8 for the remote sensing domain [*Morel and Gentili*, 1993]. Since value of $R$ is generally less than 0.1 and only plays a

secondary role in Eq. 4.9, the variation in $Qn_w^2/t^2$ does not affect much the value of $a(\lambda)$ derived by Eq. 4.9. Therefore, for a given $R_{rs}(\lambda)$, absorption coefficients can be calculated following the Eqs. 4.7 – 4.10.

4.3.2. Results and discussion when applied to the IOCCG data sets

With $R_{rs}(\lambda)$ values at 440, 490, 510 and 555 nm, values of $a(410)$, $a(440)$ and $a(490)$ were calculated from Eqs. 4.7-4.10. The comparison of these derived values versus known (or measured) values is presented in Tables 4.1 and 4.2. Figures 4.3 shows model-derived $a(440)$ with known $a(440)$. Apparently, this empirical procedure performed very well, especially for the synthetic data set with $a(440)$ less than 0.2 $m^{-1}$. Due to data range used to derive the parameters in Eq. 4.7 and Eq. 4.8, this empirical procedure with the present coefficients, however, apparently underestimates absorption when $a(440)$ value is greater than 0.2 $m^{-1}$.

Similar to the other two algorithms when applied to the *in situ* data set, the difference between model-derived $a(440)$ and known $a(440)$ is larger. And, $a(440)$ is apparently underestimated. Even so, an $R^2$ value of 0.821 and an RMSE of 0.210 were achieved.

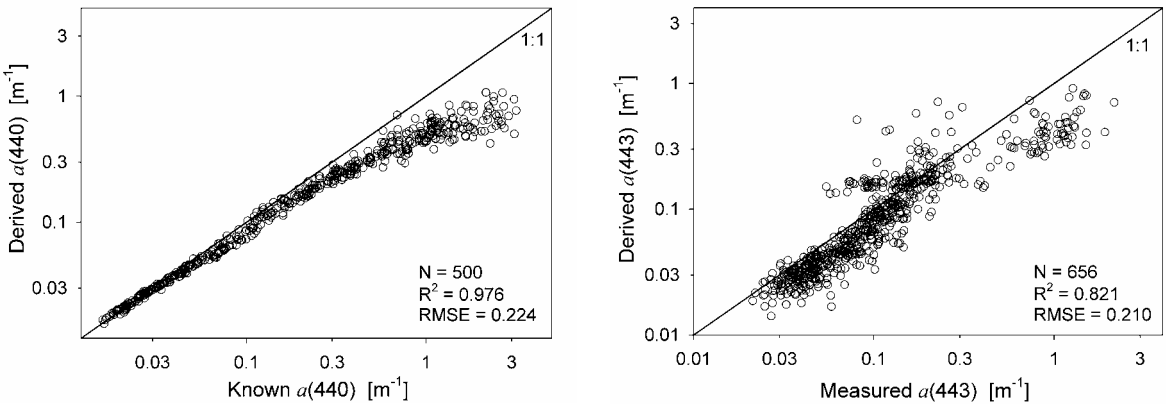


Figure 4.3. As Fig.4.1, with results from the spectral-ratio and Chl as a intermediate link [*Morel and Maritorena*, 2001]. (left) $a(440)$ of the synthetic data set; (right) $a(443)$ of the *in situ* data set.

## 4.4 Conclusions

Empirical and semi-empirical algorithms are easy and straightforward for data processing. However, because the empirical coefficients contained in empirical algorithms are derived from data sets that not necessarily represent all natural variations, the performance of such algorithms is always subject to compatibility between the waters under study and the waters from which data were used for the algorithm development. It is critical to check this consistency if robust results are desired and if such kinds of algorithms are going to be applied to wide areas.

Table 4.1: RMSE and regression (Type II) results of the synthetic data set ($\theta_0 = 30°$). N is the number of data tested, while n is the number of valid retrieval by an algorithm.

| | N | n | intercept | slope | $R^2$ | RMSE | bias |
|---|---|---|---|---|---|---|---|
| *a*(440), L98[a] | 500 | 500 | 0.050 | 0.939 | 0.976 | 0.140 | 0.091 |
| *a*(440), B99[b] | 500 | 500 | -0.466 | 0.538 | 0.932 | 0.356 | -0.151 |
| *a*(490), B99 | 500 | 500 | -0.488 | 0.574 | 0.948 | 0.281 | -0.119 |
| *a*(410), MM01[c] | 500 | 500 | -0.368 | 0.747 | 0.976 | 0.295 | -0.221 |
| *a*(440), MM01 | 500 | 500 | -0.299 | 0.792 | 0.976 | 0.224 | -0.156 |
| *a*(490), MM01 | 500 | 500 | -0.256 | 0.815 | 0.965 | 0.169 | -0.096 |

[a]: Lee et al. [1998b]
[b]: Barnard et al. [1999]
[c]: Morel and Maritorena [2001]

Table 4.2: RMSE and regression (Type II) results of the *in situ* data set. N is the number of data tested, while n is the number of valid retrieval by an algorithm.

| | N | n | intercept | slope | $R^2$ | RMSE | bias |
|---|---|---|---|---|---|---|---|
| *a*(443), L98 | 656 | 656 | 0.140 | 1.081 | 0.817 | 0.202 | 0.061 |
| *a*(443), B99 | 656 | 642 | 0.085 | 1.039 | 0.643 | 0.272 | 0.047 |
| *a*(490), B99 | 656 | 642 | 0.152 | 1.080 | 0.626 | 0.255 | 0.062 |
| *a*(412), MM01 | 656 | 656 | -0.228 | 0.911 | 0.817 | 0.237 | -0.147 |
| *a*(443), MM01 | 656 | 656 | -0.158 | 0.954 | 0.821 | 0.210 | -0.113 |
| *a*(490), MM01 | 656 | 656 | -0.117 | 0.949 | 0.808 | 0.171 | -0.059 |

## Chapter 5. Inversion of IOP based on $R_{rs}$ and Remotely Retrieved $K_d$

Hubert Loisel and Antoine Poteau

### 5.1 Background

Based on Monte Carlo and Hydrolight simulations we developed an inverse algorithm to retrieve the total absorption, scattering, and backscattering coefficients from the irradiance reflectance just beneath the surface ($R(0^-)$) and the mean vertical diffuse attenuation coefficient over the first optical depth ($<K_d>_1$) [*Loisel and Stramski*, 2000]. Note that while the particulate backscattering coefficient, $b_{bp}$, is directly obtained from $b_b$ by removing the effect of pure water, our algorithm does not intend to decompose $a$ into its different components such as the absorption by phytoplankton or by colored dissolved organic matter. This task can be done in a second step (e.g., Chapter 10), by assuming some spectral models for pigments and gelbstoff absorption coefficients, such as those already available in the literature [*Bricaud et al.*, 1995; *Kirk*, 1994; *Kopelevich and Burenkov*, 1977], and using least-square fitting methods or equivalent. The major motivation for the development of our algorithm was the assessment of total IOP from basic radiometric measurements by the means of a simple and fast approach that does not require any assumption about the spectral shapes of $a$, $b$, and $b_b$. A detailed review of the methods used for solving the hydrologic-optics inverse problem was recently performed by Gordon [2002]. One of the differences among these methods concerns the input parameters they use. The choice of $R(0^-)$ and $<K_d>_1$ for our algorithm was motivated by the fact that they can be both estimated from satellite measurements of ocean color. Whereas $R(0^-)$ is linked to the above surface remote sensing reflectance ($R_{rs}$) in a fairly straight forward manner [*Mobley*, 1994], the retrieval of $<K_d>_1$ from space is based on empirical relationships [*Loisel et al.*, 2001b; *Mueller*, 2000]. Therefore, our algorithm does not require any spectral assumptions about IOPs, but does require spectral relationships between $<K_d>_1$ and $R_{rs}$, in the frame of remote sensing application. However, while $<K_d>_1$ is still empirically determined from $R_{rs}$, one can image a more sophisticated method to retrieve $<K_d>_1$ from space (such as an iterative scheme based on analytical relationships between $<K_d>_1$ and space retrieved IOP).

Here we test an improved version of our algorithm [*Loisel and Poteau, in prep*] with the IOCCG data sets (synthetic and *in situ*). After a brief overview of the model, we examine closure between data from both synthetic and *in situ* IOPs, and the retrieval of these IOPs using our model. Finally, these results are discussed, and compared to previous validation works performed with the Loisel and Stramski [2000] algorithm in various oceanic waters.

### 5.2 Output and Input Parameters

Output parameters of the model are $a$, $b$ and $b_b$ averaged over the first attenuation layer. Because the retrieval of $b$ is highly sensitive to the variations in the particle phase function, only $a$ and $b_b$ can reasonably be retrieved from $R_{rs}$. Here, we will therefore specifically focus on the retrieval of $a$ and $b_b$ at 410, 440, 490, and 550 nm. These wavelengths are common to almost all ocean color sensors (with, however, some slight spectral shifts depending on the sensor).

Input parameters of the model are $R(0^-, \lambda)$, $<K_d(\lambda)>_1$, and the sun zenith angle ($\theta_0$). Within the context of ocean color remote-sensing application, only $R_{rs}(\lambda)$ is available, and then both $R(0^-, \lambda)$ and $<K_d(\lambda)>_1$ have to be determined. The exact procedure to assess $R(0^-, \lambda)$ from $R_{rs}(\lambda)$ is given in Loisel et al. [2001]. This step accounts for the process of reflection and refraction of light at the air-water interface, and of the bi-directional effect as described in *Morel and Gentili* [1993]. To estimate $<K_d(\lambda)>_1$ from $R_{rs}(\lambda)$, we originally used an empirical relationship between $<K_d(490)>_1$ and $R_{rs}(490)/R_{rs}(555)$, such as the one developed by Mueller [2000]. $<K_d(\lambda)>_1$ was then estimated empirically from $<K_d(490)>_1$. Therefore, to estimate $a(410)$, $a(440)$, $a(490)$, $b_b(440)$, $b_b(490)$, and $b_b(550)$, we need $R_{rs}(410)$, $R_{rs}(440)$, $R_{rs}(490)$, and $R_{rs}(550)$. Moreover, because of the strong influence of incident light field at the air-sea interface on the $R_{rs}$-IOP relationships, our model does also necessarily accounts for the change of $\theta_0$.

### 5.3 Assumptions and Description

The radiative transfer simulations used for the development of our model were run for a infinitely deep ocean (no bottom albedo) with an optically homogenous water column, a nearly flat sea surface under no wind, and in absence of inelastic scattering process. Phase function was derived from a weighted sum of the molecular scattering and the particle scattering phase functions proposed by Mobley et al. [1993]. An iterative scheme was also developed for removing the Raman contribution, that is always present in natural environment, from $R(0^-)$. This correction will not be applied here for consistency with the other models presented in this report.

Our model is based on the following set of equations between $a(\lambda)$, $b_b(\lambda)$ and $<K_d(\lambda)>_1$, $R(0^-,\lambda)$ that can be applied to any wavelength:

$$a = \frac{\mu_w < K_d >_1}{\left[1 + (2.54 - 6.54\mu_w + 19.89\,\mu_w{}^2)\dfrac{R(0^-)}{1 - R(0^-)}\right]^{0.5}}, \tag{5.1}$$

$$b_b = < K_d >_1 10^{\alpha}\,[R(0^-)]^{\delta}. \tag{5.2}$$

The $\alpha$ and $\delta$ functions were given by:

$$\alpha = (-0.83 + 5.34\,\eta - 12.26\,\eta^2) + \mu_w(1.013 - 4.124\,\eta + 8.088\,\eta^2), \tag{5.3}$$

$$\delta = (0.871 + 0.4\,\eta - 1.83\,\eta^2). \tag{5.4}$$

Where $\eta$ is the ratio of the molecular scattering to the total scattering ($= b_w/b$), and $\mu_w$ is the cosine of the refracted solar beam angle just beneath the surface.

Some modifications of the original version of the model are performed for a better retrieval of $a$ and $b_b$ in the context of ocean color remote sensing application [*Loisel and Poteau*, in prep]. These modifications are briefly listed below:

i) The model directly accounts for $R_{rs}$ instead of $R(0^-)$

ii) We developed a new way to account for the effect of $\eta$ on the derivation of $a$ and $b_b$ from remote sensing (new parameterisations coupled with an iterative procedure). Note that the dependence of $\eta$ on the assessment of $a$ was not taken into account in the previous version of our model.

iii) We performed some slight modifications within the $\alpha$ parameterisation to accounts for some more realistic $\eta$-$b/a$ combinations at any given wavelength used by actual ocean color sensors.

iv) We used new formulations and parameterisations to determine $<K_d(\lambda)>_1$ from ratios of remote sensing reflectance:

$$q = R_{rs}(440)/R_{rs}(550), \tag{5.5}$$

$$< K_d(\lambda) >_1 = 10^{(\upsilon_1(\lambda)\log(q) + \upsilon_2(\lambda))/(\upsilon_3(\lambda) + \log(q))}. \tag{5.6}$$

$\upsilon_{1\text{-}3}$ are empirical parameters and are provided in Table 5.1 for the SeaWiFS bands.

### 5.4 Results

Using $R_{rs}(\lambda)$ values at 410, 440, 490 and 550 nm, IOPs retrieved from the above steps were compared with known (synthetic) or measured (*in situ*) values.

*a. Comparison with synthetic data*

Figure 5.1 as well as Table 5.2 presents the performance of our model using $R_{rs}(\lambda)$ and the sun angle as inputs to the calculation of the IOPs. In this case, the sun angle is at 30°. For the absorption coefficient at 410, 440, and 490 nm, the slope of the linear regression is very close to 1.0, and the coefficient of determination is very high ($R^2 \geq 0.94$). The RMSE values are 0.12, 0.119, 0.136, and 0.138 for $a(410)$,

$a(440)$, $a(490)$, and $a(550)$, respectively. Note that the performance of the model is slightly degraded at 550 nm compared to other wavelengths. The retrieval of the absorption coefficient at 550 nm is challenging as it is strongly dominated by absorption by pure sea water, and because variations of $R_{rs}$ are mostly due to the backscattering coefficient in this spectral domain. The RMSE values for $b_b(\lambda)$ at 440, 490, and 550 nm are very similar to those of $a(\lambda)$, but the slope slightly differ from 1.0 (0.902, 0.935 and 0.973 at 440, 490, and 550 nm, respectively). Note that the RMSE values for $b_b$ are almost similar for every wavelength. Also, the total absorption and backscattering coefficients are retrieved with the same precision when the sun angle is fixed at 60° (not shown here). Most of the $a(\lambda)$ and $b_b(\lambda)$ errors appear at the high end of the data range, where the retrieval of $<K_d(\lambda)>_1$ from $R_{rs}(\lambda)$ is generally much more doubtful. For instance, by restricting the data set to the $a(440)$ values lower than 0.3 $m^{-1}$, which includes most oceanic waters, the RMSE drops by a factor of 2 (from 0.119 to 0.058). The same remark holds at other wavelengths. When measured $<K_d(\lambda)>_1$ is explicitly taken into account as input parameter, the performance of the model is greatly enhanced. For example, the RMSE for $a(410)$, $a(440)$, $a(490)$, $a(550)$, and $b_b(490)$ are 0.0445, 0.0102, 0.0131, 0.0101, and 0.0324, respectively (not shown here).

*b. Comparison with in situ data*

Figure 5.2 and Table 5.3 show that there is a reasonably good closure between the modelled and the measured values of the absorption coefficients. The RMSE are always lower than 0.2. In the blue-green spectral domain the mean RMSE value is 0.166. Compared to the synthetic data set, the RMSE increases by a factor of 1.6, 1.6, and 1.24 at 412, 443, and 490, respectively. Note that, RMSE drops from 0.169 to 0.142 by restricting the data set to the $a(490)$ values lower than 0.3 $m^{-1}$. Interestingly, the RMSE at 550 is slightly better with the *in situ* data set, than with the synthetic data set.

## 5.5 Conclusions

The retrieval of both $a(\lambda)$ and $b_b(\lambda)$ is achieved with excellent accuracy in the blue green spectral region when both $R(0^-)$ and $<K_d>_1$ are measured (the mean RMSE value in this spectral domain is 0.0195 for the absorption coefficient). When only $R_{rs}$ is available as input parameter, the results are obviously degraded, but are still very satisfactory: for the synthetic data set, the mean RMSE value over the blue-green part of the spectrum for $a$ and $b_b$ is 0.128 and 0.134, respectively. By comparison with *in situ* data, one may emphasis that our model is able to predict $a$ with a mean RMSE value of 0.166 over the spectral domain of interest for ocean color related studies. The performance of our model is governed, to a certain extant, by the accuracy of the $<K_d>_1$ assessment from space. Different approaches are actually tested to improve the retrieval of $<K_d(\lambda)>_1$ from $R_{rs}(\lambda)$ (*Loisel and Poteau*, in prep). Preliminary results for the retrieval of both $a$ and $b_b$ are very promising.

The results presented here are consistent with previous comparisons performed in oceanic and coastal waters [*Dupouy et al.*, 2003; *Loisel et al.*, 2001b; *Melin et al.*, 2002]. For example, based on field data collected in waters off southern California, and in waters surrounding Europe, Loisel et al. [2001b] showed that the average value and the standard deviation of the relative difference between the measured and the retrieved absorption coefficients from 412 to 555 nm are 26% and 16%, respectively. The new version of the model significantly improves the retrieval of $a$ and $b_b$, especially in the green part of the spectrum and at the extreme values (Loisel and Poteau, in prep).

Table 5.1. Parameters for deriving $<K_d(\lambda)>_1$ from remote sensing reflectance (Eq.5.6).

| | $\upsilon_1$ | $\upsilon_2$ | $\upsilon_3$ |
|---|---|---|---|
| 410 | -4.7636 | -2.1269 | 3.1752 |
| 440 | -4.6216 | -2.3587 | 3.1235 |
| 490 | -3.6636 | -2.3116 | 2.5648 |
| 550 | -2.0152 | -1.5296 | 1.7751 |

Table 5.2. RMSE and regression (Type II) results between the derived and the known values of IOP for synthetic data and for $\theta_0 = 30°$. $R_{rs}(\lambda)$ at 410, 440, 490 and 550 nm are used as inputs for the derivation of IOP. N is the number of data tested, while n is the number of valid retrieval.

| | N | n | intercept | slope | $R^2$ | RMSE | bias |
|---|---|---|---|---|---|---|---|
| $a$(410) | 500 | 500 | 0.029 | 0.977 | 0.973 | 0.120 | 0.043 |
| $a$(440) | 500 | 500 | -0.007 | 0.990 | 0.966 | 0.119 | -0.001 |
| $a$(490) | 500 | 500 | -0.017 | 0.980 | 0.939 | 0.136 | 0.000 |
| $a$(550) | 500 | 500 | -0.067 | 0.927 | 0.818 | 0.138 | -0.002 |
| $b_b$(440) | 500 | 500 | -0.173 | 0.902 | 0.924 | 0.123 | 0.003 |
| $b_b$(490) | 500 | 500 | -0.114 | 0.935 | 0.917 | 0.140 | 0.007 |
| $b_b$(550) | 500 | 500 | -0.028 | 0.973 | 0.934 | 0.138 | 0.023 |

Table 5.3. RMSE and regression (Type II) results between the derived and the known values of IOP for *in situ* data. $R_{rs}(\lambda)$ at 412, 443, 490 and 555 nm are used as inputs for the derivation of IOP. N is the number of data tested, while n is the number of valid retrieval.

| | N | n | intercept | slope | $R^2$ | RMSE | bias |
|---|---|---|---|---|---|---|---|
| $a$(412) | 656 | 656 | -0.052 | 1.013 | 0.847 | 0.186 | -0.064 |
| $a$(443) | 656 | 656 | -0.108 | 0.997 | 0.842 | 0.198 | -0.105 |
| $a$(490) | 656 | 656 | -0.122 | 0.953 | 0.823 | 0.169 | -0.069 |
| $a$(555) | 656 | 656 | -0.126 | 0.897 | 0.670 | 0.111 | -0.017 |

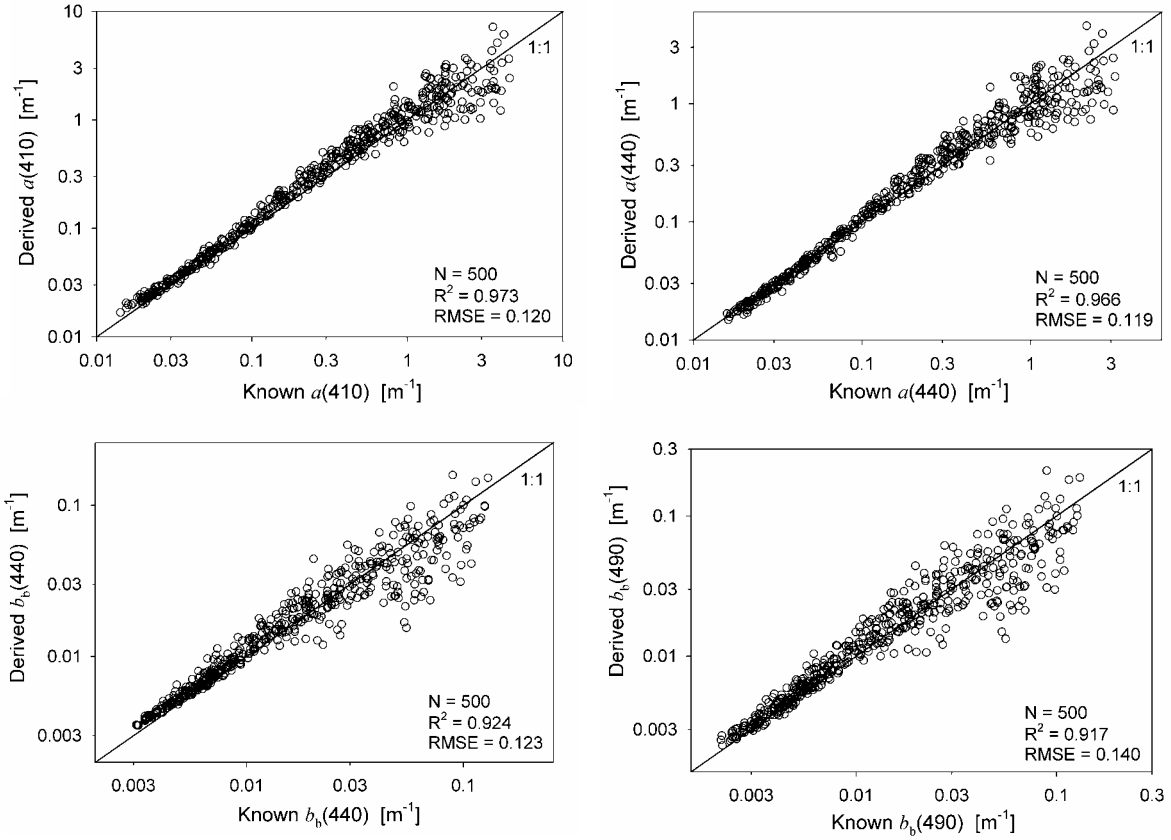


Figure 5.1. Comparison of the derived total absorption coefficients with the synthetic data, for a sun zenith angle at 30°, and at different wavelengths. $R_{rs}(\lambda)$ at 410, 440, 490 and 550 nm are used as inputs for the derivation of $a$ and $b_b$.

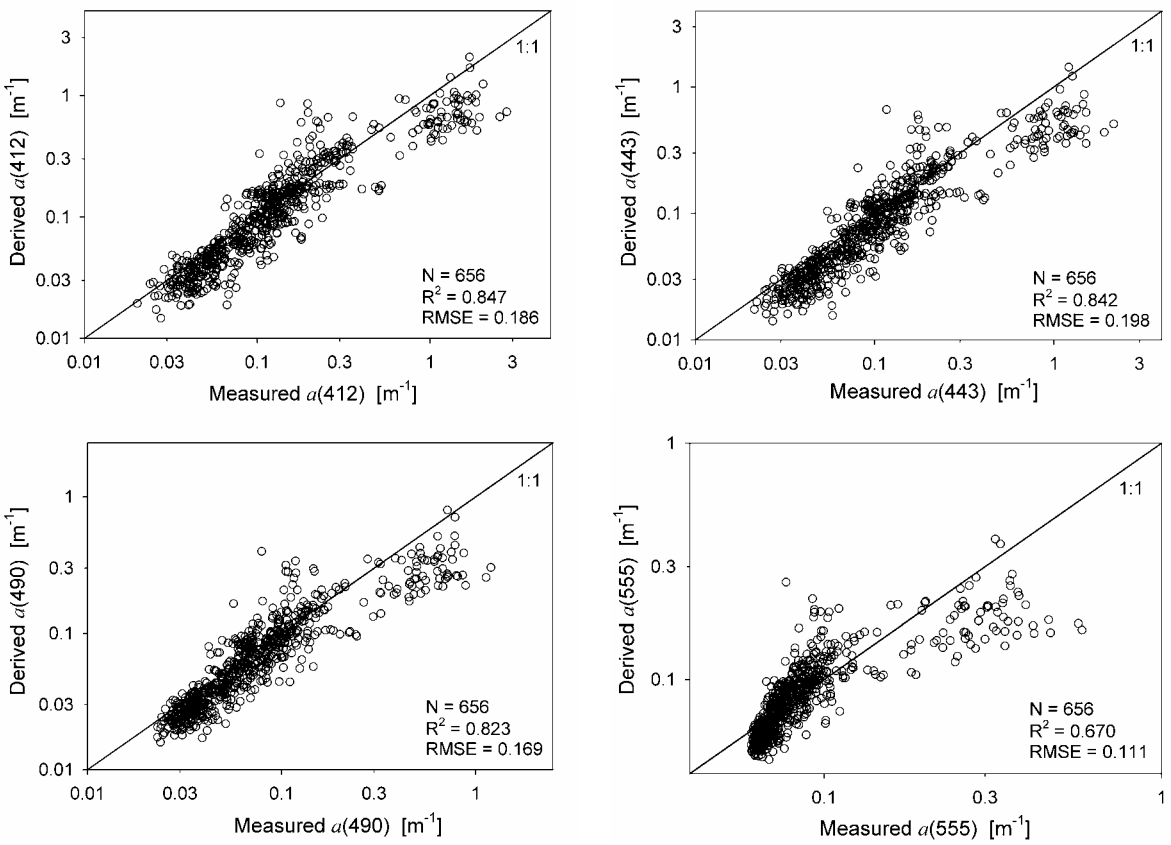


Figure 5.2. Comparison of the derived and the measured total absorption coefficients at different wavelengths, *in situ* data. $R_{rs}(\lambda)$ at 412, 443, 490 and 555 nm are used as inputs for the derivation of $a$.

## Chapter 6. The MERIS Neural Network Algorithm

Roland Doerffer and Helmut Schiller

### 6.1 Introduction

In this chapter we present the results of the MERIS Case 2 water algorithm for the IOCCG algorithm inter-comparison. This algorithm is an artificial neural network (aNN) inversion procedure [*Doerffer et al.*, 2002; *Doerffer and Schiller*, 2000; *Doerffer and Schiller*, 2006; *Schiller and Doerffer*, 2005], which is used in the ground segment processor of MERIS. This instrument is operated on board the Earth observation satellite ENVISAT of the European Space Agency (ESA), which was launched on March 1, 2002. The aNN algorithm was selected because of its capability to invert directional water leaving radiance reflectance directly into absorption and scattering coefficients or concentrations of different constituents as present in coastal waters with high efficiency for mass production. Due to the fixed architecture of the aNN only the simulated IOCCG data set could be processed for inter-comparison.

### 6.2 Description of the MERIS Case 2 Water Algorithm

The MERIS Case 2 water algorithm is a neural network, which takes the log of the above-surface remote-sensing reflectance ($R_{rs}$) of eight of the fifteen MERIS bands (i.e. after atmospheric correction, Bands 1-7 and Band 9) as well as three angles (solar zenith, viewing zenith, azimuth difference) as input and provides the log of the following three optical coefficients as output: pigment absorption ($a_{ph}(442)$), absorption of gelbstoff and bleached suspended matter ($a_{dg}(442)$), and scattering coefficient of all particles ($b_p(442)$), all at 442 nm (MERIS Band 2). The optical coefficients are then used to compute the concentrations of chlorophyll-a and total suspended matter dry weight. These are, together with the gelbstoff absorption, the three Case 2 water products of MERIS.

The neural network is trained with simulated $R_{rs}$ spectra. About 30000 spectra are used to cover a large range from Case 1 and Case 2 waters as well as different observation and solar angles (see Table 6.1). The simulation of $R_{rs}(\lambda)$ is performed using Hydrolight radiative transfer model. The model is set up in the following way:

- No bottom reflection
- Homogenous vertical distribution of water constituents
- No inelastic scattering
- Waves according to 3 m/s wind

Standard clear atmosphere with oceanic aerosol and different solar zenith angles ($0 – 80^o$ from zenith) was used to simulate incoming solar light. The detector captures the directional water leaving radiance and downwelling irradiance just above the surface for computing the directional $R_{rs}$. For the comparison here only the nadir $R_{rs}$ was used. The part controlling the success of the simulation and training of the aNN is the bio-optical model. For the MERIS aNN algorithm, it is based on measurements of the IOPs, i.e. absorption and scattering. These data are mainly from European waters, dominated by measurements in the North Sea.

The bio-optical models used represent mean conditions and variabilities (see Table 6.1). For each case of the simulations, the optical properties are varied randomly according to the standard deviations of the measured absorption and scattering spectra. For the absorption of gelbstoff ($a_g$) and bleached particles ($a_d$) as well as for the total particle scattering ($b_p$), the wavelength exponent is varied according to the measured standard deviations; while for the absorption spectra of phytoplankton pigment ($a_{ph}(\lambda)$) one out of 223 different measured spectra is selected randomly for each simulation. The absorption and scattering coefficients at 442 nm are randomly selected from the log scale from the range (see Table 6.1), while the viewing and sun angles are selected randomly from the linear scale. The simulated spectra are furthermore randomly degraded by using an estimated error of the instrument and the atmospheric correction. $R_{rs}$ spectrum that is out of the training range is detected using a forward neural network. This network takes the optical coefficients from the first backward network as input to compute $R_{rs}$ spectrum.

This spectrum is then compared with the measured one. If the $Chi^2$ deviations of all eight bands are above a certain level [*Doerffer and Schiller*, 2000], the spectrum is classified as out of the training range. However, this test was not used for the IOCCG data sets.

Uncertainties in atmospheric correction over water with low water leaving radiance sometimes result in negative reflectance. The neural network easily allows excluding these incorrect values by introducing a cut-off. In the MERIS aNN algorithm this cut-off was set to an $R_{rs}$ value of 0.000955 $sr^{-1}$. All reflectance with value below this threshold are clipped to this value. The neural network is trained in the same way.

### 6.3 aNN Results with the IOCCG Data Sets

The aNN algorithm we have tested here has 5 hidden layers with 45, 16, 12, 8 and 5 neurons respectively. It is the algorithm which is presently used for reprocessing all MERIS data [*Doerffer and Schiller*, 2006]. $a_{ph}(442)$, $a_{dg}(442)$ and $b_{bp}(442)$ (which is assumed as 1.5% of $b_p(442)$) were retrieved by applying this algorithm to the IOCCG data sets. Note that, due to wavelength mismatch, the aNN algorithm (designed specifically for MERIS) was not applied to the *in situ* part of the IOCCG data sets. Before applying the aNN algorithm, the reflectance spectra for the MERIS bands were linearly interpolated from the data set, which has a 10 nm spacing. Also the optical properties of the test data set were interpolated for 442 nm. It is necessary to point out that the IOCCG synthetic data set, though simulated with Hydrolight radiative transfer code also, has been computed totally independent of the data used for training the aNN. There are no relationships between the two data sets.

Figure 6.1 compares the derived properties (for data of $30^o$ solar zenith angle) with their corresponding known values, while Table 6.2 summarizes results from statistical analysis. For the entire range of total absorption and backscattering coefficients the RMSE values are 0.052 and 0.082 (see Table 6.2), respectively, with slope values nearly 1.0. Similar results were also obtained for the synthetic data set with the Sun at $60^o$ from zenith (not shown here). These results indicate that the aNN algorithm accurately retrieved those optical properties that determine the remote sensing reflectance. When the total absorption is decomposed into the components of water, gelbstoff and phytoplankton pigment, the scatter is much larger (RMSE values are 0.230 and 0.271 for $a_{dg}(442)$ and $a_{ph}(442)$, respectively) and the relationships deviate from linearity in the middle concentration range. The scatter is obvious due to the fact that the bio-optical models used for the IOCCG synthetic data set are different from those used for training the aNN. This is presumably also true for the maximum in difference at the middle of the data range. Here the separation between absorption by dissolved organic matter and phytoplankton pigments is most critical. Since this is also normally the case in nature, it indicates that total absorption and total backscattering are more robust variables, which should be derived from reflectance spectra in addition to other IOPs or concentrations of different water constituents.

Table 6.1. Variability and range of the optical properties used for the simulation of water leaving radiance reflectance spectra that were used to train the aNN.

| Component / property | value range |
|---|---|
| Gelbstoff absorption wavelength exponent [$nm^{-1}$] | 0.014 ± 0.002 |
| Bleached particle absorption wavelength exponent [$nm^{-1}$] | 0.008 ± 0.005 |
| Particle scattering wavelength exponent | 0.4 ± 0.2 |
| White particle scattering wavelength exponent | 0.0 |
| Phytoplankton pigment absorption spectra | random selection from > 200 absorption spectra, normalized at 442 nm (MERIS Band 2) |
| Gelbstoff absorption ($a_g$) at 442 nm [$m^{-1}$] | 0.005 - 5.0 |
| Particle scattering ($b_p$) at 442 nm [$m^{-1}$] | 0.005 - 30.0 |
| White particle scattering ($b_{pw}$) at 442 nm [$m^{-1}$] | 0.005 - 30.0 |
| Phytoplankton pigment absorption ($a_{ph}$) at 442 nm [$m^{-1}$] | 0.001 - 2.0 |
| Minimum particle scattering at 442 nm [$m^{-1}$] | 0.25 $a_{ph}(442)$ |
| Bleached particle absorption | 0.1 $b_p(442)$ + $\delta^*$0.03 $b_p(442)$ |
| Sun zenith angle [degree] | 0 - 80 |
| Viewing zenith angle [degree] | 0 - 50 |
| Difference between sun and viewing azimuth angle [degree] | 0 - 180 |

*δ is a random value in the range of 0-1.

Table 6.2. RMSE and regression (Type II) results for the synthetic data set (30° solar zenith angle). IOPs were retrieved with $R_{rs}$ values at 412, 442, 490, 510, 560, 617, 665 and 708 nm. N is the number of data tested, while n is the number of valid retrieval.

| | N | n | Intercept | slope | $R^2$ | RMSE | bias |
|---|---|---|---|---|---|---|---|
| $a_{dg}(442)$ | 500 | 500 | -0.210 | 0.959 | 0.959 | 0.230 | -0.174 |
| $a_{ph}(442)$ | 500 | 500 | 0.407 | 1.163 | 0.943 | 0.271 | 0.202 |
| $a(442)$ | 500 | 500 | -0.009 | 1.006 | 0.994 | 0.052 | -0.013 |
| $b_{bp}(442)$ | 500 | 500 | -0.038 | 0.993 | 0.980 | 0.082 | -0.024 |

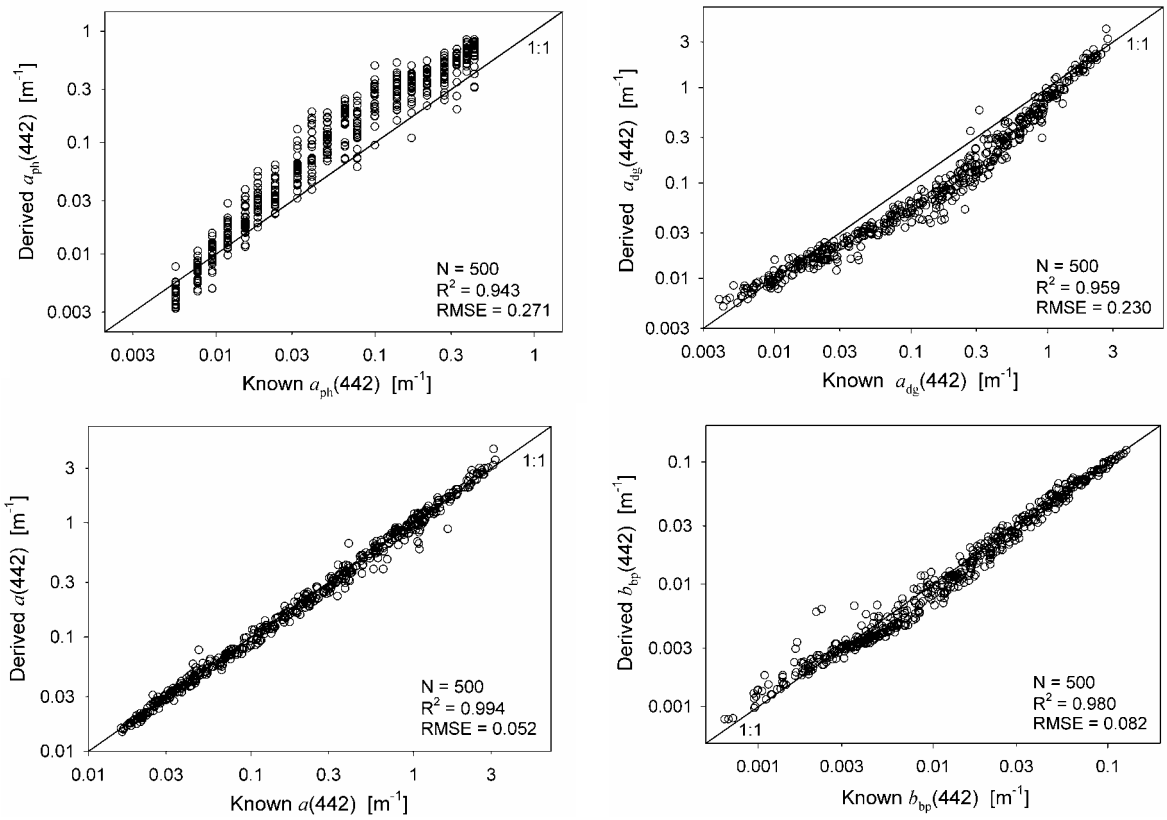


Figure 6.1 Comparison between aNN derived IOPs and the known IOPs, for the IOCCG synthetic data set (the Sun at 30$^o$ from zenith). aNN used $R_{rs}$ values at 412, 442, 490, 510, 560, 617, 665 and 708 nm to retrieve the IOPs.

## Chapter 7. The Linear Matrix Inversion Algorithm

Paul Lyon and Frank Hoge

### 7.1 Background

The Linear Matrix Inversion algorithm was developed by Hoge and Lyon [1996]. This algorithm uses remote-sensing reflectance at three wavelengths to simultaneously derive three major unknowns algebraically. Due to its linear matrix nature, it is efficient in processing satellite images. In the past decade, this algorithm has been applied to data taken from many regions around the world [*Hoge and Lyon*, 1996; *Hoge and Lyon*, 1999; *Hoge et al.*, 2001]. Never the less, since some of the parameters used in the algorithm were developed based on measurements made mainly from the Mid Atlantic Bight and off the East Coast of the United States, further refinement and improvement is expected in the coming years.

### 7.2 Inputs of LMI

The algorithm uses remotely sensed reflectance, $R_{rs}$, propagated through the air/water interface, into semi-analytic reflectance model developed by Gordon et al. [1988]. The present version of the algorithm that is optimized for use with satellite data uses only three inputs, $R_{rs}(412)$, $R_{rs}(490)$ and $R_{rs}(555)$. The algorithm also has four empirical parameters, described below, that determine the spectral shapes of the individual IOP spectrum.

### 7.3 Basic Assumptions of LMI

There are three assumptions that are fundamental to this inversion technique. First, it is assumed that the semi-analytic equation, shown in Eq. 7.1 below, is a good description of the relationship between the IOPs and the reflectance over a wide range of environments. Second, it is assumed that globally the optically significant varying IOPs are, absorption coefficients of phytoplankton and CDOM (including detritus), and backscattering coefficient of all particles (scattering constituents other than water). Thus, an algorithm based on properly formulated spectral models of these three principal IOPs may be applied to many different water masses. And, third, it is assumed that, using a proper combination of wavelengths, the three major IOPs can be resolved if the following conditions are met. The wavelengths used should maximize the mathematical differences between the spectral shapes of the three IOPs. And, within each IOP, a stable spectral dependence must be maintained or the modulations of the IOP spectral shapes need to be empirically adjusted to reflect their natural variability.

### 7.4 Approach

7.4.1 Algorithm mathematical description

As stated above, the algorithm is based on the reflectance model developed by Gordon et al. [1988],

$$r_{rs} = g_1\left(\frac{b_b}{b_b + a}\right) + g_2\left(\frac{b_b}{b_b + a}\right)^2 . \tag{7.1}$$

Here $r_{rs}$ is the subsurface remote-sensing reflectance, which can be easily calculated from the remote-sensing reflectance ($R_{rs}$) provided by any sensor. $g_1 = 0.0949$ and $g_2 = 0.0794$ are model parameters for $r_{rs}$ [*Gordon et al.*, 1988]. $b_b$ and $a$ are the total backscattering coefficients and total absorption coefficient, respectively. Defining $u$ as

$$u \equiv \frac{b_b}{b_b + a}, \tag{7.2}$$

we get a quadratic equation with $u$ as the variable,

$$g_2 u^2 + g_1 u - r_{rs} = 0, \tag{7.3}$$

which can easily be solved for $u$ using the quadratic formula. Since $b_b$ is a sum of $b_{bw}$ and $b_{bp}$, $a$ is a sum of $a_w$, $a_{ph}$, and $a_{dg}$, and $a_w$ and $b_{bw}$ are known constants, a linear system with $a_{ph}$, $a_{dg}$ and $b_{bp}$ as variables can then be constructed by re-arranging $u$ [*Hoge and Lyon*, 1996]:

$$a_{ph}(\lambda)+a_{dg}(\lambda)+b_{bp}(\lambda)v(\lambda)=-a_w(\lambda)-b_{bw}(\lambda)v(\lambda), \tag{7.4}$$

with

$$v \equiv 1-\frac{1}{u}. \tag{7.5}$$

For an exact solution, three different wavelengths are used to form a system of three equations with three unknowns. After spectrally modeling the three IOP variables with values at a reference wavelength ($\lambda_r$ = 410 nm) the equation becomes,

$$a^{\diamond}_{ph}(\lambda)a_{ph}(\lambda_r)+a^{\diamond}_{dg}(\lambda)a_{dg}(\lambda_r)+b^{\diamond}_{bp}(\lambda)b_{bp}(\lambda_r)v(\lambda)=-a_w(\lambda)-b_{bw}(\lambda)v(\lambda). \tag{7.6}$$

Here $a^{\diamond}_{ph}(\lambda)$, $a^{\diamond}_{dg}(\lambda)$ and $b^{\diamond}_{bp}(\lambda)$ represent the normalized optical properties at $\lambda_r$ (see 7.4.2). Eq. 7.6 can now be used to construct the linear matrix that could be inverted to derive the IOPs consistent with the input $R_{rs}$ and the spectral models,

$$\begin{bmatrix} 1 & 1 & v(\lambda_r) \\ a^{\diamond}_{ph}(\lambda_2) & a^{\diamond}_{dg}(\lambda_2) & b^{\diamond}_{bp}(\lambda_2)v(\lambda_2) \\ a^{\diamond}_{ph}(\lambda_3) & a^{\diamond}_{dg}(\lambda_3) & b^{\diamond}_{bp}(\lambda_3)v(\lambda_3) \end{bmatrix} \begin{bmatrix} a_{ph}(\lambda_r) \\ a_{dg}(\lambda_r) \\ b_{bp}(\lambda_r) \end{bmatrix} = -\begin{bmatrix} a_w(\lambda_r)+b_{bw}(\lambda_r)v(\lambda_r) \\ a_w(\lambda_2)+b_{bw}(\lambda_2)v(\lambda_2) \\ a_w(\lambda_3)+b_{bw}(\lambda_3)v(\lambda_3) \end{bmatrix}. \tag{7.7}$$

Note that the inverse matrix must be computed for each data point since input data, $R_{rs}(\lambda)$, is on both sides of the equation (contained in $v(\lambda)$). Any standard method of solving this system of equations can be used. The Hoge/Lyon inversion algorithm uses lower/upper deconvolution [*Hoge and Lyon*, 1999].

7.4.2 IOP spectral models

To mathematically solve Eq. 7.7, spectral models are required for the three IOP variables. It is important to select wavelengths where each IOP tends to co-vary among wavelengths [*Hoge and Lyon*, 1996]. Based on many different published phytoplankton absorption spectra, phytoplankton absorption coefficients at 412, 490 and 555 nm are found to co-vary well. A Gaussian function centered at 443 nm, with a half-max-full-width (HMFW) of 70 nm ($\sigma$ in Eq. 7.8 below) is used to model $a_{ph}(\lambda)$. No improvement in the retrieved IOPs was found when the HMFW parameter $\sigma$ was empirically varied.

$$a_{ph}(\lambda)=a_{ph}(\lambda_r)e^{\left[\frac{\lambda_r^2+886(\lambda-\lambda_r)-\lambda^2}{2\sigma^2}\right]}. \tag{7.8}$$

The combined absorption coefficient of detritus and gelbstoff, $a_{dg}(\lambda)$, is modeled with an exponential decay function [*Bricaud et al.*, 1981; *Carder et al.*, 1991; *Roesler et al.*, 1989]:

$$a_{dg}(\lambda)=a_{dg}(\lambda_r)e^{-S(\lambda-\lambda_r)}. \tag{7.9}$$

$S$ is the spectral slope and is set to 0.018 ($nm^{-1}$) for all inversions discussed within this chapter.

The total particulate backscattering coefficient, $b_{bp}(\lambda)$ is modeled as a power-law function of wavelength,

$$b_{bp}(\lambda)=b_{bp}(\lambda_r)\left(\frac{\lambda_r}{\lambda}\right)^{Y}, \tag{7.10}$$

with exponent $Y$ empirically estimated as follow,

$$Y=m_1\frac{R_{rs}(490)}{R_{rs}(555)}+m_2. \tag{7.11}$$

Sensitivity studies have found that the magnitude of parameter $Y$ affects the $b_{bp}$ and the $a_{dg}$ retrievals more than the $a_{ph}$ retrievals [*Hoge and Lyon*, 1996]. The empirical parameters, $m_1$ (0.8) and $m_2$ (0.2) have

been optimized for use with global satellite data, such that errors in the derived IOPs caused by this equation are minimized in a global sense. These parameters can also have regional values to achieve better regional results.

## 7.5 Results

### 7.5.1 Synthetic data set

Figure 7.1 shows the agreement between known and derived IOPs. There is a logarithmic offset in the $a_{ph}(410)$ retrievals and several outliers, yet the agreement is evident as shown in Table 7.1 by the correlation of determination ($R^2$) of 0.877 and the slope close to 1.0, and an RMSE of 0.222 (n = 484). Note that the statistics presented in Table 7.1 are affected by the outliers that lie below the one-to-one line, so that the larger population above the line could still be corrected by using an offset in log space. This infers, of course, that regional or specific tuning of this and any algorithm may improve its performance for similar settings.

The agreement between input and output $a_{dg}(410)$ is better than that of $a_{ph}(410)$, with correlation of determination as 0.958 and slope about 1.1, and RMSE of 0.16 (Table 7.1). Much better results are achieved for the total absorption and particle backscattering coefficients, with both $R^2$ and slope values close to 1.0 and RMSE of 0.14 and 0.15, respectively.

The smaller number (n) in the statistics analysis (Table 7.1 and Table 7.2) represents all the data points that the inversion successfully processed (all IOPs with values greater than zero, or where the output $a(410) < 10.0$ m$^{-1}$). Data points with negative IOP retrievals were excluded from the statistics and the figures, as they are physically unrealistic values that are filtered out automatically. In normal operation of the linear matrix inversion, retrievals where $a_{dg}(410) > 1.0$ m$^{-1}$ or $a_{ph}(410) > 1.0$ m$^{-1}$ are considered suspect. To allow readers to compare the results of this algorithm with those of other techniques discussed in this report, however, inversions with $a(410)$ with values up to 10.0 m$^{-1}$ are included in the figures and tables.

### 7.5.2 *In situ* data set

For the *in situ* data set, the regression statistics are provided in Table 7.2. Figure 7.2 compares retrieved $a_{ph}(412)$, $a_{dg}(412)$, $a(412)$ and $a(490)$ with their measured values, respectively. There were no *in situ* $b_{bp}$ data for comparison.

Apparently the retrievals of $a_{ph}$ and $a_{dg}$ scattered much more than that of the simulated data set. This might be due to the measurement uncertainties that are common in field-measured data. Also, large portions of the data were taken in coastal waters, and real *in situ* properties may not follow the limited combinations of spectral shapes used in the simulated data set.

Again, better results are obtained for the total absorption coefficients. This suggests that it is easier to retrieve the total absorption using this technique than it is to resolve the separate components of the total absorption.

## 7.6 Discussion

### 7.6.1 Overall results of the linear matrix inversion algorithm

As described above, the retrievals of the total absorption are quite good for both *in situ* and simulated data sets. The separation of the absorption into contributions from phytoplankton and dissolved organic matter are less accurate, but still retrieved well. The spectral model parameters used in the linear inversion of both simulated and *in situ* data sets preformed well in spite of the fact that the true spectral shapes at the wavelengths used in the inversions varied over dramatic ranges, as shown in Fig. 7.1. These results demonstrate that an exact solution derived from a 3-by-3 inversion, can be optimized to retrieve IOPs at a reference wavelength. The linear inversion method has both weaknesses and strengths associated with its use, which are briefly described below.

### 7.6.2 Algorithm weaknesses

One set of weakness in this algorithm is related to the parameterization of the IOP spectral shapes. For example, the empirical adjusted $b_{bp}$ spectral model and the fixed spectral models for $a_{ph}$ and $a_{dg}$ will not properly represent all combinations of water constituents, especially when contributions from optically significant constituents not well described by the three IOP basis vectors are present. The fixed spectral shape of $a_{ph}$ limits the accuracy of IOP retrievals since true phytoplankton absorption spectra vary dramatically (e.g., Hoepffner and Sathyendranath [1991]). Also, the $a_{dg}$ spectral slope coefficient, $S$, should be varied with type of water mass.

As shown in Figures 7.1 and 7.2, the algorithm has been optimized to retrieve values at 412nm. The IOPs derived at 412 nm can be translated to any other wavelength through the IOP spectral models but the accuracy of the values derived at the other wavelengths will be driven by how well the spectral models reflect the true characteristics of the in water constituents. Methods developed by Wang et al. [2005] should be implemented to help describe the range of equally valid retrievals of IOPs. Also, there is no error checking for unreasonable inputs (such as negative $R_{rs}$) and for doubtful retrievals (e.g., very large IOPs).

The need for the 412 nm band to separate the CDOM absorption from the phytoplankton absorption exposes the algorithm to potentially large errors in input $R_{rs}(412)$, caused by the fact that in coastal region accurate atmospheric correction at the shorter wavelengths is very difficult to achieve. This is a fundamental problem for all semi-analytical algorithms that attempt to use $R_{rs}(412)$ to separate phytoplankton and CDOM absorption coefficients.

### 7.6.4 Algorithm strengths

There are also several advantages gained by using the exact linear inversion approach. The most important feature is that the algorithm limits errors in IOP spectral models by using wavelengths where each IOP tends to co-vary. Hyperspectral data was tested and it was found that the best agreement between the retrieved IOPs and truth data was achieved by using the fewest number of wavelengths possible. Therefore, the SeaWiFS bands, 412, 490 and 555 nm, or the closest to those bands on other sensors, are used in this algorithm. By using this simplified approach, we sacrifice deriving information about more constituents in the water but minimize the errors caused by poor spectral models to describe highly variable portions of the IOP spectra.

The inversion is computationally fast and no iteration is needed. Large data set processing is limited more by the rate of data to be read and written to disk, than by the computation of the IOP outputs.

Inputs from several different satellites that are contemporaneous and geographically coincident can be used in the inversion to produce a multi satellite blended product. In this case, the same three wavelengths (or similar wave bands) are used from each satellite to realize the benefit of averaging out the asymmetrical errors in $R_{rs}$ in an over determined linear inversion, while still maintaining the inter-wavelength co-variance for each IOP.

With fewer spectral model parameters to adjust, the algorithm is easy to tune given known or expected values. This allows for tuning of the algorithm to specific regions where characteristics of constituent in the water are constrained temporally and spatially, so regionally optimized versions of the algorithm can be developed, without changing the core mathematical implementation.

Table 7.1: RMSE and regression (Type II) results of the synthetic data set ($\theta_0 = 30°$). IOPs were retrieved with $R_{rs}$ values at 410, 490 and 550 nm as inputs. N is the number of data tested, while n is the number of valid retrieval.

| | N | n | intercept | slope | $R^2$ | RMSE | bias |
|---|---|---|---|---|---|---|---|
| $a_{ph}(410)$ | 500 | 484 | 0.053 | 0.989 | 0.877 | 0.222 | 0.068 |
| $a_{ph}(490)$ | 500 | 484 | 0.114 | 0.997 | 0.891 | 0.23 | 0.118 |
| $a_{dg}(410)$ | 500 | 484 | 0.069 | 1.052 | 0.958 | 0.161 | 0.03 |
| $a_{dg}(490)$ | 500 | 484 | -0.032 | 1.051 | 0.921 | 0.236 | -0.095 |
| $a(410)$ | 500 | 484 | 0.067 | 1.036 | 0.964 | 0.14 | 0.045 |
| $a(490)$ | 500 | 484 | 0.012 | 1.007 | 0.942 | 0.133 | 0.005 |
| $b_{bp}(410)$ | 500 | 484 | 0.043 | 1.019 | 0.922 | 0.15 | 0.007 |
| $b_{bp}(490)$ | 500 | 484 | 0.008 | 1.018 | 0.936 | 0.149 | -0.027 |

Table 7.2: RMSE and regression (Type II) results of the *in situ* data set. IOPs were retrieved with $R_{rs}$ values at 412, 490 and 555 nm as inputs. N is the number of data tested, while n is the number of valid retrieval.

| | N | n | intercept | slope | $R^2$ | RMSE | bias |
|---|---|---|---|---|---|---|---|
| $a_{ph}(412)$ | 656 | 642 | 0.336 | 1.208 | 0.654 | 0.332 | 0.02 |
| $a_{ph}(490)$ | 656 | 642 | 0.454 | 1.231 | 0.686 | 0.325 | 0.078 |
| $a_{dg}(412)$ | 656 | 642 | -0.142 | 1.007 | 0.653 | 0.325 | -0.149 |
| $a_{dg}(490)$ | 656 | 642 | -0.315 | 0.98 | 0.599 | 0.427 | -0.284 |
| $a(412)$ | 656 | 642 | -0.082 | 0.96 | 0.872 | 0.163 | -0.045 |
| $a(490)$ | 656 | 642 | -0.035 | 0.994 | 0.804 | 0.168 | -0.028 |

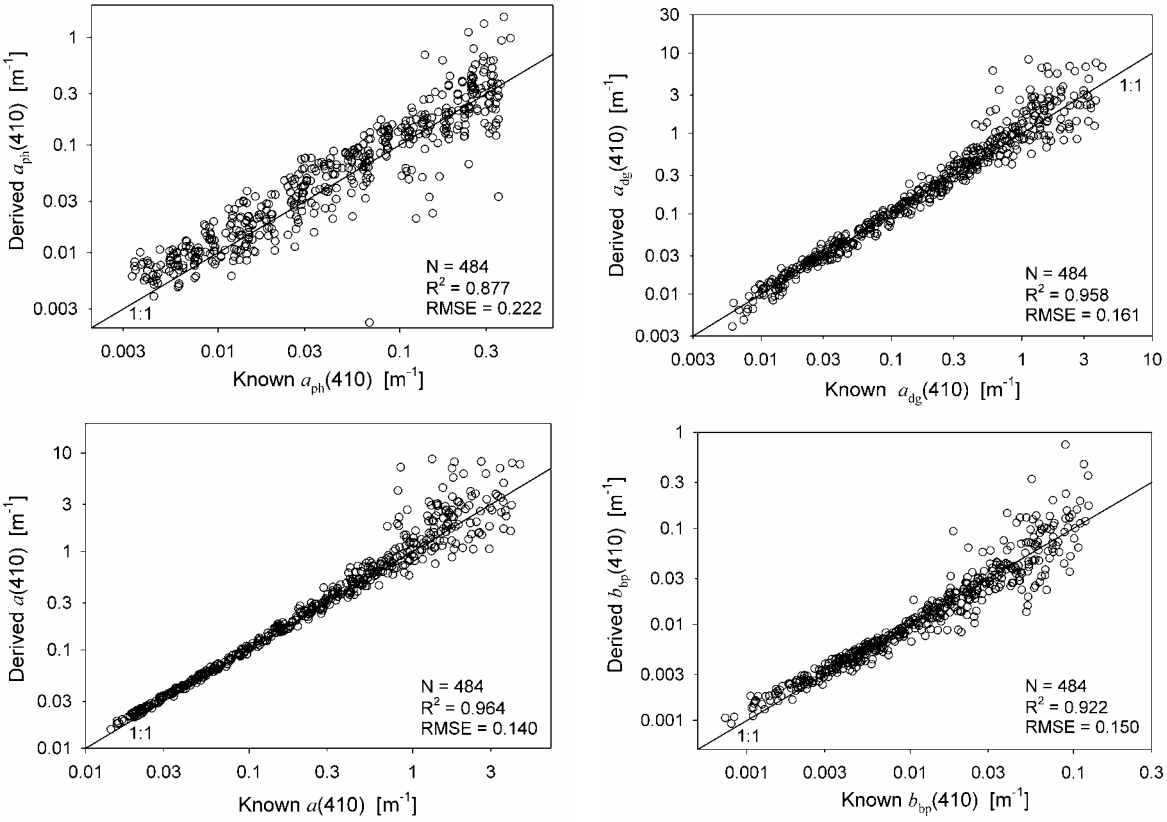


Figure 7.1. Comparison between retrieved and simulated IOPs for a sun zenith angle of 30°. IOPs were retrieved using $R_{rs}$ values at 410, 490 and 550 nm.

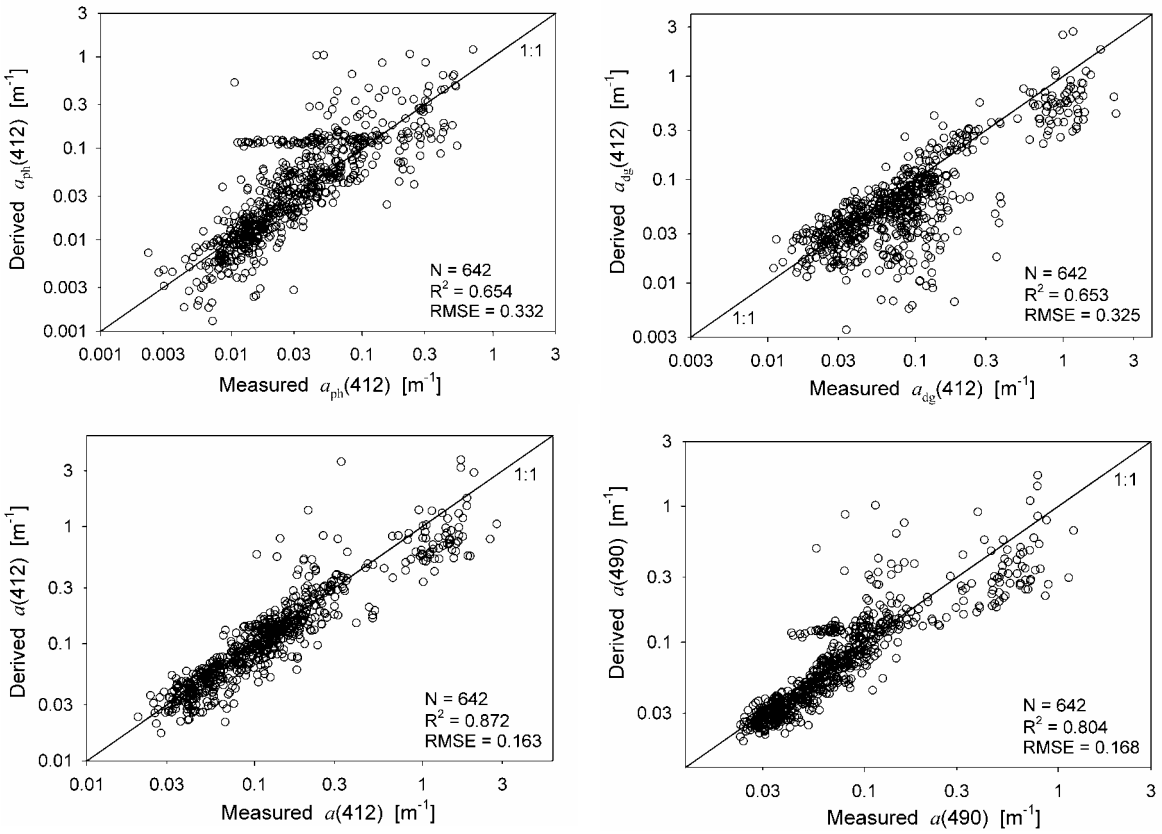


Figure 7.2. Comparison between retrieved and *in situ* IOPs. IOPs were retrieved using $R_{rs}$ values at 410, 490 and 555 nm.

## Chapter 8. Over Constrained Linear Matrix Inversion with Statistical Selection

Emmanuel Boss and Collin Roesler

### 8.1 General Description

Semi-analytic inversions of remotely sensed reflectance have been available since 1995 [*Roesler and Perry*, 1995]. However, a procedure that provides an uncertainty of the inverted parameter for each individual spectrum based on uncertainties in the remote sensing data and the model has only recently been devised [*Wang et al.*, 2005].

We use the same model philosophy as in Wang et al. [2005] with a slight modification (we use a single phytoplankton absorption spectrum). We assume a known relationship between $r_{rs}$ and the absorption and backscattering coefficients [*Gordon et al.*, 1988]:

$$r_{rs}(\lambda) = \frac{L_u(\lambda,0^-)}{E_d(\lambda,0^-)} = 0.0949\frac{b_b(\lambda)}{a(\lambda)+b_b(\lambda)} + 0.0794\left(\frac{b_b(\lambda)}{a(\lambda)+b_b(\lambda)}\right)^2. \quad (8.1)$$

The quadratic form is important for high $r_{rs}(\lambda)$ values [*Garver and Siegel*, 1997]. Gordon et al. [1988] estimated that the model errors in Eq. 8.1 are less than 10%.

The total absorption coefficient is partitioned as follows:

$$a(\lambda) = a_w(\lambda) + a_{ph}(\lambda) + a_{dg}(\lambda), \quad (8.2)$$

where the subscripts w, ph, and dg designate sea water, phytoplankton, and the combined contribution of CDOM and detrital material. The spectral absorption coefficient $a_w(\lambda)$ for sea water is computed for given salinity and temperature based on Pope and Fry [1997] and Pegau et al. [1997].

The spectral absorption coefficient of phytoplankton is assumed to be:

$$a_{ph}(\lambda) = a_{ph}(\lambda_0)\, a^+_{ph}(\lambda), \quad (8.3)$$

where $a^+_{ph}(\lambda)$ is an average of normalized phytoplankton absorption spectra [*Roesler and Perry*, 1995] and $\lambda_0$ is commonly set as 440 nm.

The spectral absorption coefficient of the combined absorption by CDOM and detritus is:

$$a_{dg}(\lambda) = a_{dg}(\lambda_0)\exp(-S(\lambda-\lambda_0)), \quad (8.4)$$

where $S$ is the spectral slope of the combined absorption coefficient. This function has been found to be an adequate representation of measured CDOM and detritus absorption coefficient with $S$ ranging between 0.008 to 0.023 $nm^{-1}$ (e.g., Roesler et al. [1989]).

The total backscattering coefficient, $b_b(\lambda)$, is approximated by

$$b_b(\lambda) = b_{bw}(\lambda) + b_{bp}(\lambda). \quad (8.5)$$

The spectral backscattering coefficients of sea water ($b_{bw}(\lambda)$) are computed for a given salinity based on the interpolation of the data of Morel [1974] as in Boss and Pegau [2001].

The spectral particle backscattering coefficient is assumed to obey:

$$b_{bp}(\lambda) = b_{bp}(\lambda_0)\,(\lambda/\lambda_0)^{-Y}. \quad (8.6)$$

This formulation is consistent with many previous studies, though without in-water validation.

To account for variability in space and time of the spectral shapes of the IOPs we perform the $r_{rs}$ inversion allowing the shape parameters (spectral slope $S$ and spectral slope $Y$) to vary within most of their observed range of variability ($0.01 \le S \le 0.02$, $0 \le Y \le 2$). For each parameter we use 11 different values with equal intervals between their maximum and minimum, resulting in $11^2 = 121$ different inversion computations for each $r_{rs}$.

It can be shown that with known spectral shapes, Eq. 8.1 can be solved to obtain $b_{bp}(\lambda_0)$, $a_{dg}(\lambda_0)$, and $a_{ph}(\lambda_0)$ using a linear matrix inversion technique [*Hoge and Lyon*, 1996]. When the number of wavelength exceeds the number of unknowns (3 in our case), this solution is the best solution in a least-square sense [*Press*, 1992].

From all the solutions to Eq. 8.1 we select the solution for which $a_{dg}(440)$ and $a_{ph}(440) > -0.005$ $m^{-1}$ and $b_{bp}(440) > -0.0001$ $m^{-1}$ (slightly negative values are accepted to compensate for finite uncertainties in

measurements and calibrations). We further restrict ourselves to the solutions whose reconstructed $r_{rs}$ (calculated by substituting the solutions into Eq. 8.1) obeys:

$$|r_{rs,reconstucted}(\lambda) - r_{rs,known}(\lambda)|/r_{rs,known}(\lambda) < 0.1 \text{ or } 0.2 \text{ for every } \lambda.$$

These criteria can result in cases where no solution could be found for a given $r_{rs}$. The choice of the criteria should be driven by knowledge of uncertainties in observed $r_{rs}$ as well as the assumed spectral shapes (in particular that of phytoplankton).

We thus present the results from the two different solution selection criteria in the tables, but only the criteria of 0.1 in the plots. We provide uncertainties for the solutions on the plots based on the distance between the 84$^{th}$ and 16$^{th}$ percentile of the obtained solutions (~+/- one standard deviation for a normal distribution).

Given the application to remote sensing we used only the $R_{rs}$ values at 410, 440, 490, 510 and 550 nm (or nearby for the *in situ* data set).

### 8.2 Results and Discussion with IOCCG Data Sets

Simulated data set: Over the large dynamic range of the data set the inversion fairs rather well for both 10 and 20% criteria (Fig. 8.1, Tables 8.1 & 8.2). Not surprisingly the stringent criteria provide less but better solutions (in terms of RMSE error and bias). The agreement between derived and known IOPs can be further improved by choosing other wavelengths (e.g., 410 nm for $a_{dg}$ and 550 nm for $b_{bp}$) and by adding more wavelengths (as we have demonstrated in Wang et al. [2005], for example, adding a 670 nm channel, the successful retrieval increased from 408 to 472 with the 10% criteria). It is encouraging that the uncertainty estimates for both $a_{dg}(440)$ and $b_{bp}(440)$ intersect the 1:1 line suggesting the constraint criteria is working well.

*In situ* data set: Large uncertainties in inverted parameters (in particular $a_{ph}$) suggest that some of these data have many possible solutions and thus large uncertainties for a given $R_{rs}(\lambda)$. Some data points are way off the line, possibly due to large sun angles and/or poor measurements.

In Wang et al. [2005] we used a more complicated phytoplankton absorption formulation which increased the computation by a factor larger than 10. We found that this complexity did not improve the match ups significantly and thus decided here to use a single phytoplankton absorption function.

It can easily be demonstrated that a different choice of wavelengths for inversions or a different choice of wavelength for the parameter can significantly improve/degrade the retrieval. Thus, if we are after $a_{dg}$, inverting a near UV wavelength provides the best inversion; while for $b_b$, it is in the NIR that the inversion does best; as long as adequate $R_{rs}$ at those wavelengths could be available.

### 8.3 Summary

The inversion method presented here was designed to provide uncertainty estimates of inversion products and is dependent on the reality of the assumptions of the model. For example, it is well known that Eq. 8.6 is likely not a good representation of particulate spectral backscattering, yet it is the only simple model currently available. Much work is still needed to understand spectral IOPs, and such work will, without a doubt, improve our ability to retrieve in-water parameters from remote sensing.

Table 8.1. RMSE and regression (Type II) results for the synthesized data set. Statistics of comparison of median of all possible inversion solution with a 10% agreement criterion. $R_{rs}$ values at 410, 440, 490, 510

and 550 nm were used as inputs for IOP retrieval. N is the number of data tested, while n is the number of valid retrieval.

| | N | n | intercept | slope | $R^2$ | RMSE | bias |
|---|---|---|---|---|---|---|---|
| $a$(440) | 500 | 408 | -0.001 | 0.995 | 0.966 | 0.106 | 0.003 |
| $b_{bp}$(440) | 500 | 408 | -0.055 | 0.972 | 0.935 | 0.125 | 0.003 |
| $a_{dg}$(440) | 500 | 408 | -0.021 | 0.982 | 0.956 | 0.141 | -0.001 |
| $a_{ph}$(440) | 500 | 408 | 0.160 | 1.113 | 0.927 | 0.159 | -0.002 |

Table 8.2. RMSE and regression (Type II) results for the synthesized data set. Statistics of comparison of median of all possible inversion solution with a 20% agreement criterion. $R_{rs}$ values at 410, 440, 490, 510 and 550 nm were used as inputs for IOP retrieval. N is the number of data tested, while n is the number of valid retrieval.

| | N | n | intercept | slope | $R^2$ | RMSE | bias |
|---|---|---|---|---|---|---|---|
| $a$(440) | 500 | 438 | -0.074 | 0.938 | 0.946 | 0.145 | -0.025 |
| $a_{ph}$(440) | 500 | 438 | -0.025 | 1.014 | 0.878 | 0.201 | -0.044 |
| $a_{dg}$(440) | 500 | 438 | -0.082 | 0.942 | 0.944 | 0.169 | -0.023 |
| $b_{bp}$(440) | 500 | 438 | -0.186 | 0.925 | 0.898 | 0.168 | -0.034 |

Table 8.3. RMSE and regression (Type II) results for the *in situ* data set. Statistics of comparison of median of all possible inversion solution with a 10% agreement criterion. $R_{rs}$ values at 412, 443, 490, 510 and 555 nm were used as inputs for IOP retrieval. N is the number of data tested, while n is the number of valid retrieval.

| | N | n | intercept | slope | $R^2$ | RMSE | bias |
|---|---|---|---|---|---|---|---|
| $a$(412) | 656 | 504 | -0.022 | 0.942 | 0.872 | 0.146 | 0.029 |
| $a$(443) | 656 | 504 | -0.029 | 0.969 | 0.849 | 0.150 | 0.001 |
| $a_{dg}$(443) | 656 | 504 | -0.018 | 1.043 | 0.705 | 0.259 | -0.072 |
| $a_{ph}$(443) | 656 | 504 | 0.068 | 1.031 | 0.613 | 0.285 | 0.024 |

Table 8.4. RMSE and regression (Type II) results for the *in situ* data set. Statistics of comparison of median of all possible inversion solution with a 20% agreement criterion. $R_{rs}$ values at 412, 443, 490, 510 and 555 nm were used as inputs for IOP retrieval. N is the number of data tested, while n is the number of valid retrieval.

| | N | n | intercept | slope | $R^2$ | RMSE | bias |
|---|---|---|---|---|---|---|---|
| $a$(412) | 656 | 629 | -0.036 | 0.939 | 0.867 | 0.157 | 0.019 |
| $a$(443) | 656 | 629 | -0.039 | 0.977 | 0.842 | 0.165 | -0.017 |
| $a_{dg}$(443) | 656 | 629 | 0.086 | 1.069 | 0.63 | 0.298 | -0.013 |
| $a_{ph}$(443) | 656 | 629 | -0.057 | 1.014 | 0.714 | 0.266 | -0.075 |

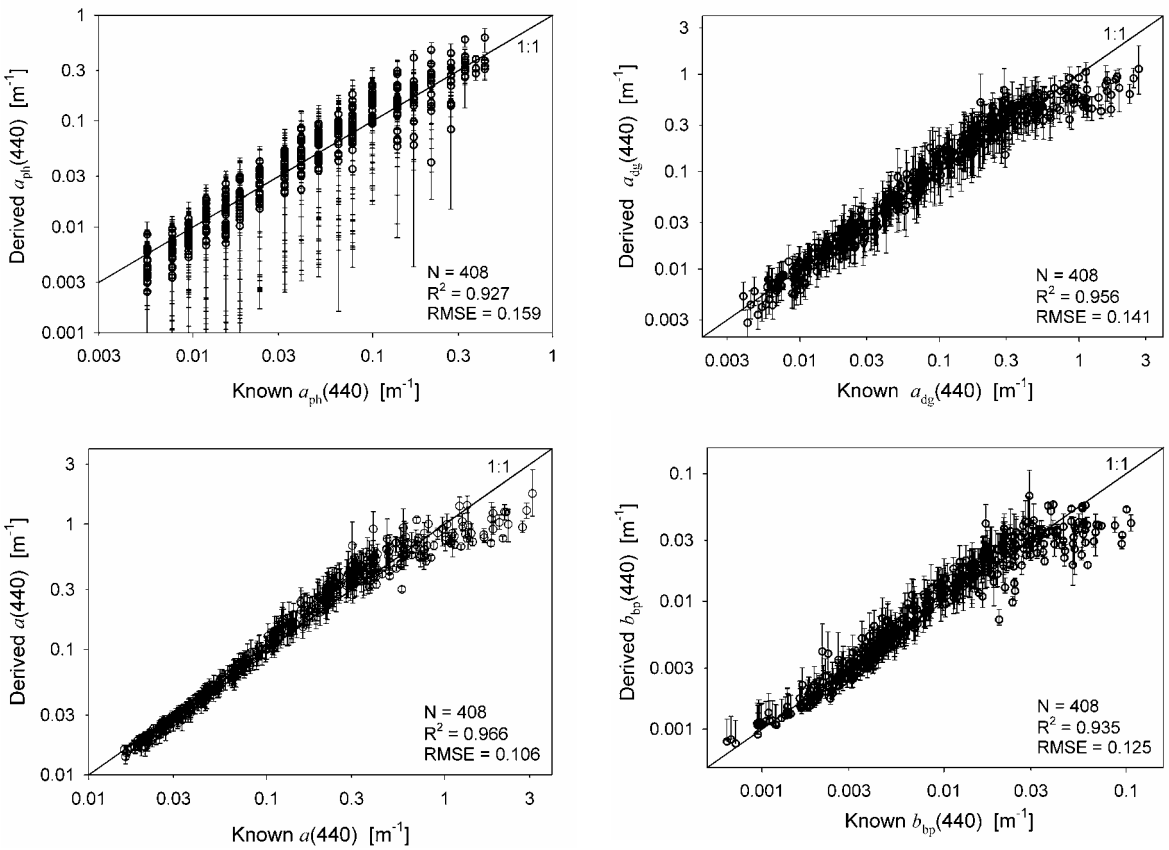


Figure 8.1. Comparison of inverted and the simulated data set (30 degrees sun angle) for $a_{ph}(440)$, $a_{dg}(440)$, $a(440)$, and $b_{bp}(440)$ for the 10% criteria (stats in Table 8.1). Vertical lines denote the 90% confidence intervals in the solutions. $R_{rs}$ values at 410, 440, 490, 510 and 550 nm were used as inputs for IOP retrieval.

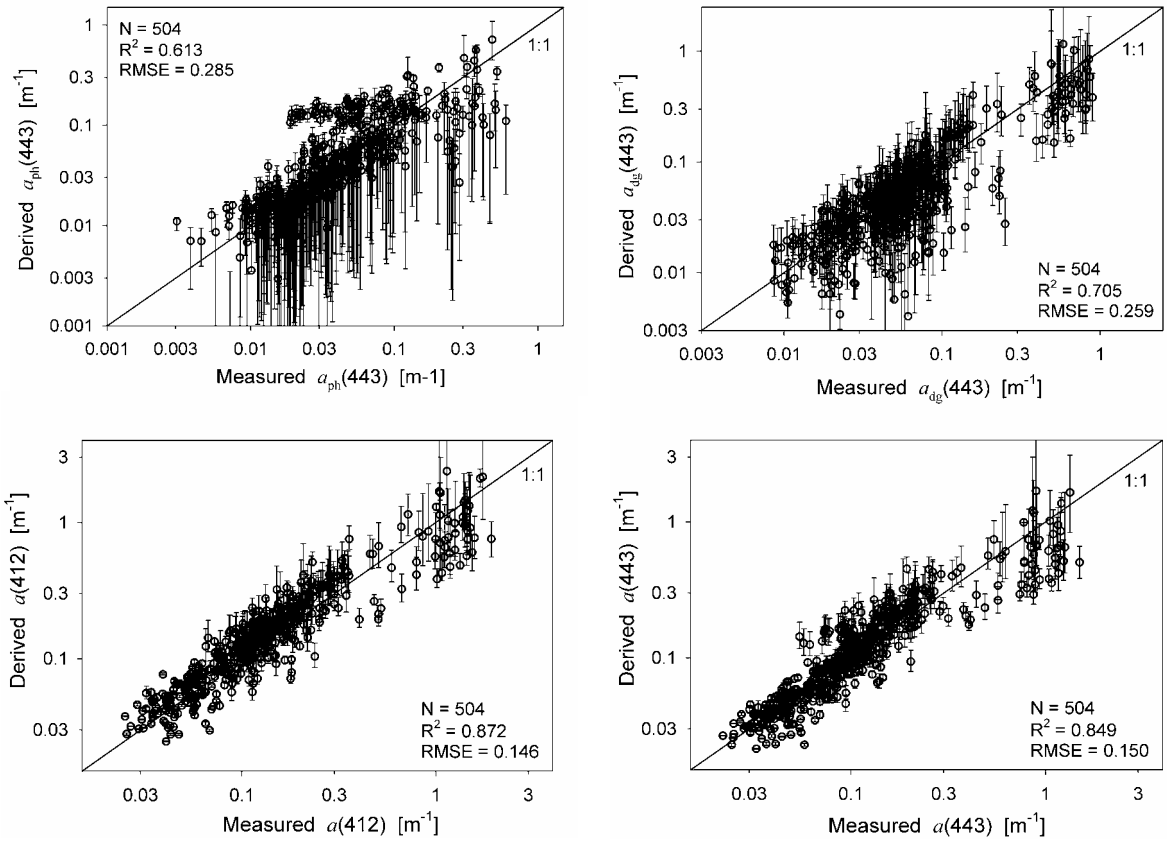


Figure 8.2. As Fig.8.1, for the *in situ* data set.

## Chapter 9. MODIS Semi-Analytic Algorithm for IOP

Kendall L. Carder, Jennifer P. Cannizzaro, Robert F. Chen, ZhongPing Lee

### 9.1 Introduction

The Moderate-Resolution Imaging Spectrometer (MODIS) semi-analytic algorithm (Carder_MODIS here after) [*Carder et al.*, 2004; *Carder et al.*, 1999] derives chlorophyll-a concentrations and inherent optical properties ($a_{ph}(\lambda)$, $a_{dg}(\lambda)$ and $b_{bp}(\lambda)$) from remote-sensing reflectance spectrum ($R_{rs}(\lambda)$). This algorithm is composed with an algebraic portion and an empirical portion. The algebraic portion is for waters with low absorption (mostly oceanic waters) while the empirical portion is for waters with high absorption (mostly coastal waters). The main characters of this algorithm include that it responds to the large global variability observed in 1) chlorophyll-specific absorption coefficients ($a^*_{ph}(\lambda)$), and 2) gelbstoff-to-phytoplankton absorption ratios. This algorithm utilizes differences between measured sea-surface temperatures and known nitrate-depletion temperatures (NDT) [*Kamykowski*, 1987; *Kamykowski and Zentara*, 1986] to select the most appropriate $a^*_{ph}(\lambda)$ for a given bio-optical domain. The algorithm was first developed and evaluated using high-light, tropical/subtropical and summer temperate field data [*Carder et al.*, 1999] and later expanded to include parameters appropriate for low-light, polar data [*Carder et al.*, 2004].

### 9.2 Algorithm Description

9.2.1 Remote-sensing reflectance model

By making several approximations, the $R_{rs}(\lambda)$ used in Carder_MODIS algorithm is simplified to [*Carder et al.*, 1999]

$$R_{rs}(\lambda) \approx constant \frac{b_b(\lambda)}{a(\lambda)}, \tag{9.1}$$

where the "constant" is unchanging with respect to wavelength and solar zenith angle. The value of the constant is not relevant to the algorithm since, as will be shown later, the algorithm (for absorption and chlorophyll-a concentration) uses spectral ratios of $R_{rs}(\lambda)$ and the constant term factors out.

Further, both $b_b(\lambda)$ and $a(\lambda)$ are partitioned into several separate terms. Each term is described empirically and is written in a general fashion as a function of variables and empirically derived parameters. Since sea surface temperatures were not provided in the IOCCG data sets, the unpackaged parameters regarding $a^*_{ph}(\lambda)$ derived from high-light, tropical/subtropical and summer temperate waters were employed [*Carder et al.*, 1999] (see Table 9.1). While $a^*_{ph}(\lambda)$ is extremely important for deriving chlorophyll-a concentrations accurately, retrievals of $a_{ph}(\lambda)$ and $a_{dg}(\lambda)$ are less sensitive to differences in $a^*_{ph}(\lambda)$.

9.2.2 Backscattering coefficients

The total backscattering coefficient, $b_b(\lambda)$, can be expanded as

$$b_b(\lambda) = b_{bw}(\lambda) + b_{bp}(\lambda), \tag{9.2}$$

with, $b_{bp}(\lambda)$ modeled as [*Carder et al.*, 1999]

$$b_{bp}(\lambda) = X\left(\frac{551}{\lambda}\right)^Y. \tag{9.3}$$

$b_{bw}(\lambda)$ is constant [*Morel*, 1974]. $X$ is the particulate backscattering at 551nm, and $Y$ describes the spectral shape of the particle backscattering spectrum. Values for $X$ and $Y$ were determined empirically by model inversion [*Carder et al.*, 1999] and are described as

$$X = X_0 + X_1 R_{rs}(551), \tag{9.4}$$

$$Y = Y_0 + Y_1 \frac{R_{rs}(443)}{R_{rs}(488)}, \tag{9.5}$$

where $X_{0,1}$ and $Y_{0,1}$ are empirically derived constants [*Carder et al.*, 1999] and are provided in Table 9.1.

When absorption due to water molecules does not dominate the total absorption coefficient at 551 nm, algorithms that utilize wavelengths longer than 551 nm that take advantage of the larger inflection in the pure water absorption spectra between 570-610 nm [*Pope and Fry*, 1997] are required. Using measurements of $R_{rs}(\lambda)$ and $b_{bp}(\lambda)$ collected from the West Florida Shelf (WFS), the equation

$$b_{bp}(551) = 10^{(0.933 - 0.134\log(R_{rs}(551)) + 1.029\log(R_{rs}(667)))} - 0.000966, \quad (9.6)$$

(n = 154, $R^2$ = 0.96, RMSE = 0.160) was derived for MODIS-like wavelengths. This function was used when Carder_MODIS algorithm was applied to the IOCCG synthetic data set. Since remote-sensing data with wavelengths longer than 555 nm were not available for the IOCCG *in situ* data set, however, $b_{bp}(551)$ values were then estimated using Eq. 9.4.

9.2.3 Absorption coefficients

The total absorption coefficient, $a(\lambda)$, can be expanded as

$$a(\lambda) = a_w(\lambda) + a_{ph}(\lambda) + a_{dg}(\lambda), \quad (9.7)$$

with value of $a_w(\lambda)$ taken from Pope and Fry [1997].

The shape of the $a_{ph}(\lambda)$ spectrum for a given water mass changes due to the pigment-package effect and changes in pigment composition. For the MODIS wavebands centered at 412, 443, 488, and 551 nm, a hyperbolic tangent function was chosen to empirically model the ratio of $a_{ph}(\lambda)/a_{ph}(675)$ in order to ensure that this ratio approaches an asymptote at very high or very low values of $a_{ph}(675)$ [*Carder et al.*, 1999],

$$a_{ph}(\lambda) = a_0(\lambda)\exp\left(a_1(\lambda)\tanh\left(a_2(\lambda)\ln\left(a_{ph}(675)/a_3(\lambda)\right)\right)\right)a_{ph}(675), \quad (9.8)$$

with values of $a_{0\text{-}3}(\lambda)$ provided in Table 9.1.

The cumulative effects of detritus and gelbstoff absorption, $a_{dg}(\lambda)$, are expressed as

$$a_{dg}(\lambda) = a_{dg}(400)\exp(-S(\lambda - 400)), \quad (9.9)$$

where $S$ is the spectral slope, and a value of 0.0225 $nm^{-1}$ provided optimal retrieval results for the Carder_MODIS algorithm to calculate chlorophyll-a concentrations [*Carder et al.*, 1999]. It is larger than the mean ocean value of about 0.015 $nm^{-1}$, likely compensating in part for uncertainties in other parts of the model.

9.2.4 Model inversion

Via Eqs. 9.1 - 9.9, $R_{rs}(\lambda)$ is reduced to a function of three unknowns ("constant" term, $a_{ph}(675)$, and $a_{dg}(400)$) along with model constants for $X_{0,1}$, $Y_{0,1}$, $a_{0\text{-}3}(\lambda)$, and $S$ (Table 9.1). To algebraically solve for the values of the two desired unknowns ($a_{ph}(675)$ and $a_{dg}(400)$), spectral ratios of 412:443 and 443:551 for $R_{rs}(\lambda)$ as shown

$$\frac{R_{rs}(412)}{R_{rs}(443)} = \frac{b_b(412)}{b_b(443)}\frac{a(443)}{a(412)},$$
$$\frac{R_{rs}(443)}{R_{rs}(551)} = \frac{b_b(443)}{b_b(551)}\frac{a(551)}{a(443)}, \quad (9.10)$$

provided the best separation of the two absorption contributions. Details on the computational method of solving these equations are discussed in Carder et al. [1999].

9.2.5 Empirical portion of Carder_MODIS

For waters with high concentrations of gelbstoff and chlorophyll, $R_{rs}(412)$ and $R_{rs}(443)$ values are small, and therefore the above semi-analytical approach cannot perform properly due to low signal-to-noise ratios. Thus the semi-analytic approach is designed to return values only when modeled $a_{ph}(675)$ values are less than 0.025 $m^{-1}$, which is equivalent to a chlorophyll concentration of about 1.5 $mg/m^3$. Otherwise, the following empirical algorithms derived from the West Florida Shelf (1999-2001) and Bayboro Harbor (St. Petersburg, Fla.) field data (n = 319) are used.

For $a_{ph}(443)$, there is

$$a_{ph}(443)_{emp} = 10^{\left(-1.164-1.2095\rho_{35}-1.566\rho_{35}^{2}-1.708\rho_{45}+19.502\rho_{45}^{2}\right)}, \quad (9.11)$$

where $\rho_{ij}$ is the log-transformed ratio of $R_{rs}(\lambda_i)$ to $R_{rs}(\lambda_j)$ and the subscripts i and j are wavebands #1-6 that represent MODIS wavebands 412, 443, 488, 531, 551, and 667 nm, respectively. Since this equation requires the MODIS $R_{rs}(531)$ waveband and the SeaWiFS waveband $R_{rs}(510)$ was provided instead with the IOCCG *in situ* data, a modified SeaWiFS algorithm was also developed

$$a_{ph}(443)_{emp} = 10^{\left(-1.189-1.133\rho_{35}-2.151\rho_{35}^{2}-0.775\rho_{45S}+7.592\rho_{45S}^{2}\right)}, \quad (9.12)$$

and applied to the IOCCG *in situ* data set. Here $\rho_{45S}$ is equal to $\log(R_{rs}(510)/R_{rs}(555))$.

The empirical algorithm for $a_{dg}(443)$ is

$$a_{dg}(443)_{emp} = 10^{\left(-1.144-0.738\rho_{15}-1.386\rho_{15}^{2}-0.644\rho_{25}+2.451\rho_{25}^{2}\right)}, \quad (9.13)$$

and was applied to the IOCCG *in situ* data set. Since adding a $\rho_{65}$ term reduced the RMSE error by 40% for calculating $a_{dg}(443)$ for the WFS and Bayboro Harbor data, the derived equation

$$a_{dg}(443)_{emp} = 10^{\left(0.043-0.185\rho_{25}-1.081\rho_{35}+1.234\rho_{65}\right)}, \quad (9.14)$$

was applied to the synthetic data set where $R_{rs}(670)$ data (considered equal to $R_{rs}(667)$) were available.

Empirical retrievals of $a(\lambda)$ at 412, 443, and 488 nm also improved for the WFS and Bayboro Harbor data set when a red reflectance waveband was included. Thus, the empirical expression derived from field data and applied to the synthetic data set takes the form

$$a(\lambda)_{emp} = 10^{\left(c_0(\lambda)+c_1(\lambda)\log\left(R_{rs}(443)\right)+c_2(\lambda)\log\left(R_{rs}(488)\right)+c_3(\lambda)\log\left(R_{rs}(667)\right)\right)}, \quad (9.15)$$

where $c_{0\text{-}3}(\lambda)$ are empirically derived parameters (Table 9.2a). Note that while reflectance ratios are used to calculate $a_{ph}(443)_{emp}$ and $a_{dg}(443)_{emp}$, reflectance values are used to calculate $a(\lambda)_{emp}$ in Eq. 9.15. For the IOCCG *in situ* data set that does not have a red reflectance waveband, an empirical expression similar to that of Lee et al. [1998b]

$$a(\lambda)_{emp} = 10^{\left(t_0(\lambda)+t_1(\lambda)\rho_{25}+t_2(\lambda)\rho_{25}^{2}+t_3(\lambda)\rho_{35}+t_4(\lambda)\rho_{35}^{2}\right)}, \quad (9.16)$$

was developed with $t_{0\text{-}4}(\lambda)$ (Table 9.2b) also derived from the WFS and Bayboro Harbor data.

9.2.6 Blending semi-analytic and empirical IOP values

In order to provide a smooth transition in modeled IOP values when the algorithm switches from the semi-analytical to the empirical method, a weighted average of the modeled values returned by both algorithms is used near the transition border [*Carder et al.*, 1999]. When the semi-analytical portion returns an $a_{ph}(675)$ value between 0.015 and 0.025 $m^{-1}$, IOP values are calculated as

$$IOP = w(IOP)_{sa} + (1-w)(IOP)_{emp}, \quad (9.17)$$

where $(IOP)_{sa}$ is the semi-analytically-derived value, $(IOP)_{emp}$ is the empirically derived value, and w is the weighting factor equal to $[0.025\text{-}a_{ph}(675)]/0.010$. Semi-analytical and empirical IOP values are used when modeled $a_{ph}(675)$ values are less than 0.015 $m^{-1}$ and greater than 0.025 $m^{-1}$, respectively. Note that this transition range can vary with pigment packaging (e.g., see Carder et al. [2004]).

## 9.3 Algorithm Performance with the IOCCG Data Sets

The Carder_MODIS algorithm requires $R_{rs}(\lambda)$ data at a minimum of five wavebands: 412, 443, 488, 531 and 551 nm. Further inclusion of the $R_{rs}(667)$ improves retrievals of $a_{dg}(443)_{emp}$ (Eq. 9.14) and $a(\lambda)_{emp}$ (Eq. 9.15) values. Since the synthetic $R_{rs}(\lambda)$ data was generated in 10 nm increments from 400-800 nm, reflectance values at 410, 440, 490, 530, 550 and 670 nm were considered similar enough to the MODIS wavebands and were input into the algorithm. For the IOCCG *in situ* data set only $R_{rs}(\lambda)$ data at 412, 443, 490, 510, and 555 nm were input into the equations.

9.3.1 Synthetic data set

Using the Carder_MODIS algorithm, the inherent optical properties $a(410)$, $a(440)$, $a(490)$, $a_{ph}(440)$, $a_{dg}(440)$ and $b_{bp}(550)$ were derived from the synthetic $R_{rs}(\lambda)$ data (Figure 9.1). Statistical analyses were performed on log-transformed data and include the slope, intercept, correlation of determination ($R^2$) and the root-mean-square error (RMSE) (Table 9.3a).

Particulate backscattering coefficients at 550 nm retrieved using Eq. 9.6 from $R_{rs}(550)$ and $R_{rs}(670)$ are very accurate (RMSE = 4.2%). Total absorption coefficients at 410, 440 and 490 nm were also retrieved accurately for the synthetic data set with RMSE errors equal to 7.1, 5.9 and 6.5%, respectively. RMSE values for $a_{ph}(440)$ (14.1%) and $a_{dg}(440)$ (13.5%) are slightly more than double the error calculated for $a(440)$ since phytoplankton and detritus/gelbstoff exhibit overlapping absorption spectra making it difficult to separate them.

9.3.2 *In situ* data set

The results of the Carder_MODIS algorithm when applied to the IOCCG *in situ* data set were not as good as the results observed for the synthetic data set because errors in field $R_{rs}$ and IOP data, not present in the synthetic data, are significant in the *in situ* data.

Total absorption coefficients at 412, 443, and 488 nm derived from the *in situ* $R_{rs}(\lambda)$ yielded RMSE errors of 19.7, 20.5 and 20.6%, respectively (Figure 9.2, Table 9.3b). Errors for $a_{ph}(443)$ and $a_{dg}(443)$ were only slightly higher than $a(443)$ and were 19.5% and 27.9%, respectively. While the semi-analytic $a_{ph}(443)$ values derived from synthetic $R_{rs}(\lambda)$ data were overestimated, values derived from the *in situ* $R_{rs}(\lambda)$ data were more centered about the one-to-one line. This may indicate that perhaps the underlying $a_{ph}(\lambda)$ functions used to generate the synthetic data for oligotrophic waters are not quite representative of the distribution of the naturally occurring $a_{ph}(\lambda)$ data, or at least Eq. 9.8 is more consistent with the $a_{ph}(\lambda)$ functionality of the *in situ* data set than with that of the synthetic data set.

Large errors that occur in empirically derived $a(412)$, $a(443)$, and $a_{ph}(443)$ values and appear as linear horizontal rows of data in Figure 9.2 at ~0.23, 0.15, and 0.07 $m^{-1}$, respectively, can be traced to a single investigator for a large multi-year, coastal data set. Removal of these points would improve the performance of the empirical portion of our algorithm. Furthermore, empirical retrievals of $a(\lambda)$ and $a_{dg}(440)$ may also be improved for this data set if $R_{rs}(\lambda)$ data were available for wavelengths longer than 555 nm.

## 9.4 Conclusions

The Carder_MODIS algorithm [Carder et al., 1999] calculated $b_{bp}(550)$ and $a(\lambda)$ values very accurately for the synthetic data set. Values for $a_{ph}(443)$ and $a_{dg}(443)$ were calculated less accurately because phytoplankton and detritus/gelbstoff exhibit overlapping absorption making it more difficult to separate them using $R_{rs}(\lambda)$. Retrieval errors tripled for $a(\lambda)$ and doubled for $a_{dg}(443)$ when the algorithm was applied to the *in situ* data set as compared to the synthetic data set. The fact that the partitioned values fell within the same error range as the total-absorption values suggests that much of the error imputed to the algorithms for the *in situ* data set may be attributable to errors or inconsistencies among the measured data sets, whereas the synthetic data set had no measurement noise.

IOP retrieval errors calculated for the *in situ* data set may improve if $R_{rs}(667)$ data were available. Significant error reductions were observed for empirically derived backscattering and total absorption coefficients when red reflectance data were used for our high-absorption Florida data set and for the synthetic data set. Note, however, that while $R_{rs}(667)$ can be used for "perfect" synthetic data, accurate measurements of $R_{rs}(667)$ from space are much more subject to error due to smaller signal-to-noise ratios. A waveband near 610-620 nm would perhaps be a better compromise than use of 667 nm for satellites. The Medium Resolution Imaging Spectrometer (MERIS) has such a waveband around 620 nm.

Finally, the expansion of available global data sets in the past 10 years and the broad range of data synthesized in the numerical data set have provided examples of how various older algorithms may be improved, and we are grateful for being included in this challenging algorithm inter-comparison.

**Table 9.1.** Parameters for the MODIS semi-analytical algorithm for regions without packaged pigments.

| $\lambda$ | $a_0$ | $a_1$ | $a_2$ | $a_3$ | $X_0$ | $X_1$ | $Y_0$ | $Y_1$ | $S$ ($nm^{-1}$) |
|---|---|---|---|---|---|---|---|---|---|
| 412 | 2.20 | 0.75 | -0.5 | 0.0112 | -0.00182 | 2.058 | -1.13 | 2.57 | 0.0225 |
| 443 | 3.59 | 0.80 | | | | | | | |
| 488 | 2.27 | 0.59 | | | | | | | |
| 551 | 0.42 | -0.22 | | | | | | | |

**Table 9.2a.** Wavelength-dependent parameters for the high-absorption empirical $a(\lambda)$ algorithm (Eq. 9.15) that requires $R_{rs}(670)$.

| | $c_0(\lambda)$ | $c_1(\lambda)$ | $c_2(\lambda)$ | $c_3(\lambda)$ |
|---|---|---|---|---|
| $a$(412) | -0.349 | -1.041 | 0.171 | 0.754 |
| $a$(443) | -0.166 | 0.068 | -1.284 | 1.077 |
| $a$(488) | -0.167 | 0.478 | -1.639 | 1.075 |

**Table 9.2b.** Wavelength-dependent parameters for the high-absorption empirical $a(\lambda)$ algorithm (Eq. 9.16) that does not require $R_{rs}(670)$.

| | $t_0(\lambda)$ | $t_1(\lambda)$ | $t_2(\lambda)$ | $t_3(\lambda)$ | $t_4(\lambda)$ |
|---|---|---|---|---|---|
| $a$(412) | -0.640 | -0.718 | -0.650 | -1.365 | 2.369 |
| $a$(443) | -0.837 | -0.860 | -0.791 | -1.162 | 2.855 |
| $a$(488) | -0.947 | -0.343 | -0.721 | -1.633 | 2.741 |

**Table 9.3a.** RMSE and regression (Type II) results of the synthetic data set ($\theta_0 = 30°$). $R_{rs}(\lambda)$ values at 410, 440, 490, 530, 550 and 670 nm were used as inputs. N is the number of data tested, while n is the number of valid retrieval.

| | N | n | intercept | slope | $R^2$ | RMSE | bias |
|---|---|---|---|---|---|---|---|
| $a$(410) | 500 | 500 | 0.015 | 0.990 | 0.990 | 0.071 | 0.020 |
| $a$(440) | 500 | 500 | 0.030 | 1.030 | 0.993 | 0.059 | 0.010 |
| $a$(490) | 500 | 500 | 0.079 | 1.082 | 0.993 | 0.065 | 0.008 |
| $b_{bp}$(550) | 500 | 500 | -0.012 | 0.998 | 0.995 | 0.042 | -0.008 |
| $a_{ph}$(440) | 500 | 500 | -0.046 | 0.908 | 0.963 | 0.141 | 0.071 |
| $a_{dg}$(440) | 500 | 500 | 0.084 | 1.098 | 0.978 | 0.135 | -0.004 |

**Table 9.3b**: RMSE and regression (Type II) results of the *in situ* data set. $R_{rs}(\lambda)$ values at 412, 443, 490, 510 and 555 were used as inputs. N is the number of data tested, while n is the number of valid retrieval.

| | N | n | intercept | slope | $R^2$ | RMSE | bias |
|---|---|---|---|---|---|---|---|
| $a$(412) | 656 | 656 | 0.098 | 1.066 | 0.826 | 0.197 | 0.039 |
| $a$(443) | 656 | 656 | 0.030 | 1.111 | 0.831 | 0.205 | -0.078 |
| $a$(488) | 656 | 656 | 0.131 | 1.173 | 0.789 | 0.206 | -0.063 |
| $a_{ph}$(443) | 656 | 656 | -0.052 | 0.986 | 0.827 | 0.195 | -0.032 |
| $a_{dg}$(443) | 656 | 656 | -0.041 | 1.082 | 0.771 | 0.279 | -0.144 |

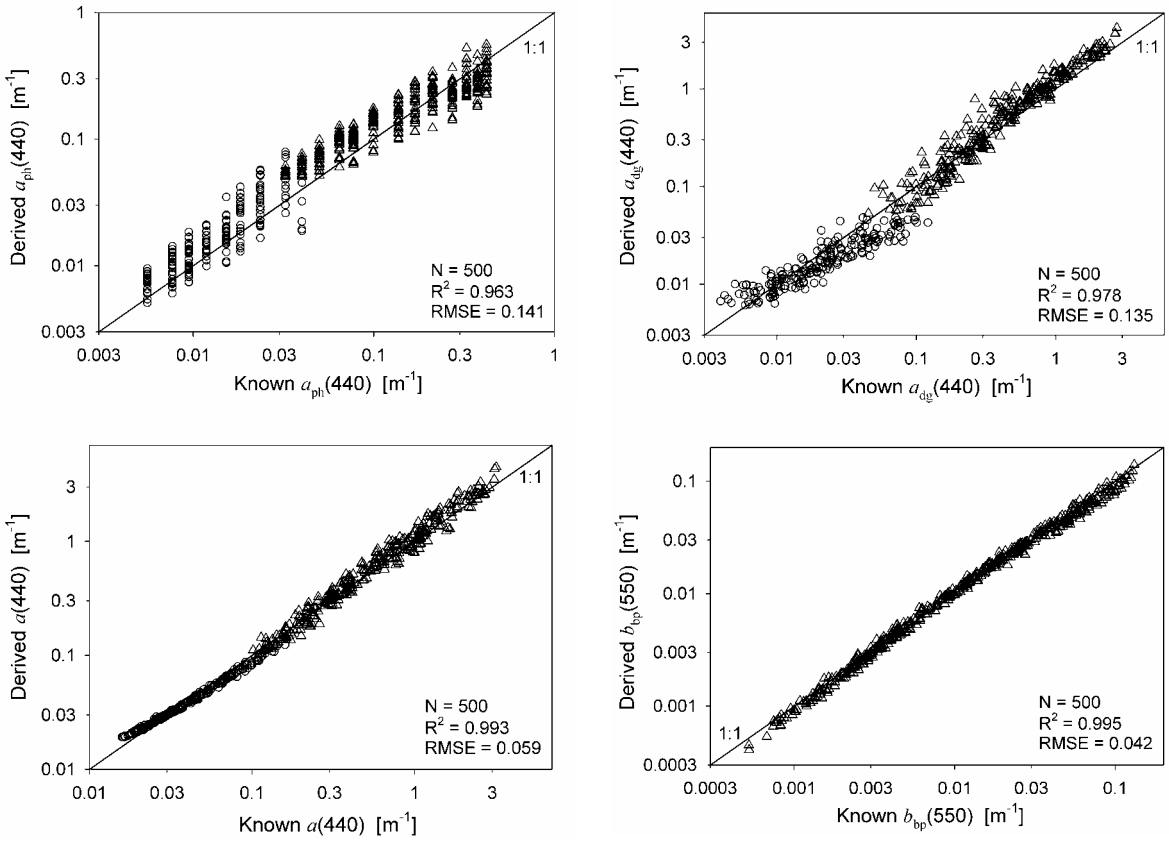


**Figure 9.1.** Relationships between known and retrieved IOPs using the Carder_MODIS algorithm (synthetic data set), with $R_{rs}(\lambda)$ at 410, 440, 490, 530, 550 and 670 nm used as inputs. Symbols: semi-analytic (o) and empirical (Δ).

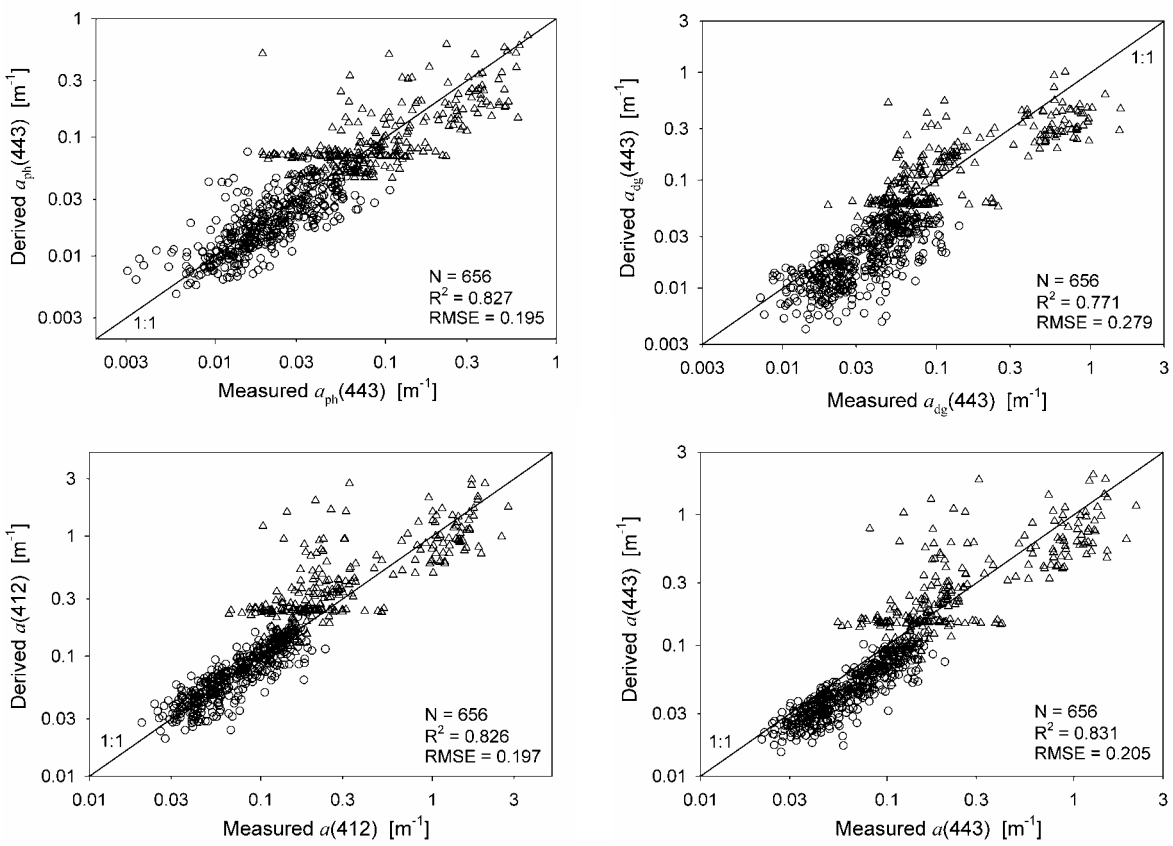


**Figure 9.2.** Relationships between measured and retrieved IOPs using the Carder_MODIS algorithm (*in situ* data set), with $R_{rs}(\lambda)$ at 412, 443, 490, 510 and 555 nm used as inputs. Symbols: semi-analytic (o) and empirical (Δ).

## Chapter 10. The Quasi-Analytical Algorithm

ZhongPing Lee, Kendall L. Carder, Robert Arnone

### 10.1 General Description

The Quasi-Analytical Algorithm (QAA) was developed by Lee et al. [2002] to derive inherent optical properties of optically deep waters. QAA separates the inversion process into two consecutive sections. The first section is the derivation of coefficients of total absorption and backscattering. In this section, there is no involvement of spectral models for the absorption coefficient of phytoplankton pigments and gelbstoff. The second section, which utilizes the derived total absorption coefficient from the first section, decomposes the total absorption coefficient into its major components.

### 10.2 Derive Total Absorption and Backscattering Coefficients

In this part, QAA follows the generally accepted relationship between remote-sensing reflectance and $b_b/(a+b_b)$, and the fact that water absorption coefficients dominate most of the longer wavelengths. Here $b_b$ is the total backscattering coefficient and $a$ is the total absorption coefficient. QAA starts with the calculation of $a$ at a reference wavelength ($\lambda_0$, 555 or 640 nm), with the assumption that remote-sensing reflectance at this wavelength is well measured from a remote-sensing platform.

The total absorption coefficient at $\lambda_0$ is expressed as

$$a(\lambda_0) = a_w(\lambda_0) + \Delta a(\lambda_0) . \quad (10.1)$$

$a_w(\lambda_0)$ is the contribution from water molecules [*Pope and Fry*, 1997], while $\Delta a(\lambda_0)$ represents the contribution from dissolved and suspended constituents. For this $a(\lambda_0)$, as long as $a_w(\lambda_0)$ makes a big portion (at least one third), errors in its estimation are limited.

Lee et al. [2002] proposed two $\lambda_0$ for dealing with IOP inversion: 555 nm for oceanic and most coastal waters and 640 nm for waters with high absorption coefficients ($a(440) > \sim 0.5$ m$^{-1}$). For each $\lambda_0$, there could be many ways to estimate $a(\lambda_0)$. In the exercise reported here, when 555 nm is selected as $\lambda_0$, $a(555)$ is estimated using the Morel-Maritorena approach [*Morel and Maritorena*, 2001] as described in Chapter 4. In essence, $a(555)$ is estimated with the value of $\max(R_{rs}(440,490,510))/R_{rs}(555)$. When 640 nm is selected as $\lambda_0$, $a(640)$ is estimated as in Lee et al. [2002], i.e.,

$$a(640) = 0.31 + 0.07\left(\frac{r_{rs}(640)}{r_{rs}(440)}\right)^{1.1} , \quad (10.2)$$

where $r_{rs}$ is the subsurface remote-sensing reflectance corresponding to the $R_{rs}$ measured above the surface.

To estimate $a(640)$ requires measurements of remote-sensing reflectance at 640 nm, a band which does not exist in many satellite sensors (such as SeaWiFS). To overcome this limitation, $R_{rs}(640)$ is simulated with measurements made at 490, 555 and 670 nm, as described in Lee et al. [2005b],

$$R_{rs}(640) = 0.01R_{rs}(555) + 1.4R_{rs}(670) - 0.0005R_{rs}(670)/R_{rs}(490) . \quad (10.3)$$

Note that in Lee et al. [2005b] it is $R_{rs}(667)$ for SeaWiFS spectral bands. This empirical formulae was aimed to more or less correct the chlorophyll-a fluorescence contained in $R_{rs}(670)$.

$r_{rs}(\lambda)$ is calculated from $R_{rs}(\lambda)$ through

$$r_{rs}(\lambda) = R_{rs}(\lambda)/(0.52 + 1.7\, R_{rs}(\lambda)), \quad (10.4)$$

where 0.52 and 1.7 are empirical values derived from data simulated by Hydrolight [*Lee et al.*, 1999]. Because $r_{rs}(\lambda)$ can be modeled as a polynomial function of $b_b/(a+b_b)$ [*Gordon et al.*, 1988; *Lee et al.*, 1998a], $b_b/(a+b_b)$ (represented as symbol $u$) at $\lambda$ can be calculated algebraically from $r_{rs}(\lambda)$ [*Hoge and Lyon*, 1996; *Lee et al.*, 2002],

$$u(\lambda) \equiv \frac{b_b(\lambda)}{a(\lambda)+b_b(\lambda)} = \frac{-0.0895+\sqrt{(0.0895)^2+4\times 0.1247\, r_{rs}(\lambda)}}{2\times 0.1247}. \tag{10.5}$$

The spectral $b_b(\lambda)$ is modeled with the widely used expression [*Gordon and Morel*, 1983; *Smith and Baker*, 1981],

$$b_b(\lambda) = b_{bw}(\lambda) + b_{bp}(\lambda_0)\left(\frac{\lambda_0}{\lambda}\right)^Y, \tag{10.6}$$

where $b_{bw}$ and $b_{bp}$ are the backscattering coefficients of pure seawater and suspended particles, respectively. Values of $b_{bw}(\lambda)$ are provided in *Morel* [1974].

When $a(\lambda_0)$, $u(\lambda_0)$, and $b_{bw}(\lambda_0)$ are known, $b_{bp}(\lambda_0)$ in Eq. 10.6 can be easily derived. The values of $b_b(\lambda)$ at other wavelengths are then calculated when the wavelength exponent ($Y$) is estimated from [*Lee et al.*, 2002]

$$Y = 2.2\left(1-1.2\,\exp\left(-0.9\frac{r_{rs}(440)}{r_{rs}(555)}\right)\right). \tag{10.7}$$

Finally, applying $b_b(\lambda)$ back to $u(\lambda)$ (derived from $r_{rs}(\lambda)$, Eq. 10.5), the total absorption coefficient at wavelength $\lambda$, $a(\lambda)$, is calculated algebraically,

$$a(\lambda) = \frac{\left(1-u(\lambda)\right)b_b(\lambda)}{u(\lambda)}. \tag{10.8}$$

To obtain smooth satellite IOP products where both 555 nm and 640 nm could be used as reference wavelength, the final $a(\lambda)$ product is a combination of the absorption coefficients derived using 555 nm as reference wavelength ($a(\lambda)^{[555]}$) and 640 nm as reference wavelength ($a(\lambda)^{[640]}$), in such a fashion

$$\begin{cases} a(\lambda) = a(\lambda)^{[555]}, & \text{for } a(440)^{[555]} < 0.3, \\ a(\lambda) = \left(1-\dfrac{a(440)^{[555]}-0.3}{0.2}\right)a(\lambda)^{[555]} + \left(\dfrac{a(440)^{[555]}-0.3}{0.2}\right)a(\lambda)^{[640]}, & \text{for } 0.3 \le a(440)^{[555]} \le 0.5, \\ a(\lambda) = a(\lambda)^{[640]}, & \text{for } a(440)^{[555]} > 0.5. \end{cases} \tag{10.9}$$

Further, final $b_{bp}(\lambda)$ is recalculated using $u(\lambda)$ and $a(\lambda)$ based on Eqs. 10.5 and 10.6.

### 10.3 Decompose the Total Absorption Coefficient

Decomposition of $a(\lambda)$ used the $a(410)$ and $a(440)$ values derived from the above steps. In the process, two more parameters are estimated first. One is the spectral ratio of $a_{ph}(410)/a_{ph}(440)$ (represented by symbol $\zeta$), while the other is the spectral ratio of $a_{dg}(410)/a_{dg}(440)$ (represented by symbol $\xi$). The value of $\zeta$ is estimated using the spectral ratio of $r_{rs}(440)/r_{rs}(555)$ based on the field data [*Lee et al.*, 1998b]:

$$\zeta = a_{ph}(410)/a_{ph}(440) = 0.71 + \frac{0.06}{0.8 + r_{rs}(440)/r_{rs}(555)}. \tag{10.10}$$

The value of $\xi$ is calculated after the spectral slope $S$ (used to describe the spectral shape of $a_{dg}(\lambda)$) is selected (0.015 $nm^{-1}$ is used in this exercise):

$$\xi = a_{dg}(410)/a_{dg}(440) = \exp(S\,(440\text{-}410)). \tag{10.11}$$

When the values of $a(410)$, $a(440)$, $\zeta$ and $\xi$ are known, $a_{ph}(440)$ and $a_{dg}(440)$ are calculated algebraically,

$$\begin{cases} a_{dg}(440) = \dfrac{\left(a(410)-\zeta\, a(440)\right)}{\xi-\zeta} - \dfrac{\left(a_w(410)-\zeta\, a_w(440)\right)}{\xi-\zeta}, \\ a_{ph}(440) = a(440) - a_{dg}(440) - a_w(440). \end{cases} \tag{10.12}$$

## 10.4 Results and Discussion

The above steps to retrieve IOPs from $R_{rs}(\lambda)$ are applied to the IOCCG data sets. For the synthetic data set, $R_{rs}$ values at 410, 440, 490, 510, 555, and 670 nm were used as indicated ($R_{rs}(555)$ is a simple average of $R_{rs}(550)$ and $R_{rs}(560)$). For the *in situ* data set, however, only $R_{rs}$ values at the first five wavelengths were used as $R_{rs}(670)$ is not available. The retrieved IOPs include $a(\lambda)$, $b_{bp}(\lambda)$, $a_{ph}(\lambda)$, and $a_{dg}(\lambda)$ of those wavelengths. To provide a general idea of the algorithm performance, some retrieved properties were compared with known values, with analysis results presented in Tables 10.1 and 10.2 and the figures followed. Performance (not presented) for the synthetic data with the Sun at 60$^o$ from zenith is similar as that with the Sun at 30$^o$.

For the synthetic data set, QAA retrieved total absorption and backscattering coefficients accurately (slope and $R^2$ values are near 1.0 and RMSE values are 5-6%) for the entire data range. The performance of the QAA to the *in situ* data set is not as good as that to synthetic data (see Fig. 10.2 and Table 10.2). This is not surprising since there are unavoidable errors and uncertainties (see Chapter 3) in the measurement of both $R_{rs}(\lambda)$ and IOPs. Also, natural water environment is far more complex than the ones simulated with computer code. Nevertheless, for such a inclusive data set, the RMSE values for $a(\lambda)$ are ~17%.

For both synthetic and *in situ* data sets, the retrieval of $a_{dg}(\lambda)$ is only slightly worse than the retrieval of total absorption coefficients, but more errors are found in the derived $a_{ph}(\lambda)$ (see Tables 10.1 and 10.2 and Figures 10.1 and 10.2). This is, in part, because gelbstoff (including detritus) likely contributes more to total absorption coefficient at 410 and/or 440 nm. Also, in the explicit decomposition of total $a(\lambda)$ to $a_{ph}(\lambda)$ and $a_{dg}(\lambda)$, values of $\zeta$ and $\xi$ are not exactly known but have to be estimated. Errors in these estimations will be propagated to the derived values of $a_{dg}(440)$ and $a_{ph}(440)$. Note that value of $\xi$ (directly related to the spectral slope of $a_{dg}(\lambda)$), as observed in the field and represented in the synthetic data set, may vary widely based on the nature of waters under study, such as humic versus fulvic acids [*Carder et al.*, 1989], and abundance of detritus [*Roesler et al.*, 1989], etc. Also, the present version of QAA uses only one spectral constraint regarding $a_{ph}(\lambda)$ (ratio of $a_{ph}(410)/a_{ph}(440)$) in the decomposition of $a(\lambda)$. Due to errors in $R_{rs}(\lambda)$ measurements as well as errors in selection of parameter $S$, negative $a_{ph}(440)$ or $a_{ph}(490)$ (4.2% in synthetic data and 4.0% in *in situ* data) appeared. Such retrievals were then flagged and removed in the statistical analyses. This kind of obvious errors can be remedied by adding more spectral constraints (e.g., the spectral models of $a^*_{ph}(\lambda)$ used in other algorithms) in the derivation of $a_{ph}(\lambda)$ (model uncertainties will be introduced, however), or replaced with empirical estimates [*Lee et al.*, 1998b].

When $R_{rs}(640)$ was not used in the derivation process (i.e. 555 nm alone as reference wavelength), the performance of QAA to the synthetic data set was slightly degraded. For instance, the slope and $R^2$ values for $a(440)$ changed from 1.003 and 0.994 to 0.891 and 0.978, respectively, and RMSE changed from 0.056 to 0.119. The slope and $R^2$ values for $a_{dg}(440)$ ($a_{ph}(440)$) became 0.892 and 0.969 (0.911 and 0.919, n = 477), respectively. As pointed out in Lee et al. [2002], the degradation happened to waters with large $a(440)$ (and then $a(555)$) values (mostly turbid coastal waters) where $a_w(555)$ makes less than 1/3 of the total absorption coefficient. For such cases, there will be bigger errors in the estimated $a(555)$ and then in other IOPs. If it is limited to waters with $a(440)$ less than 0.5 $m^{-1}$ (where $a_w(555)$ makes at least ~1/3 of $a(555)$), however, the performance of QAA with 555 nm as $\lambda_0$ is significantly better. The slope and $R^2$ values are close to unity (n = 334) and RMSE values are 4-5% for both total absorption and backscattering coefficients; and the RMSE are 8.4% and 14.6 % for $a_{dg}(440)$ and $a_{ph}(440)$, respectively. These results demonstrate the importance to have a red band (in the vicinity of 620 – 640 nm) for remote sensing of coastal waters and the applicability of QAA to satellite data, especially for oceanic waters.

## 10.5 Conclusions

The QAA is an algorithm based on the fundamental relationships of ocean optics, and generally follows the inversion concept described in Chapter 1. Apply QAA to the IOCCG data sets (both synthetic and *in situ*), the retrieved IOPs matched known or measured IOPs very well (in particular, absorption

coefficient of CDOM and the total and particle backscattering coefficient). As many other inversion algorithms, QAA is mathematically simple and physically transparent. These characteristics make the algorithm easily adaptable to different multi-spectral or hyperspectral sensors, and computational easy for processing satellite imageries.

Table 10.1: RMSE and regression (Type II) results of the synthetic data set ($\theta_0 = 30°$). IOPs were retrieved with $R_{rs}$ values at 410, 440, 490, 510, 555 and 670 nm. N is the number of data tested, while n is the number of valid retrieval.

| | N | n | intercept | slope | $R^2$ | RMSE | bias |
|---|---|---|---|---|---|---|---|
| $a$(410) | 500 | 500 | 0.022 | 0.999 | 0.994 | 0.057 | 0.023 |
| $a$(440) | 500 | 500 | 0.024 | 1.003 | 0.994 | 0.056 | 0.022 |
| $a$(490) | 500 | 500 | -0.001 | 0.998 | 0.991 | 0.053 | 0.001 |
| $b_{bp}$(440) | 500 | 500 | -0.039 | 0.973 | 0.988 | 0.064 | 0.013 |
| $b_{bp}$(555) | 500 | 500 | -0.006 | 1.010 | 0.991 | 0.063 | -0.026 |
| $a_{dg}$(410) | 500 | 479 | 0.014 | 0.985 | 0.992 | 0.072 | 0.025 |
| $a_{dg}$(440) | 500 | 479 | -0.003 | 0.984 | 0.986 | 0.088 | 0.012 |
| $a_{ph}$(440) | 500 | 479 | 0.099 | 1.051 | 0.928 | 0.168 | 0.033 |
| $a_{ph}$(490) | 500 | 479 | 0.126 | 1.099 | 0.770 | 0.316 | -0.021 |

Table 10.2: RMSE and regression (Type II) results of the *in situ* data set. IOPs were retrieved with $R_{rs}$ values at 412, 443, 490, 510 and 555 nm. N is the number of data tested, while n is the number of valid retrieval.

| | N | n | intercept | slope | $R^2$ | RMSE | bias |
|---|---|---|---|---|---|---|---|
| $a$(412) | 656 | 656 | -0.089 | 0.963 | 0.868 | 0.168 | -0.055 |
| $a$(443) | 656 | 656 | -0.081 | 0.969 | 0.840 | 0.175 | -0.051 |
| $a$(490) | 656 | 656 | 0.001 | 1.020 | 0.792 | 0.174 | -0.021 |
| $a_{dg}$(412) | 656 | 630 | -0.092 | 0.986 | 0.820 | 0.209 | -0.077 |
| $a_{dg}$(443) | 656 | 630 | -0.087 | 0.989 | 0.794 | 0.221 | -0.072 |
| $a_{ph}$(443) | 656 | 630 | 0.033 | 1.067 | 0.593 | 0.321 | -0.062 |
| $a_{ph}$(490) | 656 | 630 | 0.498 | 1.310 | 0.686 | 0.334 | -0.007 |

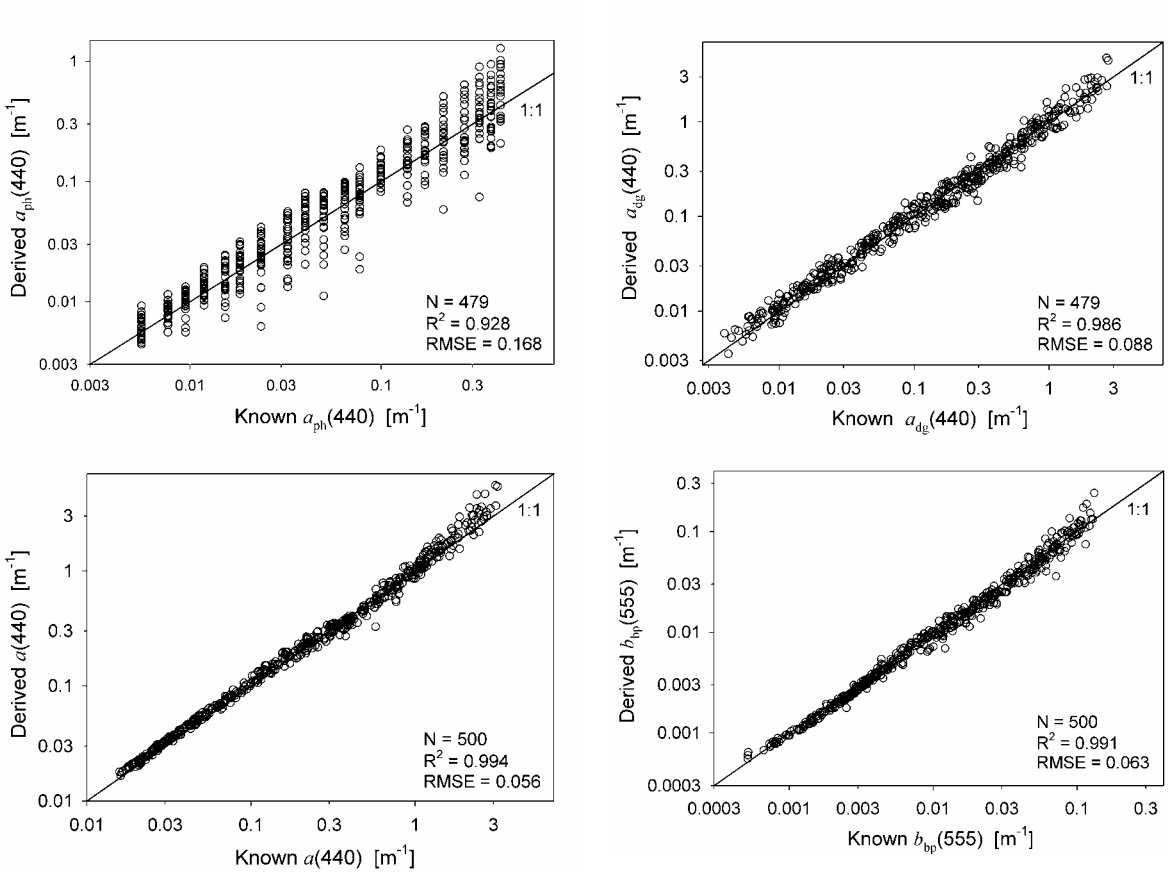


Figure 10.1. Comparison between QAA-derived IOPs and known IOPs, for the synthetic data set. IOPs were derived with $R_{rs}$ values at 410, 440, 490, 510, 555 and 670 nm as inputs (see text for details).

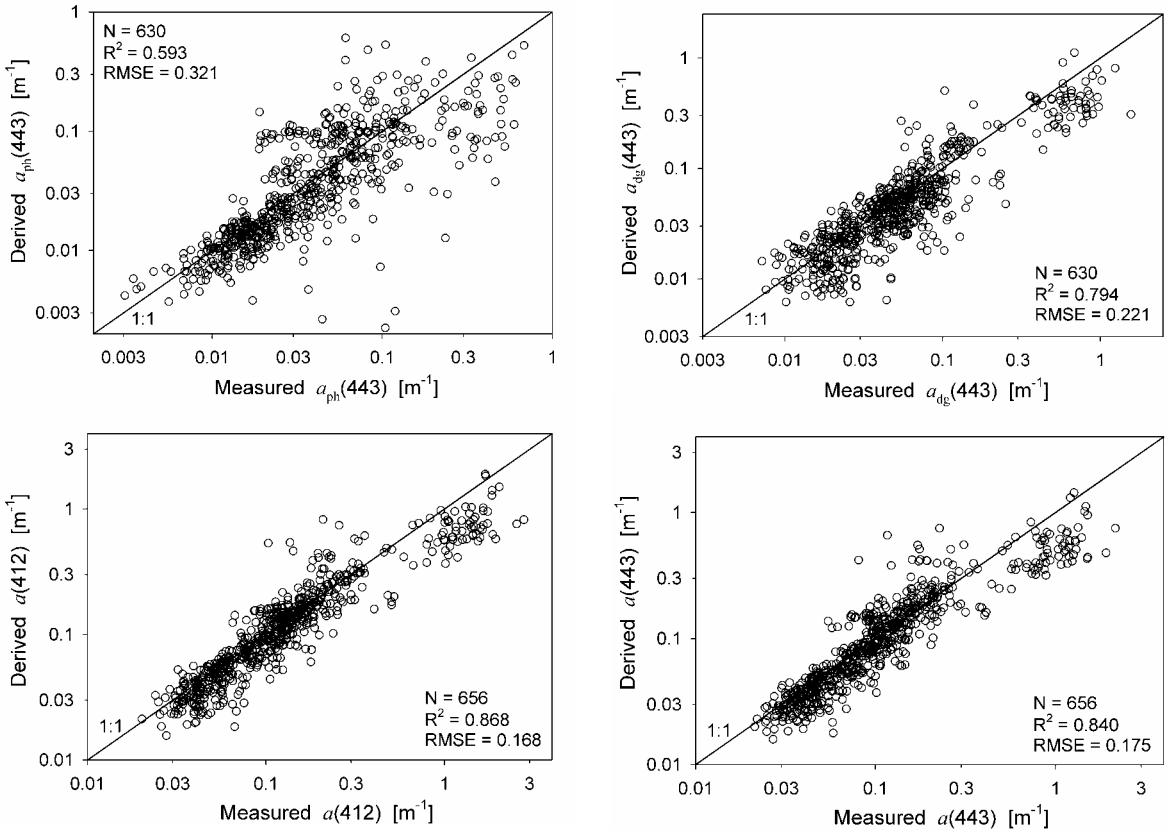


Figure 10.2. Comparison between QAA-derived IOPs and known IOPs, for the *in situ* data set. IOPs were retrieved with $R_{rs}$ values at 412, 443, 490, 510 and 555 nm as inputs.

## Chapter 11. The GSM Semi-Analytical Bio-Optical Model

Stéphane Maritorena and Dave Siegel

### 11.1 General Description

The GSM (for Garver-Siegel-Maritorena) semi-analytical ocean color model was initially developed by Garver and Siegel [1997] and later updated by Maritorena et al. [2002]. The GSM model is based on the quadratic relationship between the remote-sensing reflectance ($R_{rs}$) and the absorption and backscattering coefficients from Gordon et al. [1988],

$$R_{rs}(\lambda) = \frac{t^2}{n_w^{\,2}} \sum_{i=1}^{2} g_i \left( \frac{b_b(\lambda)}{b_b(\lambda) + a(\lambda)} \right)^i , \tag{11.1}$$

where $g_1$ (= 0.0949) and $g_2$ (= 0.0794) are geometrical factors. The absorption coefficient ($a(\lambda)$) is decomposed into seawater absorption, $a_w(\lambda)$, phytoplankton absorption, $a_{ph}(\lambda)$, and the combined absorption of colored detrital and dissolved material (CDM), $a_{dg}(\lambda)$ (considered together as a single term because of their similar spectral shapes [*Carder et al.*, 1991; *Nelson and Siegel*, 2002; *Nelson et al.*, 1998])**.** The backscattering coefficient ($b_b(\lambda)$) is partitioned into terms due to seawater, $b_{bw}(\lambda)$, and suspended particulates, $b_{bp}(\lambda)$. The non-water absorption and scattering terms are parameterized as a known shape with an unknown magnitude,

$$a_{ph}(\lambda) = Chl\, a^*_{ph}(\lambda) , \tag{11.2}$$

$$a_{dg}(\lambda) = a_{dg}(\lambda)\, \exp(-S(\lambda - \lambda_0)) , \tag{11.3}$$

$$b_{bp}(\lambda) = b_{bp}(\lambda_0) \left( \frac{\lambda_0}{\lambda} \right)^Y , \tag{11.4}$$

where $a^*_{ph}(\lambda)$ is the chlorophyll-a specific absorption coefficient, $S$ is the spectral decay constant for CDM absorption [*Bricaud et al.*, 1981], $Y$ is the power law exponent for particulate backscattering coefficient, and $\lambda_0$ is a scaling wavelength (443 nm). For $a_{ph}(\lambda)$, $a_{dg}(\lambda)$, and $b_{bp}(\lambda)$, the unknown magnitudes are the chlorophyll a concentration (Chl), the detritus/gelbstoff absorption coefficient ($a_{dg}(443)$), and the particulate backscatter coefficient ($b_{bp}(443)$), respectively. In application of Eqs. 11.1 – 11.4, $a_w(\lambda)$, $b_{bw}(\lambda)$, $n_w$, $t$, and $g_i$ are taken from the literature whereas the values of $Y$, $S$, and $a^*_{ph}(\lambda)$ were determined by "tuning" the model against a large *in situ* data set [*Maritorena et al.*, 2002] (provided in Table 11.1). The unknowns in Eqs. 11.1 – 11.4, Chl, $b_{bp}(443)$, and $a_{dg}(443)$, are retrieved by applying a nonlinear least-square technique to fit Eq. 11.1 $R_{rs}(\lambda)$ data (or normalized water-leaving radiance) collected at four or more wavelengths. Confidence intervals for the retrieved variables are also generated during the inversion (See Maritorena & Siegel [2005] and Chapter 3).

The results presented below were obtained using the set of model parameters described in Maritorena et al. [2002]. In this version, model parameters were optimized using an *in situ* data set that consisted mostly of offshore oceanic Case 1 waters with very few stations from eutrophic waters. In order to streamline the tuning process and to limit the number of unknowns to retrieve, the parameterization of the original GSM model includes some simplifying assumptions. In particular, several parameters are held constant in the model while they actually vary in nature. For example, $a^*_{ph}(\lambda)$ is expressed as a constant mean spectrum while a more sophisticated function could account for photoadaptation or community structure shifts (e.g., Bricaud et al. [1998]). Similarly, particulate backscattering is modeled using a simple function with a fixed spectral dependence (through exponent $Y$ in Eq. 11.4) while such wavelength dependence tends to disappear in turbid waters. The slope of the spectral decrease in $a_{dg}$ absorption, $S$, is also held constant in the model whereas it actually depends on a complex system

involving land/sea interactions, the productivity and state of the phytoplankton communities, the microbial loop and photochemistry (see also discussion in Maritorena et al. [2002]). Since these parameters were optimized from a large global Case 1 *in situ* data set they are generally well suited for such conditions and for the original GSM retrievals (Chl, $b_{bp}(443)$, and $a_{dg}(443)$). However, in waters where optical characteristics differ strongly from those used to tune the model, coastal Case 2 or phytoplankton rich waters in particular, the model performance can be significantly degraded. Although not presented here, other tuned versions of the model have been developed that are more appropriate for specific situations (e.g., Santa Barbara channel coastal waters).

GSM model was initially designed for use with the SeaWiFS data and chlorophyll concentration is one of its three originally retrieved variables [*Maritorena et al.*, 2002]. For consistency with some of the other models presented here, additional calculations were implemented in order to also generate total and phytoplankton absorption coefficients at 440 nm (considered negligible difference from that at 443 nm). The total absorption coefficient was calculated by solving Eq. 11.1 for $a(440)$ using the input $R_{rs}(440)$ values and the retrieved $b_{bp}(440)$. The phytoplankton absorption coefficient was then calculated by subtracting $a_w(440)$ and the retrieved $a_{dg}(440)$ value from $a(440)$. The original GSM retrieved variables have to satisfy the following criteria to be considered valid:

$0 < \text{Chl} < 100.0$ mg/m$^3$,
$0 < a_{dg}(443) < 2.0$ m$^{-1}$,
and, $0.0001 < b_{bp}(443) < 0.1$ m$^{-1}$.

## 11.2 Results

Taken the $R_{rs}$ values at 410, 440, 490, 510, and 555 nm, the variables obtained by inversion of the model were compared to the known or *in situ* data using simple regression analyses. Type II regressions on log-transformed data were performed for each of the retrieved variables. The statistical parameters presented in Table 11.2 include: the slope and intercept of the regression, $R^2$, RMSE error, bias and the number of valid retrievals.

Results of the inversion using the synthetic data set are presented in Figure 11.1. Overall, the retrievals for the four variables presented show good statistical results with small negative biases and high $R^2$ values. Slopes are greater than 1.0 for all variables and retrievals tend to slightly underestimate synthetic values at the low end and slightly overestimate at the high end. In general, dispersion tends to increase when absorption or backscattering reaches high values because as explained above this version of the model is not ideal in such conditions. Also, no valid retrievals were achieved for a small portion (about 4%) of both synthetic and *in situ* data sets.

Figure 11.2 presents the GSM retrievals when applied to the *in situ* data set. As expected, the statistical results are slightly degraded. The dispersion is higher than with the synthetic data and $R^2$ values are lower. This is likely a consequence of the noise and uncertainties associated with *in situ* AOP and IOP measurements. The slopes show the same trends as with the synthetic data but are slightly higher. In general, the GSM retrievals tend to be slightly lower than the *in situ* data.

## 11.3 Conclusions

The GSM model is a simple semi-analytical ocean color model originally designed for use with SeaWiFS and MODIS-like satellite data over non-coastal waters. While both the synthetic and *in situ* data sets used here have a strong "coastal" component, the model performed well but as expected, its performance was lower in highly absorbing or backscattering situations. Other versions of the model exist or are being developed for specific coastal waters or to implement new features (e.g., band-independent or "Trichodesmium" versions [*Westberry et al.*, 2005]).

Table 11.1. Parameters for GSM $R_{rs}(\lambda)$ inversion.

| | $a^*_{ph}(\lambda)$ [$m^2$/mg] | $S$ [$nm^{-1}$] | $Y$ |
|---|---|---|---|
| 412 | 0.00665 | 0.0206 | 1.0337 |
| 443 | 0.05582 | | |
| 490 | 0.02055 | | |
| 510 | 0.01910 | | |
| 555 | 0.01015 | | |

Table 11.2a: RMSE and regression (Type II) results of the synthetic data set ($\theta_0 = 30°$). IOPs were retrieved with $R_{rs}$ values at 410, 440, 490, 510 and 555 nm as inputs. N is the number of data tested, while n is the number of valid retrieval.

| | N | n | intercept | slope | $R^2$ | RMSE | bias |
|---|---|---|---|---|---|---|---|
| $a$(443) | 500 | 479 | 0.032 | 1.068 | 0.974 | 0.115 | -0.017 |
| $a_{dg}$(443) | 500 | 479 | 0.036 | 1.053 | 0.965 | 0.145 | -0.013 |
| $a_{ph}$(443) | 500 | 479 | 0.162 | 1.171 | 0.957 | 0.173 | -0.060 |
| $b_{bp}$(443) | 500 | 479 | 0.198 | 1.133 | 0.957 | 0.152 | -0.062 |

Table 11.2b: RMSE and regression (Type II) results of the *in situ* data set. IOPs were retrieved with $R_{rs}$ values at 412, 443, 490, 510 and 555 nm as inputs. N is the number of data tested, while n is the number of valid retrieval.

| | N | n | intercept | slope | $R^2$ | RMSE | bias |
|---|---|---|---|---|---|---|---|
| $a$(443) | 656 | 646 | -0.034 | 1.097 | 0.838 | 0.223 | -0.129 |
| $a_{dg}$(443) | 656 | 646 | 0.003 | 1.084 | 0.798 | 0.246 | -0.103 |
| $a_{ph}$(443) | 656 | 646 | 0.029 | 1.175 | 0.737 | 0.350 | -0.221 |

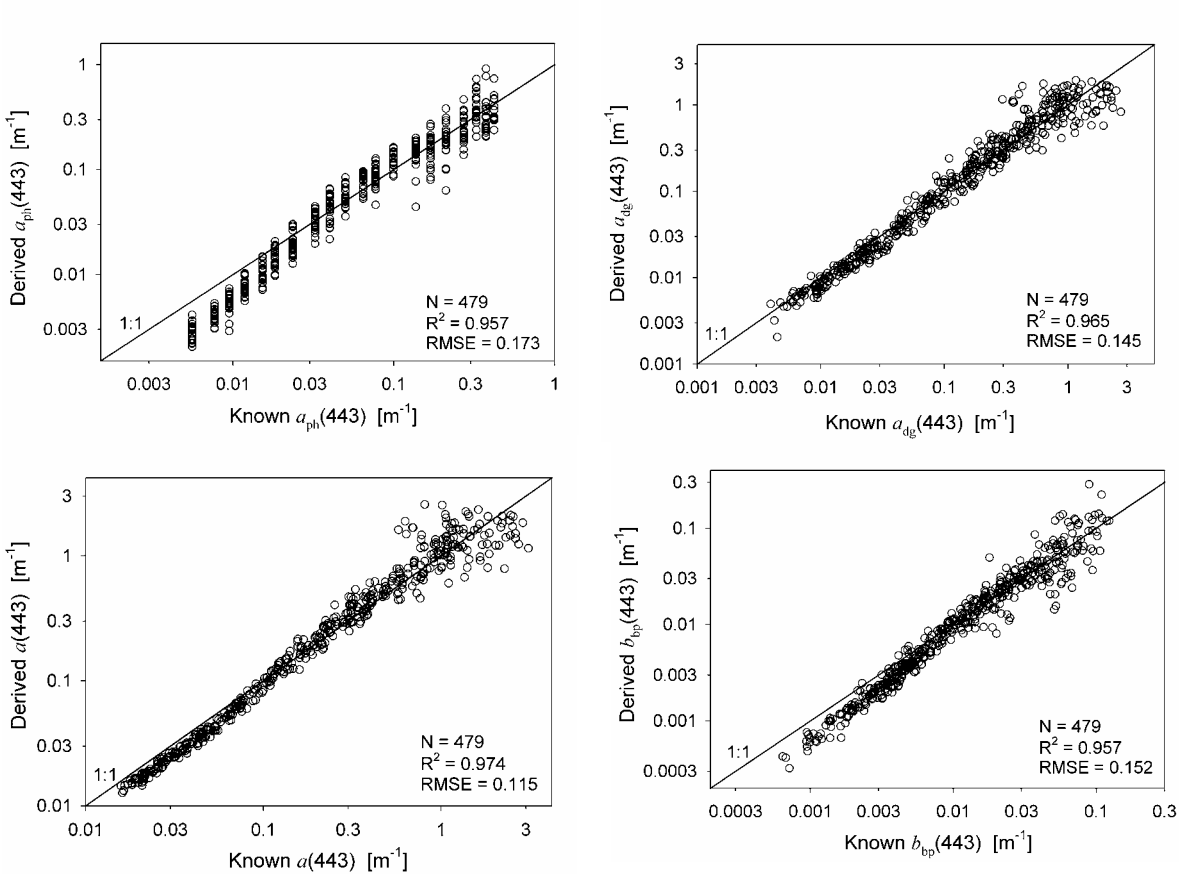


Figure 11.1. Comparison of the modeled and known IOPs for the synthetic data set using the GSM model with $R_{rs}(\lambda)$ at 410, 440, 490, 510 and 555 nm as inputs.

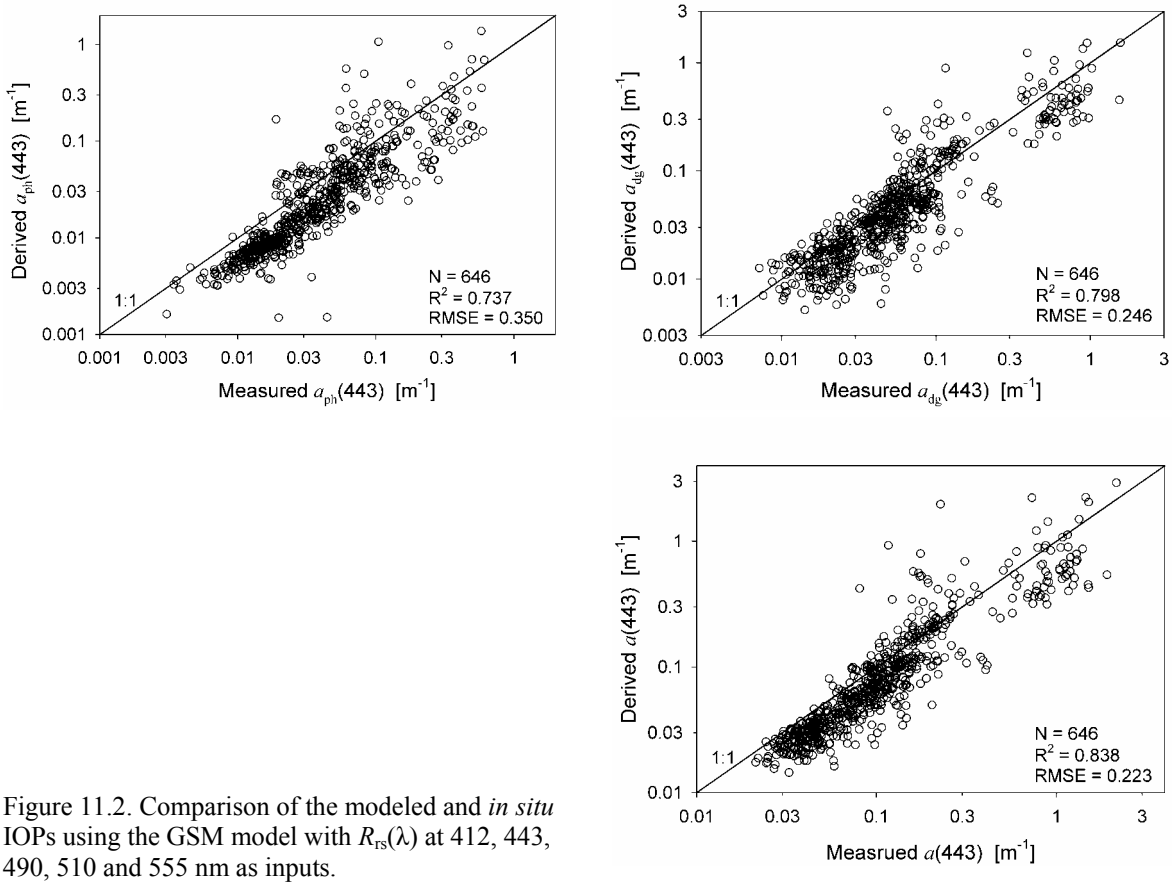


Figure 11.2. Comparison of the modeled and *in situ* IOPs using the GSM model with $R_{rs}(\lambda)$ at 412, 443, 490, 510 and 555 nm as inputs.

## Chapter 12. Inversion Based on a Semi-Analytical Reflectance Model

Emmanuel Devred, Shubha Sathyendranath and Trevor Platt

The algorithm presented here is based on the theoretical reflectance model developed by Sathyendranath and Platt [1997; 1998]. They used the assumption of quasi-single scattering to express the reflectance in the ocean as a function of the diffuse attenuation coefficient, $K_d$, which was in turn expressed as a function of IOPs. This model has since been implemented for remote sensing applications in the North West Atlantic [*Devred et al.*, 2005a; *Sathyendranath et al.*, 2001] and coastal waters off Vancouver Island [*Sathyendranath et al.*, 2004]. Although the model was designed primarily for application in Case 1 waters, the mathematical formulation [*Sathyendranath and Platt*, 1997] accounts for multiple orders of scattering, and the computer programme used in the analysis presented here incorporates scattering events up to the fifth order. Thus the model is easily adapted to more turbid Case 2 waters, such as coastal areas. Moreover, some assumptions made to develop the model (e.g., value of 1.0 for the ratio of backscattering to upward-scattering coefficients) are likely to be satisfied in turbid waters when the angular distribution of radiance tends to isotropy. This model has been widely used for various applications ranging from chlorophyll concentration retrieval to primary production computations. Here it is coupled with a nonlinear, least-square fitting method to retrieve IOPs (absorption and backscattering coefficients) of marine components (phytoplankton and detrital material, dissolved and particulate) from remote-sensing reflectance, $R_{rs}$.

### 12.1 Theoretical Background

Sub-surface irradiance reflectance ($R(0^-,\lambda)$) is expressed as the ratio of upwelling irradiance ($E_u$) to downwelling irradiance ($E_d$) just below the surface. Sathyendranath and Platt [1997] showed that $R(0^-,\lambda)$ for a homogeneous water column can be expressed as:

$$R(0^-,\lambda) = \frac{s\, b_b(\lambda)}{\mu_d\,(K_d(\lambda) + \kappa(\lambda))}, \tag{12.1}$$

where $K_d(\lambda)$ and $\kappa(\lambda)$ are respectively the diffuse attenuation coefficients ($m^{-1}$) for downwelling and upwelling irradiance (note that $\kappa(\lambda)$ defines the rate of attenuation of upwelling light as it travels to the surface, and that this is different from the attenuation coefficient for upwelling light with increasing depth), $\mu_d$ is the average cosine for the downwelling irradiance, $s$ is a shape factor defined as the ratio of upward scattering coefficient $b_u$ ($m^{-1}$) to backscattering coefficient $b_b$ ($m^{-1}$). The parameter $s$ takes the value of 1.0 in very oligotrophic waters where the molecular scattering is dominant. The average cosine for downwelling irradiance ($\mu_d$) just beneath the sea surface can be written as the sum of a direct and a diffuse component (Eq. 12.2).

The cosine for the direct component is equal to $\cos(\theta_s)$ where $\theta_s$ is the subsurface solar zenith angle and mean cosine for the diffuse component is 0.83 [*Sathyendranath and Platt*, 1988]. Thus, the mean cosine for the total downwelling irradiance at the sea surface is given by:

$$\mu_d = \frac{I_d \cos(\theta_s)}{I_0} + \frac{0.83 I_s}{I_0}, \tag{12.2}$$

where $I_0$, $I_d$ and $I_s$ correspond respectively to the total, direct and diffuse solar radiation at the sea surface [*Gregg and Carder*, 1990]. Further details regarding the assumptions and approximations in the ocean-colour model used here are available in Sathyendranath and Platt [1997].

Sathyendranath and Platt [1988] have expressed the diffuse attenuation coefficient as (wavelength argument is omitted here for clarity),

$$K_d = \frac{a + b_b}{\mu_d}, \tag{12.3}$$

and similarly,

$$\kappa = \frac{a + b_b}{\mu_u}, \tag{12.4}$$

where $\mu_u$ corresponds to the mean cosine for the upwelling light, which is approximated as 0.5.

From Eqs. 12.1 – 12.4, the reflectance $R$ can be expressed as a function of backscattering and absorption coefficients of the marine components at a given wavelength. This model has also been extended to deal with stratified waters and inelastic (Raman) scattering [*Sathyendranath and Platt*, 1998]. However, these features of the model are not exploited here to facilitate comparison with the other models in this report. The model has been used to provide a theoretical underpinning for empirical algorithms for retrieval of chlorophyll-a from ocean colour data [*Sathyendranath et al.*, 2001], and to develop improved algorithms for chlorophyll-a retrieval for Case 1 waters of the North West Atlantic [*Devred et al.*, 2005a]. Here, we examine the use of a nonlinear optimization technique to retrieve optical properties of the IOCCG data sets that include both Case 1 and Case 2 waters.

## 12.2 The Approach

To retrieve the inherent optical properties from remote-sensing reflectance, we applied a classical nonlinear least-square fitting method to Eq. 12.1. At a given wavelength, the reflectance at the sea surface is a function of five unknown parameters: $R = f(a_{ph}, a_g, a_d, b_{b,ph}, b_{b,p})$ where subscripts *ph*, *y*, *d* and *p* stand respectively for chlorophyll (phytoplankton), yellow substances (also referred to as CDOM), detritus and other particulate material, when the absorption and backscattering coefficients in the model are expressed as the sums of their components. Note that absorption ($a_w$) and backscattering ($b_{bw}$) by pure seawater can be computed at a given wavelength (see respectively Pope and Fry [1997] and Morel [1974]) and do not appear as unknown parameters in the above equation. Further, based on historical measurements and bio-optical models [*Bricaud et al.*, 1995; *Bricaud et al.*, 2004; *Bricaud et al.*, 1981; *Ciotti et al.*, 2002; *Devred et al.*, 2005b; *Loisel and Morel*, 1998; *Ulloa et al.*, 1994], the spectral dependencies of those components are described as follows:

$$a_{dg}(\lambda) = a_{dg}(440)\exp\left[-S(\lambda - \lambda_0)\right], \tag{12.5}$$

for combined absorption coefficients of yellow substances ($a_g$) and detritus ($a_d$) at $\lambda$, where $S$, the exponential decrease of absorption with decreasing wavelength, is set to the average value of 0.014 nm$^{-1}$; and

$$b_{bp}(\lambda) = b_{bp}(440)\left(\frac{\lambda}{440}\right)^{-\log(Chl)}, \tag{12.6}$$

for particulate backscattering (organic and mineral). Note that the wavelength dependence model is also a function of chlorophyll concentration (*Chl*, mg/m$^3$) as in Sathyendranath et al. [2001].

The model of Sathyendranath et al. [2001] was used to describe phytoplankton absorption,

$$a_{ph}(\lambda) = U(\lambda)(1 - \exp(-f\ Chl)) + a_2^*(\lambda)\, Chl\,. \tag{12.7}$$

Values of $U(\lambda)$, $f$ and $a_2^*(\lambda)$ are provided in Table 12.1, whereas details on interpretation of these parameters can be found in Devred et al. [2005b]. The three parameters of the model were determined by fitting the model to the data base at the Bedford Institute of Oceanography.

With the above prescriptions on the spectral dependencies of the optical properties of some of the components, and by combining the absorptions by detritus and yellow substances into a single component (Eq. 12.5), the number of unknown parameters in Eq. 12.1 is reduced to four (namely, $a_{ph}(440)$, $a_{dg}(440)$, $b_{bp}(440)$ and *Chl*). When remote-sensing reflectance at 410, 440, 490, 510, 555 and 670 nm are available from ocean colour sensors (for example, SeaWiFS, MODIS and MERIS, which are the most commonly-used), we get a system of six equations with four unknowns. This facilitates the convergence on the solution for the four unknowns. Note that parameters $b_{bp}(\lambda)$ and $a_{ph}(\lambda)$ are related to *Chl* through Eqs. 12.6 – 12.7. However, $a_{ph}(440)$ was determined independent of *Chl* in our algorithm. *Chl* was used only to the process of deriving $a_{ph}$ and $b_{bp}$ at other wavelengths.

To apply our approach to the IOCCG data sets (both synthetic and *in situ*), the reflectance $R$ was estimated from remote-sensing reflectance, $R_{rs}$, using:

$$R = \frac{n_w^2}{t^2} Q\, R_{rs}\,. \tag{12.8}$$

Here $n_w^2/t^2$ ($\approx 1.89$) accounts for the air-sea interface effects, and $Q$ converts radiance to irradiance. It is known that the factor $Q$ varies with solar zenith angle, sea-surface roughness (wind-induced) and substances present in the water. Here, the dependence of $Q$ on solar zenith angle was computed using the model of Åas and Højerselev [1999] and an empirical function [*Devred et al.*, 2005a] was used to compute the dependence of $Q$ on chlorophyll content [*Morel and Gentili*, 1993].

## 12.3 Results and Discussion

We used remote-sensing reflectance at 410, 440, 490, 510, 555, and 670 nm (note that $R_{rs}(670)$ is not available for the *in situ* data set) of the IOCCG data sets to derive total, phytoplankton, and detrital (dissolved and particulate) absorption coefficients, and particulate backscattering coefficient at 440 nm.

### 12.3.1 Retrieval of IOPs from the simulated data set

The interest in inverting synthesized data lies in the control of all environmental variables such as the sea surface state, solar zenith angle and optical properties. It is then possible to assess accurately the performance of the reflectance model and the fitting method to retrieve inherent optical properties.

Figure 12.1 shows derived versus synthesized total, phytoplankton and detritus absorption coefficients and particulate backscattering at 440 nm for data with a solar zenith angle of 30°. The retrieved data are consistent with the simulated data. For each of the derived IOPs, the optimization method failed to retrieve the parameters in eight cases for absorption of phytoplankton, and yellow substances and detritus. Linear regression (Type II) on log-transformed data (omitting the cases where convergence was not obtained) gave slopes close to 1.0 (except for phytoplankton absorption with a slope of 1.16) with small negative bias for all variables (Table 12.2). Note that similar results were also achieved with the synthesized data of $60^o$ solar zenith angle (not shown). This demonstrates that the assumptions made on the spectral dependence of the IOPs with average parameters are acceptable.

Matching of phytoplankton absorption coefficients presents the poorest agreement (although still acceptable) with a slope of 1.156 and a bias of -0.053. It also exhibits the lowest correlation coefficient with a value of $R^2 = 0.827$. One observes an increase of discrepancy in the retrieved data (Figure 12.1) as $a_{ph}(440)$ increases. This is probably due to the phytoplankton absorption model used in our algorithm. It is noteworthy that the retrieved total absorption at 440 nm shows a better agreement than does the retrieved phytoplankton absorption. At low backscattering coefficients ($b_{bp}(440) < 0.002$ m$^{-1}$) our algorithm showed a systematic underestimation of the retrieved backscattering. It probably results from the formulation of the spectral dependence of the backscattering coefficients with respect to chlorophyll concentration. This approach may not be appropriate at low chlorophyll concentrations, and therefore for low backscattering coefficients. We will explore this problem further.

### 12.3.2 Retrieval of IOPs from the *in situ* data set

Inversion of *in situ* measurements becomes more challenging not only because the parameters defined in the previous section (IOPs, sun angle, vertical profile) show random and/or systematic variability in their natural environment, but also because external variables (for example, measurement errors) add perturbation to the entire system (defined here as the reflectance/IOP pairs). We can therefore expect a higher variability when retrieving the IOPs as confirmed in Figure 12.2. Only results for absorption coefficients are shown in Figure 12.2 because backscattering measurements were not available.

The standard deviation has increased for all of the matching pairs (Table 12.3). Retrieved phytoplankton absorption coefficients show the highest discrepancy with the *in situ* data (slope of 1.537 and bias of -0.110), perhaps because of the performance of the absorption model. Previous works [*Burenkov et al.*, 2001; *Devred et al.*, 2005a; *Gohin et al.*, 2002; *Reynolds et al.*, 2001; *Sathyendranath et*

*al.*, 2001] showed that local bio-optical models should be preferred to global ones. This type of approach would likely decrease the discrepancy between the retrieved and *in situ* data. Comparison between retrieved and *in situ* absorption coefficients of yellow substances and detritus is also less consistent (slope of 1.312 and bias of -0.003) than the previous case (synthesized data set). In Figure 12.2, cases where the fitting procedure for $a_{dg}(440)$ failed to converge are shown as filled triangles. These points were not retained in the statistical analysis (resulted smaller number of samples). The total absorption coefficients show a good agreement with a slope of 1.048 and a bias of -0.036. This is not inconsistent as phytoplankton absorption seemed to be slightly overestimated while yellow substances are underestimated. These effects cancelled each other, resulting in a better agreement when comparing the total absorption coefficients.

### 12.4 Conclusion

The reflectance model of Sathyendranath and Platt [1997], although based on the quasi-single scattering assumption, proved to be robust when applied to a great variety of optical marine environments, to cases ranging from low to high albedo (scattering to absorption coefficients ratio).

Retrieval of inherent optical properties shows better accuracy when performed on the synthesized data set at low solar zenith angle. A small decrease in the accuracy was observed as solar zenith angle increased (not presented). A greater discrepancy occurred when retrieving phytoplankton absorption at 440 nm than for other IOPs. This may be explained by the phytoplankton absorption model used in our algorithm. However, retrieval of the total absorption coefficient seems not affected by this feature. Our algorithm underestimated backscattering coefficients at small values, perhaps a limitation of our bio-optical model adapted from Loisel and Morel [1998].

For the *in situ* data set, our algorithm yielded consistent results, although a greater variability around the 1:1 line was observed than that observed when inverting the synthesized data set. We showed that an underestimation (overestimation) of retrieved phytoplankton absorption lead to an overestimation (underestimation) of retrieved yellow substances absorption (not knowing which one is the cause). This will be further analysed to improve the performance of our algorithm. However, our algorithm yielded results comparable to other models reported here.

Table 12.1. Parameters for $a_{ph}(\lambda)$ model.

| wavelength | $U(\lambda)$ | $a^*_2(\lambda)$ ($m^2$/mg) | $f$ |
|---|---|---|---|
| 412 | 0.0369 | 0.0243 | 1.5815 |
| 490 | 0.0338 | 0.0129 | |
| 510 | 0.0180 | 0.0114 | |
| 555 | 0.0036 | 0.0070 | |
| 670 | 0.0089 | 0.0172 | |

Table 12.2. RMSE and regression (Type II) results for the synthetic data set (Sun at 30°). IOPs were retrieved using $R_{rs}$ values at 410, 440, 490, 510, 555 and 670 nm. N is the number of data tested, while n is the number of valid retrieval.

| | N | n | intercept | slope | $R^2$ | RMSE | bias |
|---|---|---|---|---|---|---|---|
| $a(440)$ | 500 | 500 | -0.122 | 0.974 | 0.960 | 0.166 | -0.104 |
| $b_{bp}(440)$ | 500 | 500 | -0.093 | 0.981 | 0.938 | 0.160 | -0.056 |
| $a_{ph}(440)$ | 500 | 492 | 0.145 | 1.156 | 0.827 | 0.288 | -0.053 |
| $a_{dg}(440)$ | 500 | 492 | -0.119 | 1.090 | 0.873 | 0.348 | -0.200 |

Table 12.3. RMSE and regression (Type II) results for the *in situ* data set. IOPs were retrieved using $R_{rs}$ values at 410, 440, 490, 510 and 555 nm. N is the number of data tested, while n is the number of valid retrieval.

| | N | n | intercept | slope | $R^2$ | RMSE | bias |
|---|---|---|---|---|---|---|---|
| $a(443)$ | 656 | 656 | 0.011 | 1.048 | 0.762 | 0.218 | -0.036 |
| $a_{ph}(443)$ | 656 | 656 | 0.654 | 1.537 | 0.648 | 0.442 | -0.110 |
| $a_{dg}(443)$ | 656 | 491 | 0.416 | 1.312 | 0.380 | 0.470 | -0.003 |

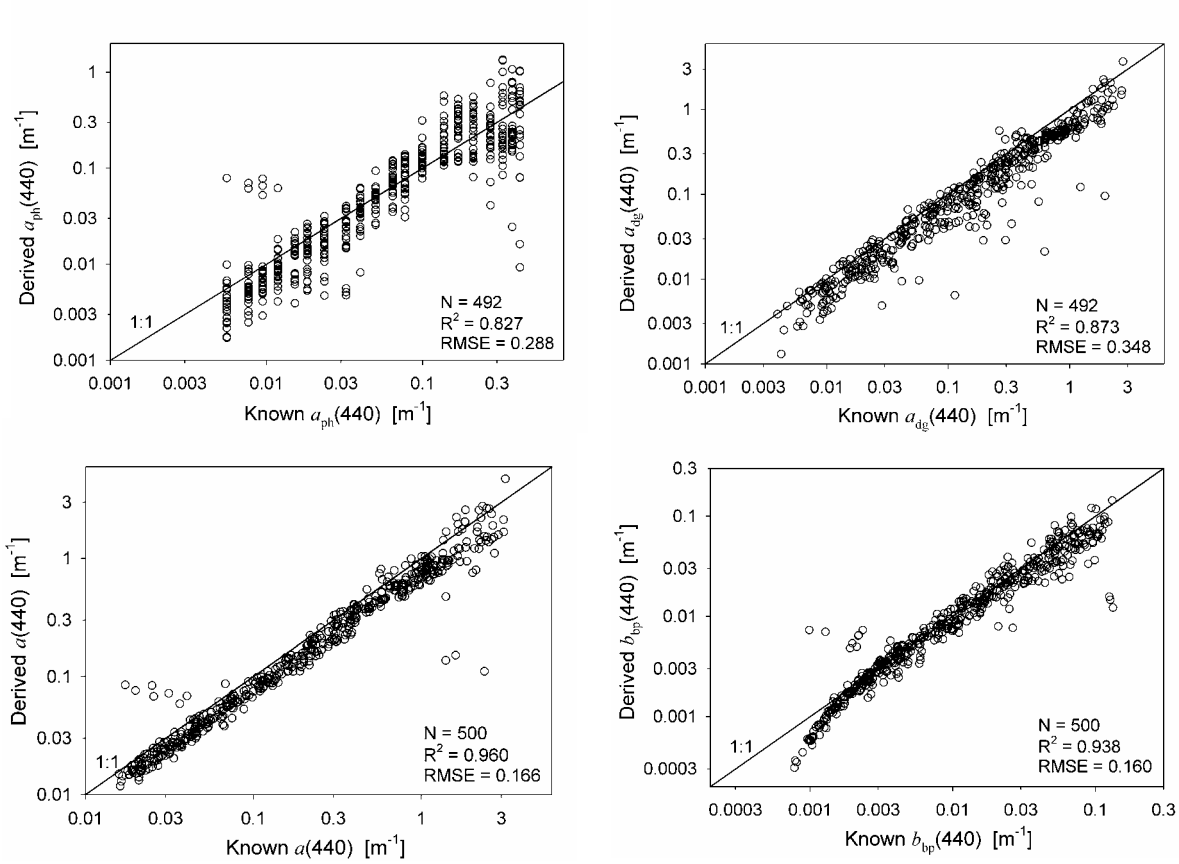


Figure 12.1. Comparison between retrieved and simulated IOPs for a solar zenith angle of 30°. IOPs were retrieved using $R_{rs}$ values at 410, 440, 490, 510, 555 and 670 nm.

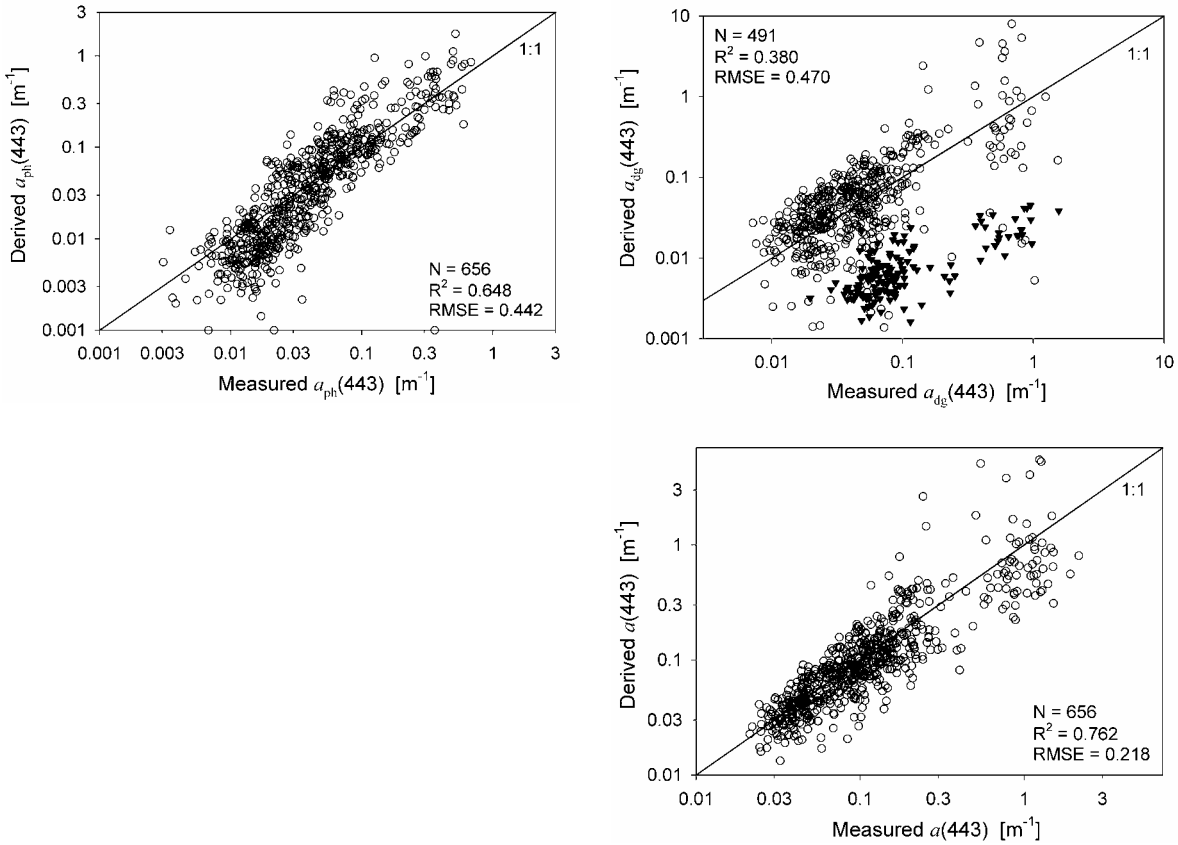


Figure 12.2. Comparison between retrieved and *in situ* IOPs. IOPs were retrieved using $R_{rs}$ values at 412, 443, 490, 510 and 555 nm.

## Chapter 13. Examples of IOP Applications

Robert Arnone, Hubert Loisel, Kendall Carder, Emmanuel Boss, Stephane Maritorena, ZhongPing Lee

The IOPs retrieved from ocean color provide innovative tools and opportunities for oceanographic studies, as their values can be used directly or indirectly to study biological and biogeochemical processes in the oceans (e.g., Bissett et al. [2001], Gould and Arnone [1997], Coble et al. [2004], Hu et al. [2004; 2005]). For instance, earlier studies (e.g., Kirk [1984] and Sathyendranath and Platt [1988]) have shown that the diffuse attenuation coefficients of the water can be adequately estimated from water's inherent optical properties. Recent studies [*Balch et al.*, 2005; *Loisel et al.*, 2001a; *Stramski et al.*, 1999] have shown that particulate carbon can be well estimated from particle backscattering coefficient. Further, a new generation of biological models [*Bissett et al.*, 2005; *Penta et al.*, 2005] now integrate explicitly two or more species of plankton, as well as dissolved (DOC) and particulate organic carbon (POC), whereas IOPs play important roles in observing and monitoring blooms of red tides [*Cannizzaro et al.*, 2005; *Cullen et al.*, 1997]. As confidence in the IOP products continues to grow, our understanding of how IOP properties are linked to ocean processes expands. These researches are moving the ocean community beyond the traditional applications centered on the oceanic chlorophyll. In this chapter, we present some examples of IOP applications in this regard.

### 13.1 Water Composition and Water-Mass Classification

The absorption and backscattering coefficients bring some complementary information on the water composition, because of their different sensitivity to the various optically significant materials in water. While the absorption coefficient is affected by the presence of both suspended and dissolved material in water, the backscattering coefficient represents the concentration (to first order) of organic and inorganic suspended particles, and bubbles. The decomposition of total absorption coefficient into its different components, as discussed in this report (Chapter 1), allows the monitoring of phytoplankton and of the remaining absorbing materials. Therefore, synoptic satellite observations of $a$ and $b_b$ give a valuable picture of composition of surface waters. For example, the $b_{bp}/a$ ratio may be used to discriminate different families of particles (Figure 13.1).

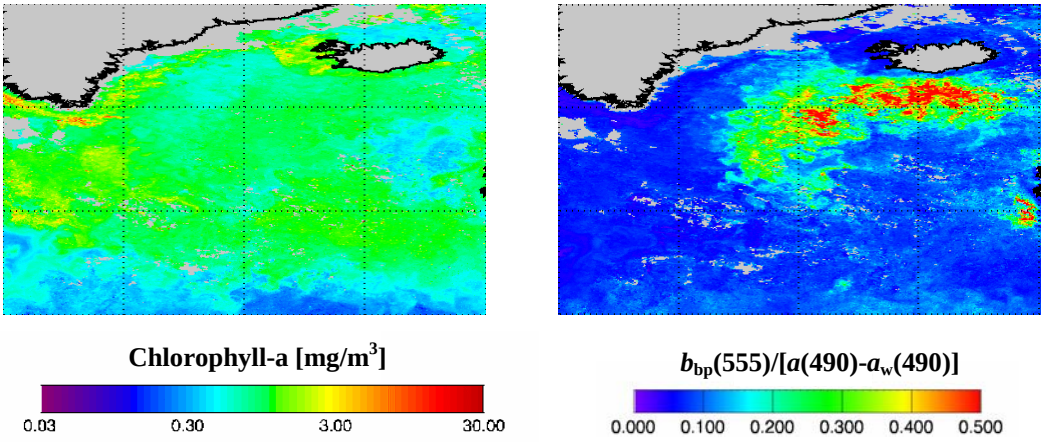


Figure 13.1. Comparison between the SeaWiFS-Chlorophyll concentration and the ratio of the particle backscattering to absorption obtained from an inverse algorithm [*Loisel and Stramski*, 2000] over the North Atlantic (south Island) in May 1998. As seen, Chl and $b_{bp}(555)/[a(490)-a_w(490)]$ represent different patterns, with the latter clearly showing different particle populations. These particles have been identified as coccolithophorid, which are characterized by a high backscattering efficiency.

New applications have also used water's IOP characteristics as a tool to fingerprint a water mass and identify the controlling optical processes [*Arnone and Parsons*, 2004]. Besides water absorption, the total absorption is additionally composed of the absorption from CDOM, detritus and phytoplankton (see Chapter 1). By defining the percent contribution of each of these components, a water mass can be defined by which component controls the absorption budget. A ternary plot of these three components provides a useful method for fingerprinting water mass and the dominant absorption process [*Arnone et al.*, 2004; *Gould and Arnone*, 2003]. This method has been applied to satellite absorption properties derived from semi-analytical algorithms for SeaWiFS and MODIS ocean color imagery (Fig. 13.2a). This water-mass classification can be represented by an RGB image representing percent detritus, phytoplankton and CDOM absorption (Fig. 13.2b). These images easily illustrate the controlling biogeochemical processes for monitoring coastal and offshore water masses. Note that this classification method identifies the dominance of the absorption processes, and not the absolute values of the absorption coefficients. This classification method can be used on sequential satellite images of the absorption components to 1) identify changes in absorption processes and 2) tracking water masses based on a specific fingerprint of the absorption components.

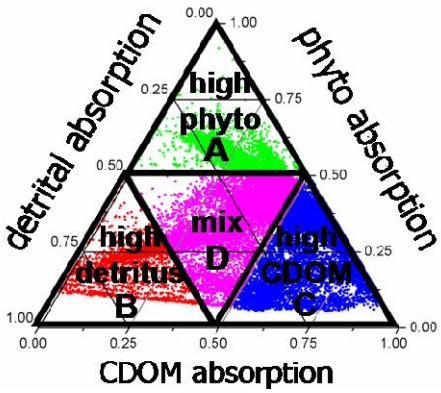


Figure 13.2(a). Water-mass classification from the absorption budget. Ternary plot of the percent absorption for detritus, CDOM and phytoplankton for pixels identifies the dominant components.

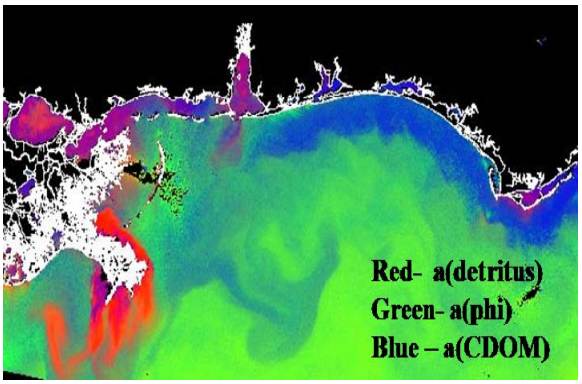


Figure 13.2(b). RGB image of percent absorption of detritus (Red), phytoplankton (green) and CDOM (blue). Absorption products derived from SeaWIFS were used to determine the absorption budget. Intensity of the color indicates the dominant component.

## 13.2 Dissolved and Particulate Organic Carbon

Examinations of the temporal variations of absorption and backscattering coefficients and comparison with that of Chl over the global ocean have also provided important information about the dynamics of marine particles and dissolved organic carbon, because the absorption and backscattering coefficients are related to different biogeochemical parameters. For instance, the feasibility of estimating POC (in $mg/m^3$), and the colored detrital and dissolved materials (CDM) (in $m^{-1}$), from the remotely detected $b_b$ and $a$ was recently demonstrated [*Balch et al.*, 2005; *Loisel et al.*, 2002; *Loisel et al.*, 2001b; *Siegel et al.*, 2002; *Stramski et al.*, 1999] (see Figs. 13.3 and 13.4). A phase shift between the annual cycles of $b_{bp}$ and Chl was evidenced, and was attributed to the presence of a pool of non-pigmented particles originating from the accumulation of dead phytoplankton cells, as well as zooplankton detritus, in the summer stratified surface layer [*Loisel et al.*, 2002]. "*The decrease of the* Chl/POC *ratio in living phytoplankton at high irradiance in summer*" was also used to explain "*the lag between the* Chl *and* $b_{bp}$ *maxima*" [*Loisel et al.*, 2002].

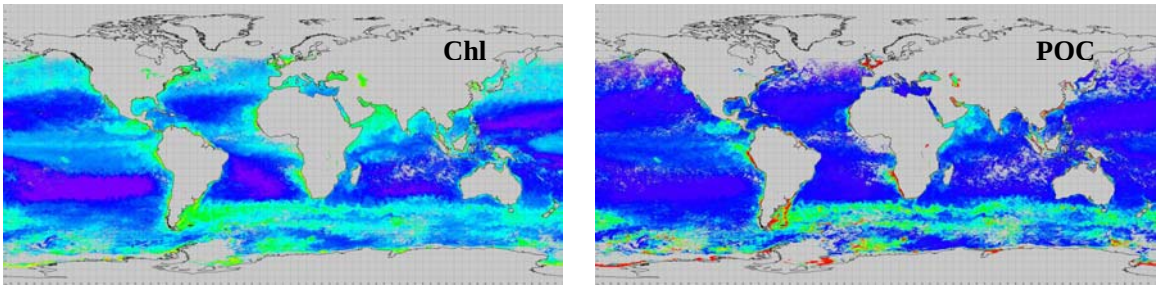


Figure 13.3. Global Chl (SeaWiFS product) and POC [*Loisel et al.*, 2002] distribution in January 2000.

Figure 13.4 shows global distributions of CDM of two seasons in 1998, derived from SeaWiFS data [*Siegel et al.*, 2002]. Clearly, there are significant spatial and temporal variations in global CDM (a part of DOC). Because POC and CDM represent different pools of carbon stored in oceans, and that CDM plays important role in regulating subsurface blue/ultraviolet radiation [*Siegel et al.*, 2002], analysis of their spatial/temporal distributions is important for the understanding of the carbon cycles in oceans.

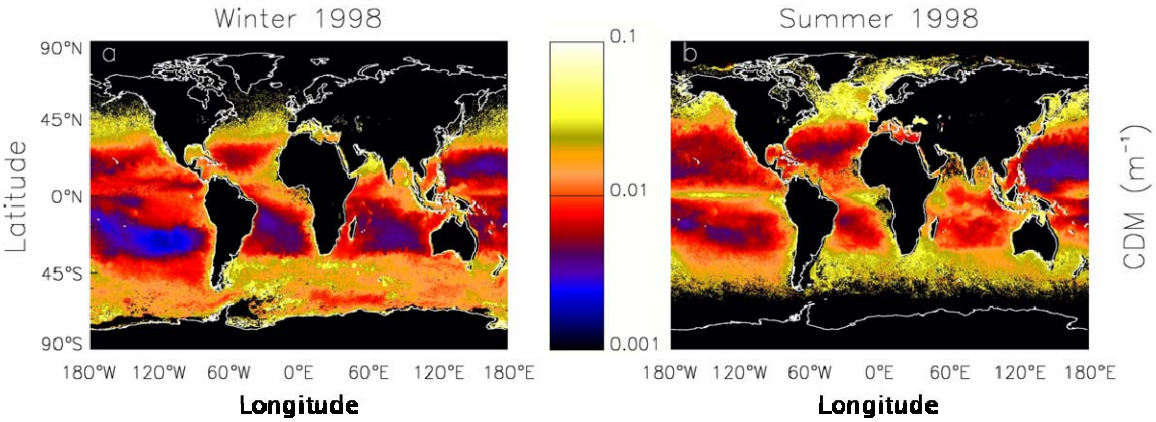


Figure 13.4. Global distribution of CDM (in $m^{-1}$) derived from SeaWiFS data by the GSM algorithm (Ch. 11) [*Siegel et al.*, 2002].

Behrenfeld et al. [2005], using backscattering and chlorophyll derived from $R_{rs}$ as inputs, also developed a novel primary production model based on the physiological link between phytoplankton growth rate and growth conditions (temperature, nutrients, and light) as reflected in the ratio of chlorophyll to carbon of phytoplankton. This novel (and debatable) approach is to use the backscattering coefficient to estimate phytoplankton biomass and assuming a linear relation between total POC and phytoplankton biomass. The observed change (Fig. 13.5) in the ratio of chlorophyll to phytoplankton carbon is interpreted as reflecting a physiological change, rather than a change in the particulate composition. Net primary production is then computed from the estimated growth rate through a simple multiplication by the phytoplankton carbon and a function that accounts for its vertical distribution with depth.

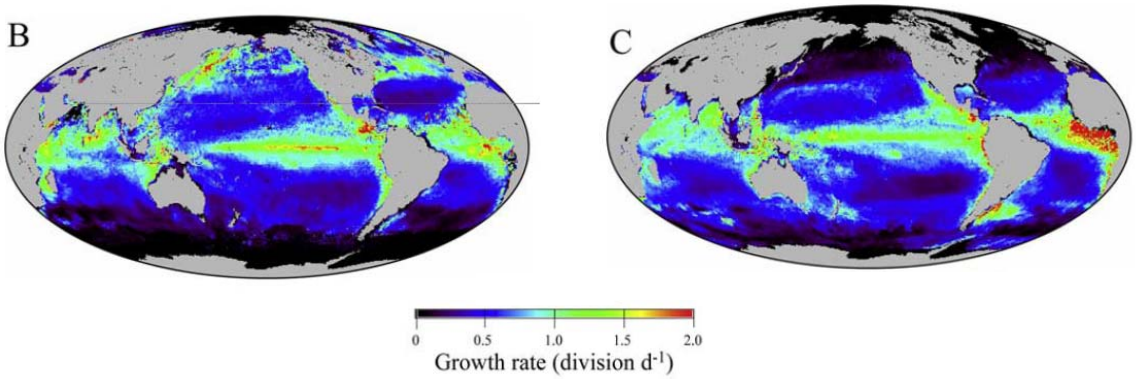


Figure 13.5. Phytoplankton growth rates for Boreal: summer (left, June to August), winter (right, December to February). From Behrenfeld et al. [2005].

### 13.3 Diffuse Attenuation Coefficient of Downwelling Irradiance

The availability of absorption ($a$) and backscattering coefficients ($b_b$) also makes it straightforward to calculate the diffuse attenuation coefficient of downwelling irradiance, either at a single wavelength ($K_d(\lambda)$) or for the broad band (350 – 700 nm) visible domain ($K_{VIS}$). Because both $K_d$ and $K_{VIS}$ are apparent optical properties, they are directly linked to the IOPs [*Gordon*, 1989; *Lee et al.*, 2005a; *Lee et al.*, 2005b; *Sathyendranath and Platt*, 1988]. Traditionally, estimation of $K_d$ is based on the spectral ratios of $L_w(\lambda)$ or $R_{rs}(\lambda)$. Such an approach does not reveal the fundamental relationship between AOPs and IOPs, and is found to only work for waters with limited dynamic range [*Mueller*, 2000]. For a wide range of $K_d(490)$ (~0.04 – 4.0 $m^{-1}$) measured from different regions and at different times, Figure 13.6(a) shows a comparison between measured $K_d(490)$ and $R_{rs}$ derived $K_d(490)$, using an algorithm based on $a$ and $b_b$ whose values were derived first from $R_{rs}$ [*Lee et al.*, 2005b]. Clearly, excellent agreement is achieved between the two independent measurements and determinations.

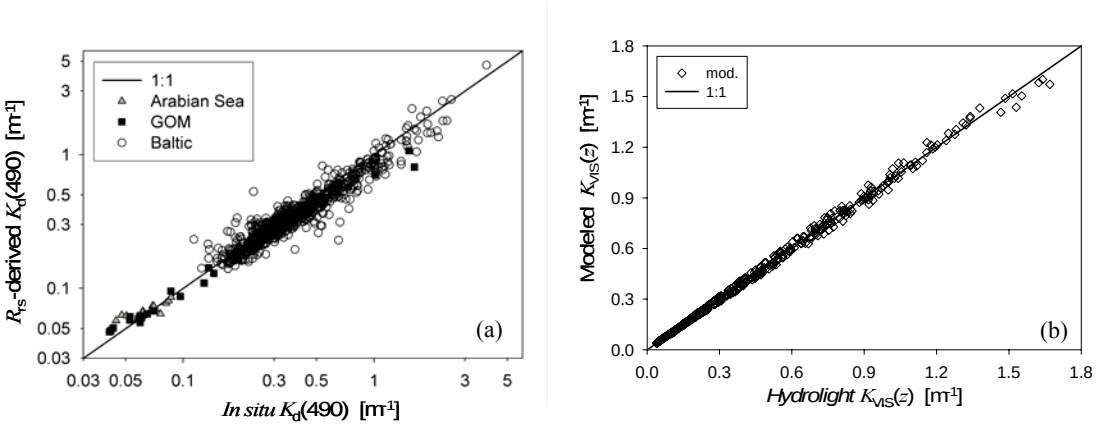


Figure 13.6. (a) Measure $K_d(490)$ vs $R_{rs}$-derived $K_d(490)$. In the derivation of $K_d$ from $R_{rs}$, values of $a$ and $b_b$ were derived from $R_{rs}$ first, and then $K_d$ is calculated based on these $a$ and $b_b$ values. From Lee et al. [2005b]. (b) Modeled $K_{vis}(z)$ compared with $K_{vis}(z)$ from Hydrolight simulations. From Lee et al. [2005a].

$K_{VIS}$ (wavelength range of 350 – 700 nm) is a parameter needed for models of oceanic photosynthesis and heat transfer in the upper water column. Different from the characteristics of $K_d$, $K_{VIS}$

varies significantly from the surface to a depth ($z$) even for vertically homogeneous waters. To represent this vertical variation, earlier studies used multiple exponential terms to describe the vertical propagation of visible solar radiation, with the coefficients of these multiple terms expressed as empirical functions of Chl [*Morel and Antoine*, 1994; *Ohlmann and Siegel*, 2000]. Again, realizing the intrinsic limitation between an optical property (e.g., $K_{VIS}$) and Chl, a model has been developed [*Lee et al.*, 2005a] that can be used to adequately estimate the vertical variation of $K_{VIS}$ when values of $a(490)$ and $b_b(490)$ are available, with Fig. 13.6(b) showing modelled $K_{VIS}$ compared with Hydrolight-calculated $K_{VIS}$ for different values of $a$, $b_b$, and $z$. The average difference between the two sets of $K_{VIS}(z)$ is 2.2%.

### 13.4 Oceanic Primary Production

Knowing the values of IOPs also provides some basic information for the estimation of oceanic primary production. Currently, this estimation is done centred on the values of chlorophyll [*Behrenfeld and Falkowski*, 1997; *Platt and Sathyendranath*, 1988]. When Chl is used as an input parameter representing the function of phytoplankton, a value regarding the Chl-specific absorption coefficient is also utilized, explicitly or inexplicitly. Numerous field measurements [*Bricaud et al.*, 1995; *Bricaud et al.*, 1998; *Cleveland*, 1995; *Lutz et al.*, 1996] and theoretical studies [*Bricaud and Morel*, 1986] have pointed out that this property varies widely from place to place and time to time, therefore large uncertainties are automatically introduced when this parameter is involved. Because primary production measures the conversion of solar energy absorbed by phytoplankton to sustenance in the photosynthetic process [*Morel*, 1978; *Smith et al.*, 1989], remotely derived or locally measured phytoplankton absorption and other IOPs can then be directly utilized in this estimation [*Zaneveld et al.*, 1993]. One example of taking this approach is demonstrated in Lee et al. [1996b], with Fig. 13.7 showing primary production calculated from values of $R_{rs}$ (along with other auxiliary information) compared with primary production measured from *in situ* incubation.

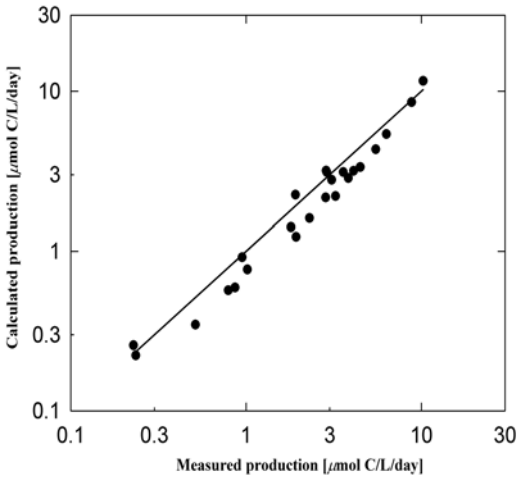


Figure 13.7. Daily primary production calculated from $R_{rs}$ versus that from *in situ* incubation. From Lee et al. [1996b].

### 13.5 Chl from Remotely Derived Pigment Absorption Coefficient

When the absorption coefficient of phytoplankton pigment is derived from ocean color, it adds the possibility of deriving Chl [Carder et al., 1999; Lyon et al., 2004] for different regions of the world, as indicated in Carder et al. [1999]. Applying the semi-analytic (SA) code [Carder et al., 1999] to an upwelling site [Smyth et al., 2002] and a river-plume site [Hu et al., 2003], it provided much more realistic estimations of Chl for both cases; where the empirical band-ratio approach (OC4) underestimated the high Chl of the upwelling site and overestimated Chl for gelbstoff-rich river-plume regions.

MODIS Terra Chl images from the GESDAAC (Goddard Earth Science Distributed Active Archive Center) derived by the SA code (chl_a_3) and empirical-ratio code (chl_a_2) were composited in 39 km bins for December 2000 and are shown in Fig. 13.8. The subtropical gyre regions appear similar for the two images, but the Chl values are clearly elevated with the SA code for the high-latitude and equatorial upwelling regions where chlorophyll are richer.

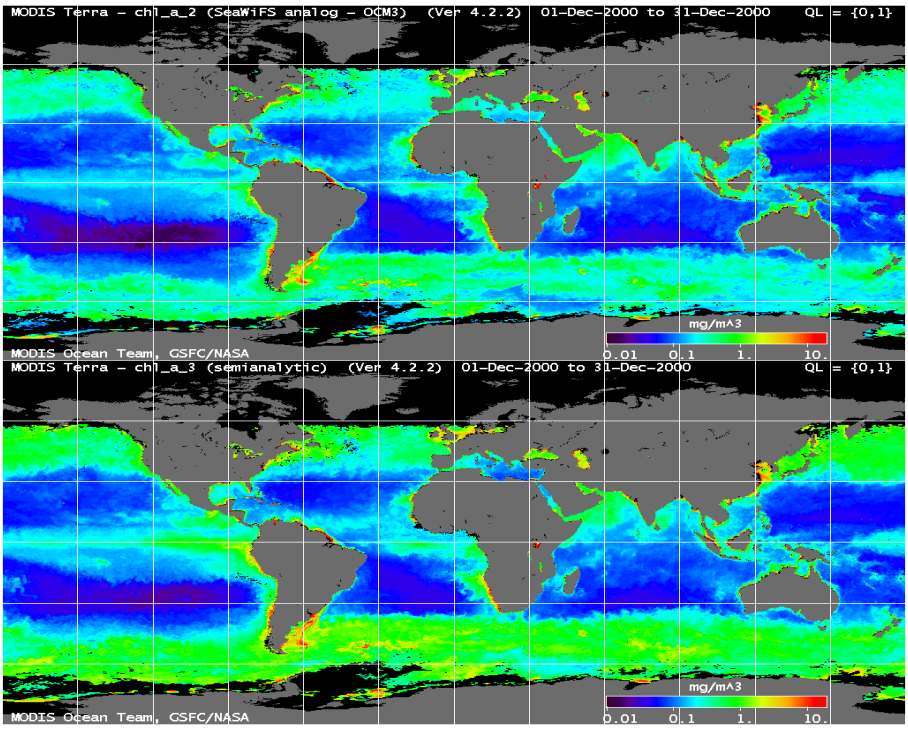


Figure 13.8. Global composited maps (December 2000) of chlorophyll a concentration (mg/m$^3$) retrieved using empirical (top) and semi-analytic (bottom) algorithms from MODIS Terra radiometry (after Carder et al. [2004]).

### 13.6 Monitoring Coastal Ocean Processes using IOPs and Numerical Circulation Models

IOPs provide an improved capability to understand how physical processes influence the bio-optical processes [*Arnone and Parsons*, 2004; *Bissett et al.*, 2001]. For instance, ocean color IOP products from MODIS and SeaWIFS are being integrated with numerical circulation models. The Navy Coastal Ocean Model (NCOM) is forced by large scale ocean models which currently assimilate sea surface height from altimetry and sea surface temperature (SST) from AVHRR. These models are at 32 degree resolution with 41 sigma levels to characterize the mesoscale features (http://www7320.nrlssc.navy.mil/global_ncom/). Overlaying the modeled properties (currents, salinity, surface heights) with optical properties adds continuity to understanding IOP image products. This fusion of physical models and IOP imagery enables improved understanding of the distribution of bio-optical processes that are linked with mesoscale ocean circulation features. Different IOP properties, such as backscattering, CDOM and phytoplankton absorption respond differently to mesoscale processes. Along the U.S. West coast, filaments associated with the California Current System are driven by the physical circulation as shown in Fig. 13.9 [*Penta et al.*, 2005; *Shulman et al.*, 2004]. The corresponding IOP distribution within these filaments is used to define the response of bio-optical processes. For example, the influence of the strong southerly flow off the Channel Islands is characterized by backscattering and total absorption products. Within this filament, the elevated particles are located south of the strong flow (point A) as shown in the $b_b(551)$ image (a result of advection), whereas the strongest currents (point B) located close to land have elevated total absorption as shown in the $a(443)$ image (a result of coastal upwelling). Divergent and convergent mesoscale fronts are revealed by the IOP properties observed in satellite imagery (Fig. 13.9). Similar differences in the distribution of backscattering and absorption have been observed by [*Otero and Siegel*, 1995].

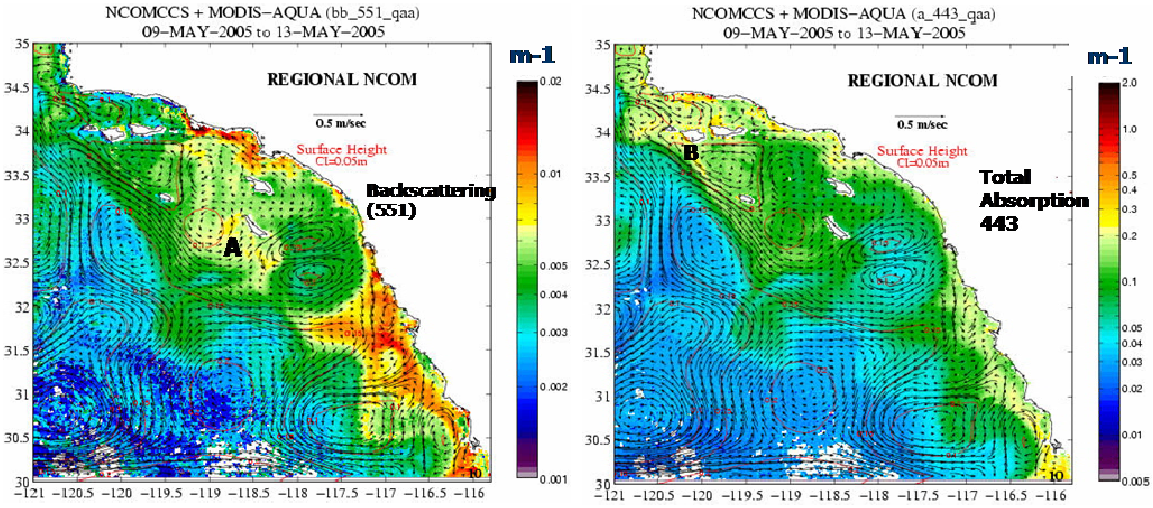


Figure 13.9. The circulation along the California Coast develops coastal filaments shown in surface currents and MODIS Aqua IOP products. Differences in the locations of backscattering at 551 nm (associated with particles) and the total absorption at 443 nm (detritus, CDOM and phytoplankton) indicate varying bio-optical processes within these filaments.

## 13.7 Conclusions

Our understanding of how the optical properties of water constituents are related to ocean processes has advanced significantly in the last decade. Use of IOPs to characterize ocean processes provides improved methods toward monitoring and understanding the role which the ocean has played on global scales. Because IOPs are closely associated with the water leaving radiance measured by satellites and IOP retrievals are robust and stable as shown by previous chapters, IOP products are critical for monitoring and detecting changes in the ocean's climatology and forecasting ocean biogeochemical processes.

## Chapter 14. Summary and Conclusions

ZhongPing Lee, J. Ronald V. Zaneveld, Stephane Maritorena, Hubert Loisel, Roland Doerffer, Paul Lyon, Emmanuel Boss, Kendall L. Carder, Emmanuel Devred, Robert Arnone

Inherent optical properties (IOPs) are the fundamental parameters of hydrological optics. The IOPs, in combination with radiances from the sun and sky, determine water-leaving radiance, which in turn defines water color (an apparent optical property). At the same time, IOPs are also environmental properties. Their variation is directly related to changes in concentration, size distribution and composition of particulate matter and/or dissolved constituents. IOPs derived from remote sensing of ocean color provide innovative opportunities for environmental observation and oceanographic studies on time and space scales not achievable with *in situ* measurements.

To accurately derive various IOPs from water color, as presented in this report, is not an easy and straightforward task. This report presents some frequently encountered methods for IOP retrieval. The algorithms presented here have different levels of complexity; some are explicit about processes, some are inexplicit; some have less empirical inputs, while others have more empiricism built into them. Obviously, there remains room for improvement in the derivation of IOPs. As new information becomes available, it is anticipated that present algorithms could be improved, or exciting new methods would be developed. It is natural that algorithm development is always a continuing and evolving process.

An algorithm works as a mathematical filter in analogy to physical or chemical filters used in the lab or field. In this filtering process, explicitly or inexplicitly, uncertainties are introduced into the desired products. More uncertainties are introduced when fewer parameters are under control. This concept is well illustrated with the IOP inversions, regardless of the method used. Fig. 1.3 in Chapter 1 and the algorithm results of each chapter, clearly show that the overall best properties that can be obtained from ocean color are the spectral absorption and backscattering coefficients of the total water volume. This is because they are the properties directly related to ocean color as observed by a space-borne sensor. When decomposing the total absorption coefficient into the components of phytoplankton pigments and colored matters, less accurate results are anticipated due to overlapping of spectral signals and because the spectral shapes of both components are not constant. Moreover, if the chlorophyll concentration is desired, more uncertainties will be introduced because the chlorophyll-specific absorption coefficient is not constant at a given wavelength, nor is the relationship between backscattering and chlorophyll well defined.

Fundamentally, there are more unknown factors affecting the retrieval of Chl from ocean color than unknown factors affecting the retrieval of absorption and backscattering coefficients. For this reason, we should revisit why Chl should remain the primary product of ocean color remote sensing rather than the IOPs of the bulk water or the optical properties of phytoplankton. The robust and stable results of the total absorption and backscattering coefficients from these various algorithms, which are developed independently and are based on different principles, clearly indicate that these optical properties should be taken as standard products for all ocean color satellite missions. These optical properties, resembling the sea surface temperature, can well serve as climatology data records to study the long-term change of the oceans.

Because inherent optical properties provide important indices for our water environments and open new doors for oceanographic studies, we should spend a good deal of effort on the following subjects to improve IOP products:

a. Increased high-quality *in situ* co-located measurements of remote-sensing reflectance and IOPs.

b. Improved methods to select model parameters such as the spectral shapes of individual IOPs that include $b_b(\lambda)$, $a_{ph}(\lambda)$ and $a_{dg}(\lambda)$. Separation of the global ocean into dynamic biogeochemical provinces may provide vital help in this regard (for more information please visit http://www.ioccg.org/groups/dowell.html for “Global Ecological Provinces”).

c. Better quantification of uncertainties in derived products.

d. Algorithms based on fundamentals of hydrological optics. Simple empirical relationships prevent understanding of the basics and, therefore, limit advancement in ocean color remote sensing.

e. Space based sensors should be equipped with at least a spectral band in the region of 620 – 640 nm. Such a band is important for coastal remote sensing. Current sensors such as SeaWiFS or MODIS lack such a band. The 670 nm or 680 nm bands of SeaWiFS and MODIS are more or less contaminated by chlorophyll-a fluorescence. Fortunately, the MERIS sensor of ESA does have a band around 620 nm.

f. Improved procedure for atmospheric correction. All algorithms tested use remote-sensing reflectance ($R_{rs}$) as inputs for the calculation of IOPs. Quality of $R_{rs}$, which is one of the products derived from atmospheric correction, plays a critical role in the accuracy of retrieved IOPs. Addition of UVa bands would assist the derivation of $R_{rs}$ from satellite measured radiance, especially for coastal waters. Also, such bands may increase the ability to separate phytoplankton absorption from that of dissolved and non-pigmented particulate materials.

g. And, finally, enhance and broaden applications of IOPs for oceanographic studies, which are the ultimate goal of ocean color remote sensing.

It is necessary to point out that in this exercise the water column is assumed homogeneous in water properties. Passive optical remote sensing becomes quite a challenge when the water column is significantly stratified. Further, we did not discuss issues related to optically shallow environments in this report.

In the past decade, there have been significant progresses in remote sensing of IOPs from the observation of ocean color and applications of IOPs in oceanography studies. However, as listed above, there are still many works ahead of us in ocean color remote sensing.

**Reference**


Åas, E., and N.K. Højerslev, Analysis of underwater radiance observations: Apparent optical properties and analytic functions describing the angular radiance distribution, *J. Geophys. Res.*, *104*, 8015-8024, 1999.

Aires, F., C. Prigent, and W.B. Rossow, Neural network uncertainty assessment using Bayesian statistics: A remote sensing application, *Neural Computation*, *16*, 2415-2458, 2004.

Arnone, R.A., and A.R. Parsons, Real-time use of ocean color remote sensing for coastal monitoring, in *Remote Sensing of the Coastal Environments*, edited by R.L. Miller, C.E. DelCastillo, and B.A. McKee, Kluwer academic, Dordrecht, The Netherlands, 2004.

Arnone, R.A., A.M. Wood, and R.W. Gould, The evolution of optical water mass classification, *Oceanography*, *17* (2), 14-15, 2004.

Balch, W.M., H.R. Gordon, B.C. Bowler, D.T. Drapeau, and E.S. Booth, Calcium carbonate measurements in the surface global ocean based on Moderate-Resolution Imaging Spectroradiometer data, *J. Geophys. Res.*, *110* (C07001), doi:10.1029/2004JC002560, 2005.

Barnard, A.H., J.R. Zaneveld, and W.S. Pegau, In situ determination of the remotely sensed reflectance and the absorption coefficient: closure and inversion, *Applied Optics*, *38*, 5108-5117, 1999.

Bates, D.M., and D.G. Watts, *Nonlinear regression analysis and its applications*, 365 pp., Wiley, 1988.

Behrenfeld, M.J., E. Boss, D. Siegel, and D.M. Shea, Carbon-based ocean productivity and phytoplankton physiology from space, *Global biogeochemical cycles*, *19, GB1006*, doi:10.1029/2004GB002299, 2005.

Behrenfeld, M.J., and P.G. Falkowski, A consumer's guide to phytoplankton primary productivity models, *Limnol. Oceanogr.*, *42* (7), 1479-1491, 1997.

Berwald, J., D. Stramski, C.D. Mobley, and D.A. Kiefer, Influences of absorption and scattering on vertical changes in the average cosine of the underwater light field, *Limnol. Oceanogr.*, *40*, 1347-1357, 1995.

Bissett, W.P., R. Arnone, S. DeBra, D.A. Dieterle, D. Dye, G.J. Kirkpatrick, O.M. Schofield, and G.A. Vargo, Predicting the optical properties of the West Florida Shelf: resolving the potential impacts of a terrestrial boundary condition on the distribution of colored dissolved and particulate matter, *Marine Chemistry*, *95* (3-4), 199-233, 2005.

Bissett, W.P., O. Schofied, S. Glenn, J.J. Cullen, W.L. Miller, A.J. Plueddemann, and C.D. Mobley, Resolving the impacts and feedback of ocean optics on upper ocean ecology, *Oceanography*, *14* (3), 30-53, 2001.

Boss, E., and W.S. Pegau, The relationship of light scattering at an angle in the backward direction to the backscattering coefficient, *Applied Optics*, *40*, 5503-5507, 2001.

Bricaud, A., M. Babin, A. Morel, and H. Claustre, Variability in the chlorophyll-specific absorption coefficients of natural phytoplankton: Analysis and parameterization, *J. Geophys. Res.*, *100*, 13321-13332, 1995.

Bricaud, A., H. Claustre, J. Ras, and K. Oubelkheir, Natural variability of phytoplanktonic absorption in oceanic waters: Influence of the size structure of algal populations, *J. Geophys. Res.*, *109* (C11010), doi:10.1029/2004JC002419, 2004.

Bricaud, A., and A. Morel, Light attenuation and scattering by phytoplanktonic cells: a theoretical modeling, *Applied Optics*, *25*, 571-580, 1986.

Bricaud, A., A. Morel, M. Babin, K. Allali, and H. Claustre, Variations of light absorption by suspended particles with chlorophyll a concentration in oceanic (case 1) waters: Analysis and implications for bio-optical models, *J. Geophy. Res.*, *103*, 31033-31044, 1998.

Bricaud, A., A. Morel, and L. Prieur, Absorption by dissolved organic matter of the sea (yellow substance) in the UV and visible domains, *Limnol. Oceanogr.*, *26*, 43-53, 1981.

Bukata, R.P., J.H. Jerome, K.Y. Kondratyev, and D.V. Pozdnyakov, *Optical Properties and Remote Sensing of Inland and Coastal Waters*, CRC Press, Boca Raton, FL, 1995.

Burenkov, V.I., V.I. Verdernikov, S.V. Ershova, O.V. Kopelevitch, and S.V. Sheberstov, Use of satellite ocean color data for assessment of bio-optical characteristics in the Barent Sea, *Okeanologiya*, *41*, 485-492, 2001.

Cannizzaro, J.P., K.L. Carder, F.R. Chen, C.A. Heil, and G.A. Vargo, A novel technique for detection of the toxic dinoflagellate, *Karenia brevis*, in the Gulf of Mexico from remotely sensed ocean color data, *Cont. Shelf Res.*, accepted, 2005.

Carder, K.L., F.R. Chen, J.P. Cannizzaro, J.W. Campbell, and B.G. Mitchell, Performance of the MODIS semi-analytical ocean color algorithm for chlorophyll-a, *Advances in Space Research*, *33* (7), 1152-1159, 2004.

Carder, K.L., F.R. Chen, Z.P. Lee, S.K. Hawes, and D. Kamykowski, Semianalytic Moderate-Resolution Imaging Spectrometer algorithms for chlorophyll-a and absorption with bio-optical domains based on nitrate-depletion temperatures, *J. Geophy. Res*, *104*, 5403-5421, 1999.

Carder, K.L., S.K. Hawes, K.A. Baker, R.C. Smith, R.G. Steward, and B.G. Mitchell, Reflectance model for quantifying chlorophyll a in the presence of productivity degradation products, *J. Geophys. Res*, *96*, 20599-20611, 1991.

Carder, K.L., R.G. Steward, G.R. Harvey, and P.B. Ortner, Marine humic and fulvic acids: their effects on remote sensing of ocean chlorophyll, *Limnol. Oceanogr.*, *34*, 68-81, 1989.

Chandrasekhar, S., *Radiative Transfer*, 393 pp., Dover, New York, 1960.

Ciotti, A.M., M.R. Lewis, and J.J. Cullen, Assessment of the relationships between domininant cell size in natural phytoplankton communities and spectral shape of the absorption coefficient, *Limnol. Oceanogr.*, *47*, 404-417, 2002.

Claustre, H., S.B. Hooker, L.V. Heukelem, J.F. Berthon, R. Barlow, J. Ras, H. Sessions, C. Targa, C.S. Thomas, D.V.d. Linde, and J.C. Marty, An intercomparison of HPLC phytoplankton methods using in situ samples: Application to remote sensing and database activities, *Marine Chemistry*, *85* (1-2), 41-61, 2004.

Claustre, H., and S. Maritorena, The many shades of ocean blue, *Science*, *302*, 1514-1515, 2003.

Cleveland, J.S., Regional models for phytoplankton absorption as a function of chlorophyll a concentration, *J. Geophys. Res.*, *100*, 13,333-13,344, 1995.

Coble, P., C. Hu, R. Gould, G. Chang, and A.M. Wood, Colored dissolved organic matter in the coastal ocean: An optical tool for coastal environmental assessment and management, *Oceanography*, *17*, 50-59, 2004.

Cullen, J.J., A.M. Ciotti, R.F. Davis, and M.R. Lewis, Optical detection and assessment of algal blooms, *Limnol. Oceanogr.* (42), 1223-1239, 1997.

Devred, E., C. Fuentes-Yaco, S. Sathyendranath, C. Caverhill, H. Maass, V. Stuart, T. Platt, and G. White, A semi-analytic, seasonal algorithm to retrieve chlorophyll-a concentration in the northwest atlantic from SeaWiFS data, *Indian J. Mar. Sci.*, 2005a.

Devred, E., S. Sathyendranath, V. Stuart, H. Maass, O. Ulloa, and T. Platt, A two-component model of phytoplankton absorption in the open ocean: theory and applications, *J. Geophys. Res.*, 2005b.

Doerffer, R., K. Heymann, and H. Schiller, Case 2 water algorithm for the medium resolution imaging spectrometer (MERIS) on ENVISAT, ESA report ENVISAT validation workshop, 2002.

Doerffer, R., and H. Schiller, Neural Network for retrieval of concentrations of water constituents with the possibility of detecting exceptional out of scope spectra, in *IEEE 2000 International Geoscience and Remote Sensing Symposium*, pp. 714-717, Honolulu, Hawaii USA, 2000.

Doerffer, R., and H. Schiller, The MERIS case 2 water algorithm, *Int. J. Remote Sensing*, accepted, 2006.

Dupouy, C., H. Loisel, J. Neveux, C. Moulin, S. Brown, J. Blanchot, A. Lebouteiller, and M. Landry, Microbial absorption and backscattering coefficients from in situ and POLDER satellite during an El Nino-Southern Oscillation cold phase in the equatorial Pacific (180$^{o}$), *J. Geophys. Res.*, *108* (C12), 8138, 2003.

Fischer, J., and F. Fell, Simulation of MERIS measurements above selected ocean waters, *Int. J. Remote Sensing*, *20* (9), 1787-1807, 1999.

Garver, S.A., and D. Siegel, Inherent optical property inversion of ocean color spectra and its biogeochemical interpretation 1. Time series from the Sargasso Sea, *J. Geophy. Res*, *102*, 18607-18625, 1997.

Gohin, F., J.N. Druon, and L. Lampert, A five channel chlorophyll concentration algorithm applied to SeaWiFS data processed by SeaDAS in coastal waters, *Int. J. Remote Sensing*, *23*, 1639-1661, 2002.

Gordon, H.R., Can the Lambert-Beer law be applied to the diffuse attenuation coefficient of ocean water?, *Limnol. Oceanogr.*, *34*, 1389-1409, 1989.

Gordon, H.R., Inverse Methods in hydrologic optics, *Oceanologia*, *44* (1), 9-58, 2002.

Gordon, H.R., O.B. Brown, R.H. Evans, J.W. Brown, R.C. Smith, K.S. Baker, and D.K. Clark, A semianalytic radiance model of ocean color, *J. Geophy. Res.*, *93*, 10,909-10,924, 1988.

Gordon, H.R., O.B. Brown, and M.M. Jacobs, Computed relationship between the inherent and apparent optical properties of a flat homogeneous ocean, *Applied Optics*, *14*, 417-427, 1975.

Gordon, H.R., and D.K. Clark, Remote sensing optical properties of a stratified ocean: an improved interpretation, *Applied Optics*, *19*, 3428-3430, 1980.

Gordon, H.R., and A. Morel, *Remote assessment of ocean color for interpretation of satellite visible imagery: A review*, 44 pp., Springer-Verlag, New York, 1983.

Gould, R.W., and R. Arnone, Remote sensing estimates of inherent optical properties in a coastal environment, *Remote Sens. Environ.*, *61*, 290-301, 1997.

Gould, R.W., and R.A. Arnone, Optical Water Mass Classification for Ocean Color Imagery, in *Second International Conference, Current Problems in Optics Of Natural Waters*, St. Petersburg, Russia, 2003.

Gregg, W.W., and K.L. Carder, A simple spectral solar irradiance model for cloudless maritime atmospheres, *Limnol. Oceanogr.*, *35*, 1657-1675, 1990.

Haltrin, V.I., Chlorophyll-based model of seawater optical properties, *Applied Optics*, *38* (33), 6826-6832, 1999.

Hoepffner, N., and S. Sathyendranath, Effect of pigment composition on absorption properties of phytoplankton, *Mar. Ecol. Prog. Ser.*, *73*, 11-23, 1991.

Hoepffner, N., and S. Sathyendranath, Bio-optical characteristics of coastal waters: Absorption spectra of phytoplankton and pigment distribution in the western North Atlantic, *Limnol. Oceanogr.*, *37*, 1660-1679, 1992.

Hoge, F.E., and P.E. Lyon, Satellite retrieval of inherent optical properties by linear matrix inversion of oceanic radiance models: an analysis of model and radiance measurement errors, *J. Geophy. Res.*, *101*, 16631-16648, 1996.

Hoge, F.E., and P.E. Lyon, Spectral parameters of inherent optical property models: Methods for satellite retrieval by matrix inversion of an oceanic radiance model, *Applied Optics*, *38*, 1657-1662, 1999.

Hoge, F.E., C.W. Wright, P.E. Lyon, R.N. Swift, and J.K. Yungel, Inherent optical properties imagery of the western North Atlantic Ocean: Horizontal spatial variability of the upper mixed layer, *J. Geophys. Res.*, *106*, 31,129-31,140, 2001.

Hooker, S.B., W.E. Esaias, G.C. Feldman, W.W. Gregg, and C.R. McClain, An overview of SeaWiFS and Ocean Color, in *NASA Goddard Space Flight Center*, edited by S.B. Hooker, and E.R. Firestone, pp. 24, Greenbelt, MD, 1992.

Hooker, S.B., and S. Maritorena, An evaluation of oceanographic radiometers and deployment methodologies, *J. Atmos. Ocean. Tech.*, *17* (6), 811-830, 2000.

Hooker, S.B., C.R. McClain, J.K. Firestone, T.L. Westphal, E.-N. Yeh, and Y. Ge, The SeaWiFS Bio-Optical Archive and Storage System (SeaBASS), Part 1, in *NASA Tech. Memo. 104566*, edited by S.B. Hooker, and E.R. Firestone, pp. 1-40, NASA Goddard Space Flight Center, Greenbelt, Maryland, 1994.

Hooker, S.B., G. Zibordi, J.-F. Berthon, D. D'Alimonte, S. Maritorena, S. McLean, and J. Sildam, Results of the second SeaWiFS data analysis round robin, in *NASA Tech. Memo. 2001--206892*, edited by S.B. Hooker, and E.R. Firestone, pp. 71, NASA Goddard Space Flight Center, Greenbelt, Maryland, 2001.

Hu, C., Z. Chen, T.D. Clayton, P. Swarzenski, J.C. Brock, and F.E. Müller-Karger, Assessment of estuarine water-quality indicators using MODIS medium-resolution bands: Initial results from Tampa Bay, Florida, *Remote Sens. Environ.*, *93*, 423-441, 2004.

Hu, C., Z. Lee, F.E. Muller-Karger, K.L. Carder, and J.J. Walsh, Ocean color reveals phase shift between marine plants and yellow substance, *IEEE Geoscience and Remote Sensing Letters*, *accepted*, 2005.

Hu, C., F.E. Muller-Karger, D.C. Biggs, K.L. Carder, B. Nababan, D. Nadeau, and J. Vanderbloemen, Comparison of ship and satellite bio-optical measurements on the continental margin of the NE Gulf of Mexico, *Int. J. Remote Sensing*, *24*, 2597-2612, 2003.

Kamykowski, D., A preliminary biophysical model of the relationship between temperature and plant nutrients in the upper ocean, *Deep-Sea Res.*, *34* (7), 1067-1079, 1987.

Kamykowski, D., and S. Zentara, Predicting plant nutrient concentrations from temperature and sigma-t in the upper kilometer of the world ocean, *Deep-Sea Res.*, *33*, 89-105, 1986.

Kirk, J.T.O., Dependence of relationship between inherent and apparent optical properties of water on solar altitude, *Limnol. Oceanogr.*, *29*, 350-356, 1984.

Kirk, J.T.O., *Light & Photosynthesis in Aquatic Ecosystems*, University Press, Cambridge, 1994.

Kopelevich, O.V., and V.I. Burenkov, Relation between the spectral values of the light absorption coefficients of sea water, phytoplanktonic pigments, and the yellow substance, *Oceanology*, *17*, 278-282, 1977.

Krasnopolsky, V., and H. Schiller, Some Neural Network applications in environmental sciences part I: forward and inverse problems in geophysical remote measurements, *Neural Networks*, *16*, 321-334, 2003.

Laws, E.A., *Mathematical methods for oceanographers: an introduction*, John Wiley and Sons, Inc., New York, NY, 1997.

Lee, Z., K. Du, R. Arnone, S.C. Liew, and B. Penta, Penetration of solar radiation in the upper ocean - A numerical model for oceanic and coastal waters, *J. Geophy. Res.*, in press, 2005a.

Lee, Z.P., K.L. Carder, and R. Arnone, Deriving inherent optical properties from water color: A multi-band quasi-analytical algorithm for optically deep waters, *Applied Optics*, *41*, 5755-5772, 2002.

Lee, Z.P., K.L. Carder, and K.P. Du, Effects of molecular and particle scatterings on model parameters for remote-sensing reflectance, *Applied Optics*, *43*, 4957-4964, 2004.

Lee, Z.P., K.L. Carder, C.D. Mobley, R.G. Steward, and J.S. Patch, Hyperspectral remote sensing for shallow waters. 1. A semianalytical model, *Applied Optics*, *37*, 6329-6338, 1998a.

Lee, Z.P., K.L. Carder, C.D. Mobley, R.G. Steward, and J.S. Patch, Hyperspectral remote sensing for shallow waters: 2. Deriving bottom depths and water properties by optimization, *Applied Optics*, *38*, 3831-3843, 1999.

Lee, Z.P., K.L. Carder, T.G. Peacock, C.O. Davis, and J.L. Mueller, Method to derive ocean absorption coefficients from remote-sensing reflectance, *Applied Optics*, *35*, 453-462, 1996a.

Lee, Z.P., K.L. Carder, R.G. Steward, T.G. Peacock, C.O. Davis, and J.S. Patch, An empirical algorithm for light absorption by ocean water based on color, *J. Geophy. Res*, *103*, 27967-27978, 1998b.

Lee, Z.P., K.L. Carder, R.G. Steward, and M.J. Perry, Estimating primary production at depth from remote sensing, *Applied Optics*, *35*, 463-474, 1996b.

Lee, Z.P., M. Darecki, K.L. Carder, C. Davis, D. Stramski, and W.J. Rhea, Diffuse attenuation coefficient of downwelling irradiance: An evaluation of remote sensing methods, *J. Geophys. Res.*, *110* (C02017), doi:10.1029/2004JC002573, 2005b.

Loisel, H., E. Bosc, D. Stramski, K. Oubelker, and P.Y. Deschamps, Seasonal variability of the backscattering coefficients in the Mediterranean Sea based on Satellite SeaWIFS imagery, *Geophys. Res. Lett.*, *28*, 4203-4206, 2001a.

Loisel, H., and A. Morel, Light scattering and chlorophyll concentration in Case 1 waters: A reexamination, *Limnol. Oceanogr.*, *43*, 847-858, 1998.

Loisel, H., and A. Morel, Non-isotropy of the upward radiance field in typical coastal (Case 2) waters, *Int. J. Remote Sensing*, *22* (2), 275-295, 2001.

Loisel, H., J.M. Nicolas, P.Y. Deschamps, and R. Frouin, Seasonal and inter-annual variability of the particulate matter in the global ocean, *Geophys. Res. Lett.*, *29* (24), 2196, doi:10.1029/2002GL015948, 2002.

Loisel, H., and D. Stramski, Estimation of the inherent optical properties of natural waters from the irradiance attenuation coefficient and reflectance in the presence of Raman scattering, *Applied Optics*, *39*, 3001-3011, 2000.

Loisel, H., D. Stramski, B.G. Mitchell, F. Fell, V. Fournier-Sicre, B. Lemasle, and M. Babin, Comparison of the ocean inherent optical properties obtained from measurements and inverse modeling, *Applied Optics*, *40*, 2384-2397, 2001b.

Lutz, V.A., S. Sathyendranath, and E.J.H. Head, Absorption coefficient of phytoplankton: Regional variations in the North Atlantic, *Mar. Ecol. Prog. Ser.*, *135* (1-3), 197-213, 1996.

Lyon, P.E., F.E. Hoge, C.W. Wright, R.N. Swift, and J.K. Yungel, Chlorophyll biomass in the global oceans: Satellite retrieval using inherent optical properties, *Applied Optics*, *43*, 5886-5892, 2004.

Maritorena, S., and D.A. Siegel, Consistent merging of satellite ocean color data sets using a bio-optical model, *Remote Sens. Environ.*, *94*, 429-440, 2005.

Maritorena, S., D.A. Siegel, and A.R. Peterson, Optimization of a semianalytical ocean color model for global-scale applications, *Applied Optics*, *41*, 2705-2714, 2002.

McClain, C.R., R.A. Barnes, J. R.E. Eplee, B.A. Franz, N.C. Hsu, F.S. Patt, C.M. Pietras, W.D. Robinson, B.D. Schieber, G.M. Schmidt, M. Wang, S.W. Bailey, and P.J. Werdell, SeaWiFS Postlaunch Calibration and Validation Analyses, Part 2. , Vol. 10, , Eds., , 57 pp., in *NASA Tech. Memo. 2000-206892*, edited by S.B. Hooker, and E.R. Firestone, NASA Goddard Space Flight Center, Greenbelt, Maryland, 2000.

Melin, F., Z. G., and J.F. Berthon, Comparison of *in situ* and SeaWiFS derived atmospheric and marine products for the Adriatic Sea, in *Ocean Optics*, edited by S. Ackleson, Santa Fe, New Mexico, US, 2002.

Mitchell, G., A. Bricaud, K.L. Carder, J. Cleveland, G. Ferrari, R. Gould, M. Kahru, M. Kishino, H. Maske, T. Moisan, L. Moore, N. Nelson, D. Phinney, R. Reynolds, H. Sosik, D. Stramski, S. Tassan, C. Trees, A. Weidemann, J. Weiland, and A. Vodacek., Determination of spectral absorption coefficients of particles, dissolved material, and phytoplankton for discrete water samples, in *Ocean optics protocols for satellite ocean color sensor validation, revision 2. NASA/TM 2000-209966*, edited by G.S. Fargion, and J.L. Mueller, pp. 125-153, NASA,, Goddard Space Flight Center, Greenbelt, Maryland, 2000.

Mobley, C.D., *Light and Water: radiative transfer in natural waters*, Academic Press, New York, 1994.

Mobley, C.D., Hydrolight 3.0 Users' Guide, SRI International, Menlo Park, Calif., 1995.

Mobley, C.D., B. Gentili, H.R. Gordon, Z. Jin, G.W. Kattawar, A. Morel, P. Reinersman, K. Stamnes, and R.H. Stavn, Comparison of numerical models for computing underwater light fields, *Applied Optics*, *32*, 7484-7504, 1993.

Morel, A., Optical properties of pure water and pure sea water, in *Optical Aspects of Oceanography*, edited by N.G. Jerlov, and Nielsen, E. S., pp. 1-24, Academic, New York, 1974.

Morel, A., Available, usable, and stored radiant energy in relation to marine photosynthesis, *Deep-Sea Res*, *25*, 673-688, 1978.

Morel, A., Optical modeling of the upper ocean in relation to its biogenous matter content (Case I waters), *J. Geophy. Res*, *93*, 10749-10768, 1988.

Morel, A., and D. Antoine, Heating rate within the upper ocean in relation to its bio-optical state, *J. of Physical Oceanography*, *24*, 1652-1665, 1994.

Morel, A., and B. Gentili, Diffuse reflectance of oceanic waters (2): Bi-directional aspects, *Applied Optics*, *32*, 6864-6879, 1993.

Morel, A., and B. Gentili, Diffuse reflectance of oceanic waters, III, Implications of bi-directionality for the remote sensing problem, *Applied Optics*, *35*, 4850-4862, 1996.

Morel, A., and S. Maritorena, Bio-optical properties of oceanic waters: A reappraisal, *J. Geophy. Res*, *106*, 7163-7180, 2001.

Morel, A., and L. Prieur, Analysis of variations in ocean color, *Limnol. Oceanogr.*, *22*, 709-722, 1977.
Mueller, J.L., SeaWiFS algorithm for the diffuse attenuation coefficient, K(490), using water-leaving radiances at 490 and 555 nm, in *SeaWiFS Postlaunch Calibration and Validation Analyses, Part 3*, edited by S.B. Hooker, pp. 24-27, 2000.
Mueller, J.L., and R.W. Austin, Ocean optics protocols for SeaWiFS validation, in *NASA Technical Memorandum 104566*, edited by S.B.H.a.E.R. Firestone, NASA Goddard Space Flight Center, Greenbelt, MD, 1992.
Mueller, J.L., and R.W. Austin, Ocean Optics Protocols for SeaWiFS Validation, Revision 1, in *NASA Tech. Memo. 104566*, edited by S.B. Hooker, E.R. Firestone, and J.G. Acker, pp. 67, NASA, Goddard Space Flight Center, Greenbelt, Maryland, 1995.
Mueller, J.L., C. Davis, R. Arnone, R. Frouin, K.L. Carder, Z.P. Lee, R.G. Steward, S. Hooker, C.D. Mobley, and S. McLean, Above-water radiance and remote sensing reflectance measurement and analysis protocols, in *Ocean Optics Protocols for Satellite Ocean Color Sensor Validation, Revision 3, NASA/TM-2002-210004*, edited by J.L. Mueller, and G.S. Fargion, pp. 171-182, 2002.
Nelson, N.B., and D.A. Siegel, Chromophoric DOM in the open ocean, in *Biogeochemistry of Marine Dissolved Organic Matter*, edited by D.A. Hansell, and C.A. Carlson, Academic Press, 2002.
Nelson, N.B., D.A. Siegel, and A.F. Michaels, Seasonal dynamics of colored dissolved material in the Sargasso Sea, *Deep-Sea Res.*, *45* (6), 931-957, 1998.
Ohlmann, J.C., and D. Siegel, Ocean Radiant Heating. Part II: Parameterizing solar radiation transmission through the upper ocean, *J. of Physical Oceanography*, *30*, 1849-1865, 2000.
O'Reilly, J., S. Maritorena, B.G. Mitchell, D. Siegel, K.L. Carder, S. Garver, M. Kahru, and C. McClain, Ocean color chlorophyll algorithms for SeaWiFS, *J. Geophy. Res*, *103*, 24937-24953, 1998.
Otero, M.P., and D.A. Siegel, Spatial and temporal characteristics of sediment plumes and phytoplankton blooms in the Santa Barbara Channel, *Deep-Sea Res.*, *100*, 13279-13294, 1995.
Pegau, W.S., D. Gray, and J.R.V. Zaneveld, Absorption and attenuation of visible and near-infrared light in water: dependence on temperature and salinity, *Applied Optics*, *36* (24), 6035-6046, 1997.
Penta, B., J. Kindle, I. Shulman, S. deRada, S. Anderson, Z.P. Lee, F. Chai, and R. Arnone, Remote sensing in conjunction with the Navy Coastal Ocean Model (NCOM): examples from the California current system, in *Eighth International Conference on Remote Sensing for Marine and Coastal Environments*, Halifax, Nova Scotia, 2005.
Platt, T., and S. Sathyendranath, Oceanic primary production: estimation by remote sensing at local and regional scales, *Science*, *241*, 1613-1620, 1988.
Pope, R., and E. Fry, Absorption spectrum (380 - 700 nm) of pure waters: II. Integrating cavity measurements, *Applied Optics*, *36*, 8710-8723, 1997.
Preisendorfer, R.W., *Hydrologic optics vol. 1: introduction*, National Technical Information Service. Also available on CD, Office of Naval Research, Springfield, 1976.
Press, W.H., *Numerical Recipes in FORTRAN: The Art of Scientific Computing, 2nd ed.*, 992 pp., Cambridge University Press, 1992.
Press, W.H., S.A. Teukolsky, W.T. Vetterling, and B.P. Flannerty, *Numerical Recipes in C: The Art of Scientific Computing, 2nd Edition*, Cambridge University Press, New York, 1992.
Prieur, L., and S. Sathyendranath, An optical classification of coastal and oceanic waters based on the specific spectral absorption curves of phytoplankton pigments, dissolved organic matter, and other particulate materials, *Limnol. Oceanogr.*, *26*, 671-689, 1981.
Reynolds, R.A., D. Stramski, and B.G. Mitchell, A chlorophyll-dependent semianalytical reflectance model derived from field measurements of absorption and backscattering coefficients within the Southern Ocean, *J. Geophy. Res.*, *106*, 7125-7138, 2001.
Roesler, C.S., and E. Boss, Spectral beam attenuation coefficient retrieved from ocean color inversion, *Geophys. Res. Lett.*, *30* (9), 1468, 2003.
Roesler, C.S., and M.J. Perry, In situ phytoplankton absorption, fluorescence emission, and particulate backscattering spectra determined from reflectance, *J. Geophy. Res*, *100*, 13279-13294, 1995.

Roesler, C.S., M.J. Perry, and K.L. Carder, Modeling in situ phytoplankton absorption from total absorption spectra in productive inland marine waters, *Limnol. Oceanogr.*, *34*, 1510-1523, 1989.
Sathyendranath, S., G. Cota, V. Stuart, M. Maass, and T. Platt, Remote sensing of phytoplankton pigments: a comparison of empirical and theoretical approaches, *Int. J. Remote Sensing*, *22*, 249-273, 2001.
Sathyendranath, S., and T. Platt, The spectral irradiance field at the surface and in the interior of the ocean: a model for applications in oceanography and remote sensing, *J. Geophy. Res*, *93*, 9270-9280, 1988.
Sathyendranath, S., and T. Platt, Remote sensing of ocean chlorophyll: consequence of nonuniform pigment profile, *Applied Optics*, *28*, 490-495, 1989.
Sathyendranath, S., and T. Platt, Analytic model of ocean color, *Applied Optics*, *36*, 2620-2629, 1997.
Sathyendranath, S., and T. Platt, Ocean-color model incorporating transspectral processes, *Applied Optics*, *37*, 2216-2227, 1998.
Sathyendranath, S., T. Platt, B. Irwin, E. Horne, G. Borstad, V. Stuart, L. Payzant, H. Maass, P. Kepkay, W.K.W. Li, J. Spry, and J. Gower, A multispectral remote sensing study of coastal waters off Vancouver Island, *Int. J. Remote Sensing*, *24*, 893-919, 2004.
Schiller, H., and R. Doerffer, Improved determination of coastal water constituent concentrations from MERIS data, *IEEE Transactions on Geoscience and Remote Sensing*, *43*, 1585-1591, 2005.
SeaWiFS, Ocean color algorithm evaluation, http://seawifs.gsfc.nasa.gov/SEAWIFS/RECAL/Repro3/OC4_reprocess.html, 2000.
Shifrin, K., *Physical optics of ocean water*, 285 pp., American Institute of Physics, New York, 1988.
Shulman, I., J.C. Kindle, S. deRada, S.C. Anderson, B. Penta, and P.J. Martin, Development of a hierarchy of nested models to study the California current system, in *Estuarine and Coastal Modeling, Proceedings of the Eighth International Conference*, edited by M.L. Spaulding, pp. 74-88, Monterey, CA, 2004.
Siegel, D.A., S. Maritorena, N.B. Nelson, D.A. Hansell, and M. Lorenzi-Kayser, Global distribution and dynamics of colored dissolved and detrital organic materials, *J. Geophys. Res.*, *107* (C12), 3228, doi:10.1029/2001JC000965, 2002.
Siegel, D.A., M.C. O'Brien, J.C. Sorensen, D.A. Konnoff, E.A. Brody, J.L. Mueller, C.O. Davis, W.J. Rhea, and S.B. Hooker, Results of the SeaWiFS Data Analysis Round-Robin (DARR-94), in *NASA Tech. Memo. 104566*, edited by S.B. Hooker, and E.R. Firestone, pp. 58, NASA Goddard Space Flight Center, Greenbelt, Maryland, 1995.
Smith, R.C., and K.S. Baker, Optical properties of the clearest natural waters, *Applied Optics*, *20*, 177-184, 1981.
Smith, R.C., B.B. Prezelin, R.R. Bidigare, and K.S. Baker, Bio-optical modeling of photosynthetic production in coastal waters, *Limnol. Oceanogr.*, *34*, 1524-1544, 1989.
Smyth, T.J., S.B. Groom, D.G. Cummings, and C.A. Llewellyn, Comparison of SeaWiFS bio-optical chlorophyll-a algorithms within the OMEXII programme, *Int. J. Remote Sensing*, *23*, 2321-2326, 2002.
Sokal, R.R., and F.J. Rohlf, *Biometry*, 859 pp., Freeman, New York, 1981.
Stramski, D., A. Bricaud, and A. Morel, Modeling the inherent optical properties of the ocean based on the detailed composition of the planktonic community, *Applied Optics*, *40*, 2929-2945, 2001.
Stramski, D., R.A. Reynolds, M. Kahru, and B.G. Mitchell, Estimation of particulate organic carbon in the ocean from satellite remote sensing, *Science*, *285*, 239-242, 1999.
Stuart, V., S. Sathyendranath, T. Platt, H. Maass, and B. Irwin, Pigments and species composition of natural phytoplankton populations: effect on the absorption spectra, *J. Plankton Res.*, *20*, 187-217, 1998.
Thomas, G.E., and K. Stamnes, *Radiative Transfer in the Atmosphere and Ocean*, Cambridge University Press, 1999.
Twardowski, M.J., M.R. Lewis, A. Barnard, and J.R.V. Zaneveld, In-Water Instrumentation and Platforms for Ocean Color remote Sensing Applications, in *Remote sensing of Coastal Aquatic*

*Environments*, edited by R.L. Miller, C.E.D. Castillo, and B.A. McKee, pp. 347, Springer, Dordrecht, 2005.
Ulloa, O., S. Sathyendranath, and T. Platt, Effect of the particle-size distribution on the backscattering ratio in seawater, *Applied Optics*, *30*, 7070-7077, 1994.
van de Hulst, H.C., *Light Scattering By Small Particles*, Dover, 1981.
Van Heukelem, L., C.S. Thomas, and P.M. Glibert, Sources of variability in chlorophyll analysis by fluorometry and high performance liquid chromatography in a SIMBIOS inter-calibration exercise, in *NASA Tech. Memo. 2002-02338-0*, edited by G.S. Fargion, and C.R. McClain, pp. 58, NASA Goddard Space Flight Center, Greenbelt, Maryland, 2002.
Wang, P., E. Boss, and C. Roesler, Uncertainties of Inherent Optical Properties obtained from Semi-Analytical Inversions of Ocean Color, *Applied Optics*, *44* (19), 4074-4085, 2005.
Westberry, T.K., D.A. Siegel, and A. Subramaniam, An improved bio-optical model for the remote sensing of Trichodesmium spp. blooms, *J. Geophys. Res.*, in press, 2005.
Yoder, J.A., J.K. Moore, and R.N. Swift, Putting together the big picture: Remote-sensing observations of ocean color, *Oceanography*, *14* (4), 33-40, 2001.
Zaneveld, J.R.V., New developments of the theory of radiative transfer in the ocean., in *Optical Aspects of Oceanography*, edited by N.G. Jerlov, pp. 121-134, Academic Press, London, 1973.
Zaneveld, J.R.V., Remote sensed reflectance and its dependence on vertical structure: a theoretical derivation, *Applied Optics*, *21*, 4146-4150, 1982.
Zaneveld, J.R.V., An asymptotic closure theory for irradiance in the sea and its inversion to obtain the inherent optical properties, *Limnol. Oceanogr.*, *34*, 1442-1452, 1989.
Zaneveld, J.R.V., A theoretical derivation of the dependence of the remotely sensed reflectance of the ocean on the inherent optical properties, *J. Geophys. Res.*, *100*, 13135-13142, 1995.
Zaneveld, J.R.V., A.H. Barnard, and E. Boss, Theoretical derivation of the depth average of remotely sensed optical parameters, *Optics Express*, *13*, 9052-9061, 2005a.
Zaneveld, J.R.V., J.C. Kitchen, and J.L. Mueller, Vertical structure of productivity and its vertical integration as derived from remotely sensed observations, *Limnol. Oceanogr.*, *38*, 1384-1393, 1993.
Zaneveld, J.R.V., M.J. Twardowski, A. Barnard, and M.R. Lewis, Introduction to radiative transfer, in *Remote sensing of Coastal Aquatic Environments*, edited by R.L. Miller, C.E.D. Castillo, and B.A. McKee, pp. 347, Springer, Dordrecht, 2005b.

**Acronyms and Abbreviations**

| | |
|---|---|
| AOP | Apparent Optical Property |
| AUV | Autonomous Underwater Vehicle |
| CDM | Colored Detrital and Dissolved Material |
| CDOM | Colored Dissolved Organic Matter |
| CZCS | Coastal Zone Color Scanner |
| DOC | Dissolved Organic Carbon |
| ERT | Equation of Radiative Transfer |
| GSM | Garver Siegel Maritorena |
| IOP | Inherent Optical Property |
| LMI | Linear Matrix Inversion |
| MERIS | Medium Resolution Imaging Spectrometer |
| MOBY | Marine Optical Buoy |
| MODIS | Moderate Resolution Imaging Spectroradiometer |
| NCOM | Navy Coastal Ocean Model |
| NDT | Nitrate Depletion Temperature |
| NN | Neural Network |
| NPOESS | National Polar-orbiting Operational Environmental Satellite System |
| NWLR | Normalized Water Leaving Radiance |
| POC | Particulate Organic Carbon |
| QAA | Quasi Analytical Algorithm |
| RMSE | Root Mean Square Error |
| SeaBASS | SeaWiFS Bio-Optical Archive and Storage System |
| SeaWiFS | Sea-viewing Wide Field-of-view Sensor |
| VIIRS | Visible Infrared Imager Radiometer Suite |
| VSF | Volume Scattering Function |